

Development of control systems for movement mechanisms of electric drives based on neural networks

YURII N. KUTOVOI¹, IHOR V. OBRUCH¹, TATIANA YU. KUNCHENKO¹

Abstract. The paper presents the results of the development and investigations of intelligent control systems for electric drives of DC and AC movement mechanisms. It is shown that the use of methods of genetic algorithms for training and structural optimization of neural systems makes it possible to synthesize the control law excluding the self-oscillating process arising from the nonlinearity of the "friction pair" type load. The developed systems have a single easily realizable feedback on the speed of the motor which does not create difficulties in physical realization.

Key words. Neural network control system, genetic algorithm, DC motor of sequential excitation, induction motor, electric drive, transient.

1. Introduction

Traditional control methods based on the classical theory of automatic control for linear systems have now reached sufficient perfection. Using, for example, methods of modal control or systems of subordinate regulation, it is possible to synthesize control systems that ensure the high quality of both static and dynamic parameters for adjusting the coordinates of the electric drive (ED). In the analytic synthesis of the parameters of such systems, matrix, root, topological methods which have been significantly developed lately are widely used [1–3].

However, such a control requires an introduction of external feedbacks across all the main coordinates. This not only complicates the system, but also complicates its implementation when it is necessary to have information about hard-to-measure coordinates such as the elastic moment in a certain kinematic connection. Another disadvantage of such systems may be the impossibility of realizing the synthesized parameters due to limitations on certain coordinates in real ED.

¹National Technical University "Kharkiv Polytechnic Institute" Kyrpychova str. 2, 61002 Kharkiv, Ukraine

One of the most effective tools for creating modern intelligent control systems are artificial neural networks [4] which model the basic mechanisms of information processing in the brain. To construct regulators and identification models based on artificial neural networks, new methods of selecting their structure and parameters are needed. A promising approach to solving this problem is the use of methods of evolutionary modeling, namely genetic algorithms [5], for training and structural optimization of neural networks.

In this paper, a technique for synthesizing a control system for the ED mechanisms of movement based on the theory of neural networks is presented.

2. Problem definition

Until now, DC motors of sequential excitation are widely used in electric transport (electric locomotives, trams, electric cars) and other mechanisms of displacement along with induction motors. These mechanisms have a nonlinear load of the "friction pair" type. The presence of such a load, as shown in [6], under certain combinations of the system parameters, leads to self-oscillating processes, which is inadmissible.

Hence, the problem arises of synthesizing a neural network control system for ED with a DC motor of sequential excitation and induction motors that have a nonlinear load of the "friction pair" type.

3. The technique proposed

Provision of a given quality of regulation, elimination of oscillatory and self-oscillating processes is achieved by introducing a nonlinear regulator into the system, which must have information on easily measured one or several coordinates. These regulators can be classified as neuroregulators—technical devices built on the basis of artificial neural networks.

The functional diagram of the neurocontroller is shown in Fig. 1, the main cell of the neurocontroller is a neuron that simulates the principle of the action of a bio-logical neuron (see Fig. 2).

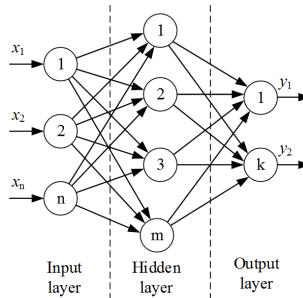


Fig. 1. Diagram of a three-layer artificial neural network

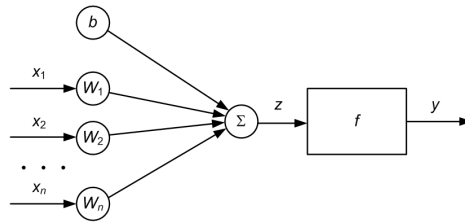


Fig. 2. Model of the j th neuron

The operation of the neurocontroller can be explained as follows. The inputs of the neurocontroller (neurons of the input layer) receive the reference signals and feedback signals. Each of these neurons is associated with the neurons of the hidden layer. The signal of the input neuron x_i comes to the hidden layer neuron multiplied by a certain value $W_{i,j}$, which is the weighting coefficient of the neurons of the hidden layer, that is, the amplified or weakened one. In addition, each of the neurons of the hidden layer receives its additional signal b_j , which is the shift signal and, thus, the input signal of the j th neuron of the hidden layer is equal to the sum of all the incoming signals, that is,

$$y_i = \sum_{j=1}^n W_{i,j}x_i + b_j. \tag{1}$$

For the received signals, a non-linear transformation is performed using the so-called activation function f (see Fig. 3).

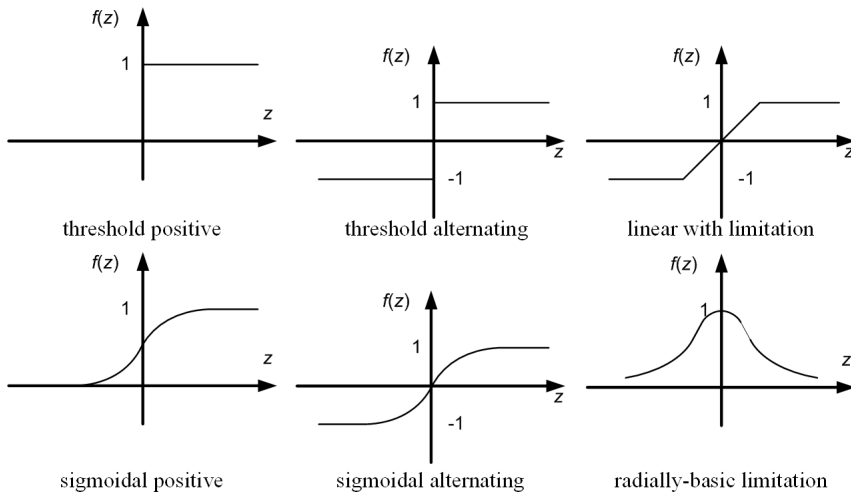


Fig. 3. Types of activation functions of hidden layer neurons

The output signal of the neuron of the hidden layer turns out to be equal to $y_j = z_j$. Then the output signals of the hidden layer neurons multiplied by the weight coefficients $W_{2i,j}$ (the weight coefficients of the output layer neurons) enter the output layer of the neural network and their sum is the output signal of the

neurocontroller. The most frequently used activation functions are shown in Fig. 3, while, as a rule, as activation function of the output layer neurons linear functions with a limitation are used.

The above described procedure for converting the input signals of the neurocontroller provides ample opportunities for forming the required character and value of the output signal by appropriately selecting the values of the weight coefficients $W_{1i,j}$, W_{2j} , the shift value b_j and the type of the activation function. Networks of this type are called perceptrons and are denoted as NN A–B–C, where A, B, C are the number of neurons of the input, hidden and output layers, respectively (for example, the network NN 3-10-1 contains 3 input neurons, 10 neurons of the hidden layer, 1 neuron in the output layer).

The problem of synthesis of a neural network is to determine the weight coefficients and signals of the neuron shift of the hidden and output layers that would provide the required control. To solve this problem, the backpropagation errors algorithm [7], which is essentially a gradient descent method is used, which, by virtue of this, has a known drawback—the localization of the minimization domain. Meanwhile, the space of synthesized parameters has such a large dimension due to a significant number of determinants $W_{i,j}$, W_j , b_j that the expediency of global optimization is obvious.

For global optimization of the parameters of the neurocontroller, it is required to use the genetic algorithm method [5]. Considering the neural network (neurocontroller) as a single set of parameters, the genetic algorithm is able to perform its optimal tuning with the dimensionality of the search space sufficient to solve most practical problems. At the same time, the spectrum of the applications under consideration far exceeds the capabilities of the algorithm of backpropagation errors. The combination of these two computational techniques, artificial neural networks and genetic algorithms is considered today as a potential source of future progress in the field of evolutionary modeling. In addition to its inherent globality, the genetic algorithm, as a training procedure, has the advantage over the algorithm of backpropagation errors that it is able to train the neurocontroller immediately on the output characteristics of the object, rather than the output signals of the neural network.

Just as genetic information about a biological individual is contained in the genes of chromosomes, information about the parameters of a neural network, that is, a neurocontroller, is contained in the form of chains of symbols, called, like in biology and genetics, chromosomes. These parameters are coded using a two- or four-letter alphabet. For simplicity of the presentation, let us consider two-letter (binary) coding of neural network parameters which is used in modeling the evolution of populations (a certain set of chromosomes) of the so-called haploid type. Each neural network variable x_i is the weight and the neuron shift and encoded by a certain fragment of the chromosome (see Fig. 4) in the form of a sequence of zeros and ones. These fragments go to the chromosome one after another and do not have start and end markers, and yet, when decoding the chromosome into a variable vector, the same mapping mask is used throughout the simulated evolution period. Such chromosomes are randomly generated by sequentially filling the digits (genes)

by zero or one, and any subsequent chromosome changes in the population are associated with a change in genetic information and only then decoded into the parameters of an artificial neural network.

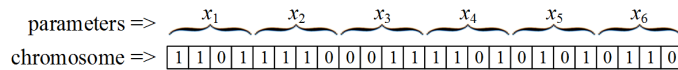


Fig. 4. The simplest mapping mask of the chromosome for 6 parameters

In principle, to decode genetic information from a binary form into a decimal one, any binary-decimal code is suitable, but it is usually assumed that it is represented in the Gray code [8]. For each parameter of the neurocontroller, the left and right limits of the range of this parameter change and the number of bits (genes) N encoding the parameter are set. The Gray code has advantages over the binary-coded decimal code, which, at some coincidence, generates idiosyncratic deadlocks for the search process. If we involve geometric interpretations, the Gray code ensures that two adjacent points belonging to one of edge vertices of the hypercube on which the search is performed are always decoded into two nearest points in the space of real numbers, spaced apart by one discrete of precision. Binary-decimal code does not possess such a property.

The above described approach is applied for synthesis of the control system of traction ED which represents "converter—motor of sequential excitation".

The main feature of the sequential excitation motor is the connection of the excitation winding in series with the armature winding, which in turn necessitates the consideration of the nonlinear dependence of the magnetic flux of the motor on the excitation current equal to the armature current.

Equations describing the behavior of the ED with a sequential excitation motor are given below.

$$U_{\text{ctrl}} = K_u \cdot W_2 \cdot f(W_1 \cdot U + B_1) + B_2, \quad (2)$$

where U_{ctrl} is the control voltage of a thyristor converter produced by a neural network, K_u is the coefficient that matches the output voltage of the neural network and the input voltage of the thyristor converter, f is the activation function, W_1 , W_2 are the matrices of weight coefficients of the neurons of the hidden and output layers of the neural network and B_1 , B_2 are the matrices of shifts of neurons of the hidden and output layers of the neural network. Finally

$$U = \begin{vmatrix} U_{\text{set}} \\ \omega_i \\ \omega_{i-1} \end{vmatrix}$$

is the matrix of input signals of a neural network, the components of which are: U_{set} is the speed set signal, ω_i is the current value, and ω_{i-1} is the previous value of the motor speed obtained by speed feedback.

The processes in the thyristor converter are described by equation

$$T_{tc} \cdot \frac{dE_d}{dt} + E_d = K_{tc} \cdot U_{ctrl}, \quad (3)$$

where T_{tc} is the time constant of the thyristor converter, E_d is the rectified emf of the thyristor converter, K_{tc} is the gain of the thyristor converter and t is the time.

The magnetization curve of the motor is described in the form of a nonlinear equation

$$F = f(I_a), \quad (4)$$

where F is the motor flux generated by the excitation winding and I_a is the current flowing through the winding of the motor armature.

Equation of the power electrical circuit reads

$$U_a = (R_a + R_e) \cdot I_a + (L_a + L_e) \cdot \frac{dI_a}{dt} + w_a \frac{dF}{dt}, \quad (5)$$

where U_a is the voltage supplying the armature winding, R_a , R_e are the active resistances of armature and excitation windings, respectively, L_a , L_e are the inductances of armature and excitation windings, respectively, and w_a is the number of turns of the excitation winding.

Equation of electromechanical transformation in the motor can be written as

$$M = K \cdot F \cdot \omega \quad E_{emf} = K \cdot F \cdot I_a, \quad (6)$$

where K is the constructive coefficient of the electrical machine.

Equation of motion is given as

$$J \cdot \frac{d\omega}{dt} = M - M_c, \quad (7)$$

where J is the total moment of inertia of the motor armature and the moment of inertia of the mechanism, reduced to the speed of the shaft of the electric machine and M_c is the load torque on the electric motor of the "friction pair" type.

Based on equations (2)–(7), a structural diagram is constructed (see Fig. 5).

4. Obtained results and their analysis

To control the system, a neural network of the form NN 3–10–1 with sigmoidal alternating activation functions of the neurons of the hidden layer (see Fig. 3) and linear ones of the neurons of the output layer was chosen. For normal operation of the system, a neural network must be trained. The system was trained by the genetic algorithm using the Mendel 4 program (<https://sites.google.com/site/kvmahotilo/mendel>). The following parameters of the genetic algorithm were selected:

- sampling pressure ratio – 10 %,
- parent group – 100 %,
- average number of crossovers – 1,

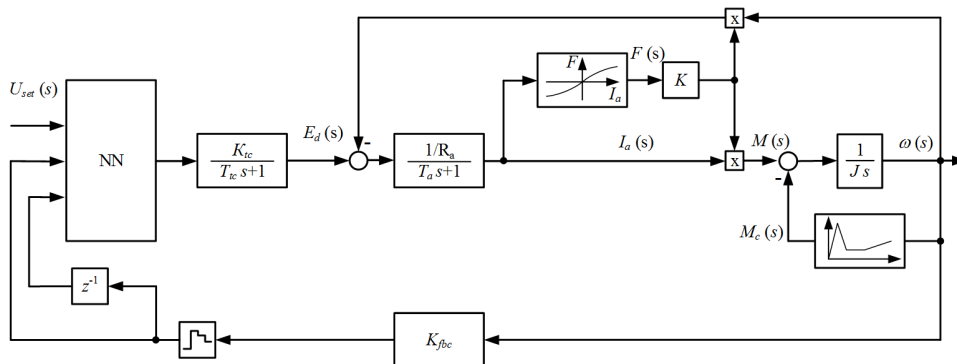


Fig. 5. Structural diagram of a neural network control system for a DC motor of sequence excitation

- probability of gene mutation – 0.004,
- probability of translocation – 0.005,
- probability of inversion – 0.002.

The neural network was trained according to the procedure described above, while the criterion [9] was chosen as an optimization:

$$F = \frac{1}{T_{\max} \cdot N} \cdot \sqrt{\int_0^{T_{\max}} [(\omega_{\text{set}} - \omega_{\text{av}}) \cdot t]^2 dt}, \quad (8)$$

where T_{\max} is the duration of the transient of the system, N is the number of test signals, ω_{set} and ω_{as} are the set and actual value of the motor speed, respectively.

The training was done on a personal computer with a CPU type Intel Core i7 with a clock frequency of 3 GHz. As test signals $|\pm 1 \pm 0.8 \pm 0.6 \pm 0.4 \pm 0.2 \ 0| \cdot \omega_r$, where ω_r is the rated motor speed, were chosen. The total calculation time was 02:03:31, while the number of calculations of the objective function is 337373, and the minimum criterion value (8) is 5.7923104391986.

Figures 6 and 7 show the transients of starting the ED of an ARP14 electric locomotive with open and neural network control systems, respectively, and a DC motor of sequential excitation of ET23.5. An intensity adjuster is applied to limit the coordinates.

The neural network control system provides the following quality control indicators:

- regulation time ≈ 0.25 s,
- overregulation $\approx 6.7\%$,
- regulation error $\approx 0.11\%$,
- maximum armature winding current ≈ 172 A,
- maximum motor torque ≈ 657 Nm.

The required control law was synthesized using a single easily measured feedback on the speed of the motor which does not create difficulties in the physical implementation of the system.

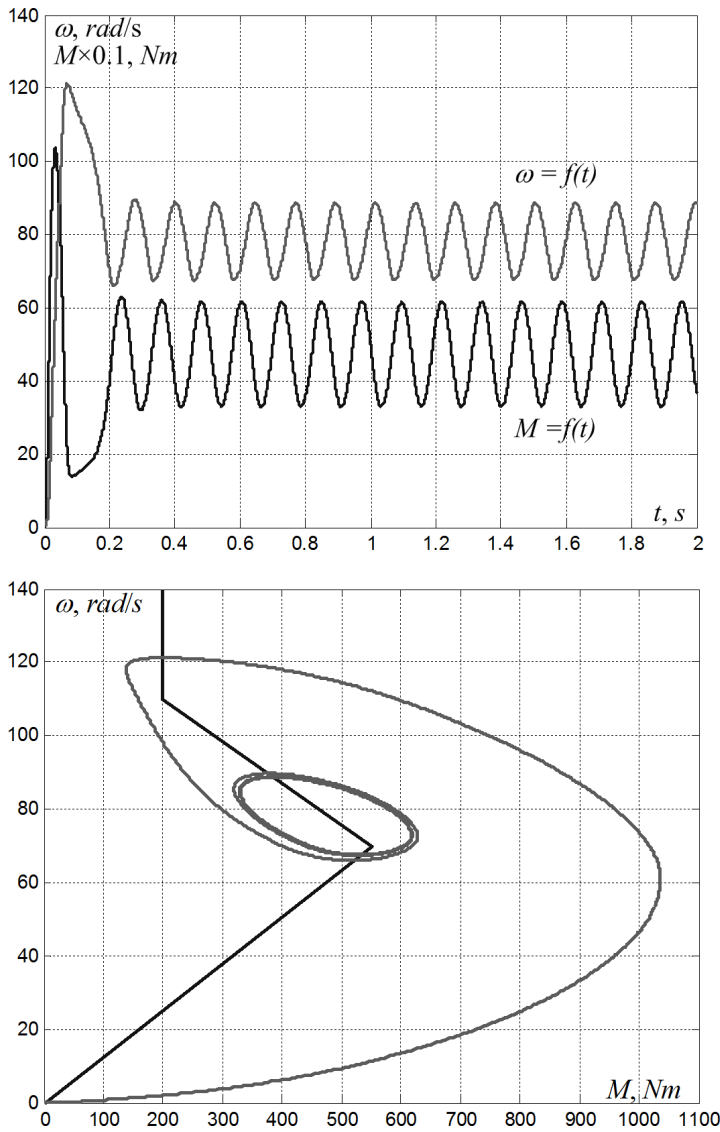


Fig. 6. Transients and mechanical characteristics of the open system

The use of induction short-circuited motors in the movement mechanisms whose speed is regulated by a transistor frequency converter is primarily due to the advantages of an induction motor in comparison with a DC motor. Such systems are used in urban electric transport and, in particular, in the ED of trams [10].

Figure 8 shows the static mechanical characteristics of the traction induction electric motor of the tram type AD927A (Fig. 8a), the transients (Fig. 8b), the graphs of the change in the linear speed (Fig. 8c), and the acceleration (Fig. 8d) when the

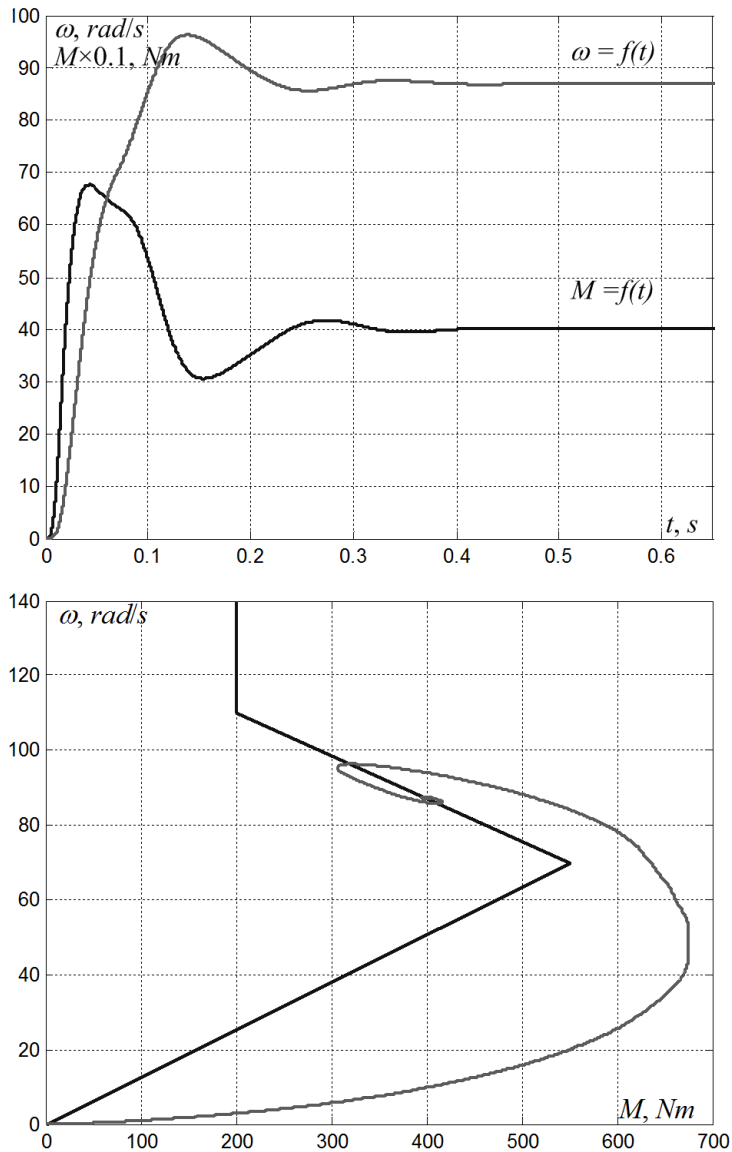
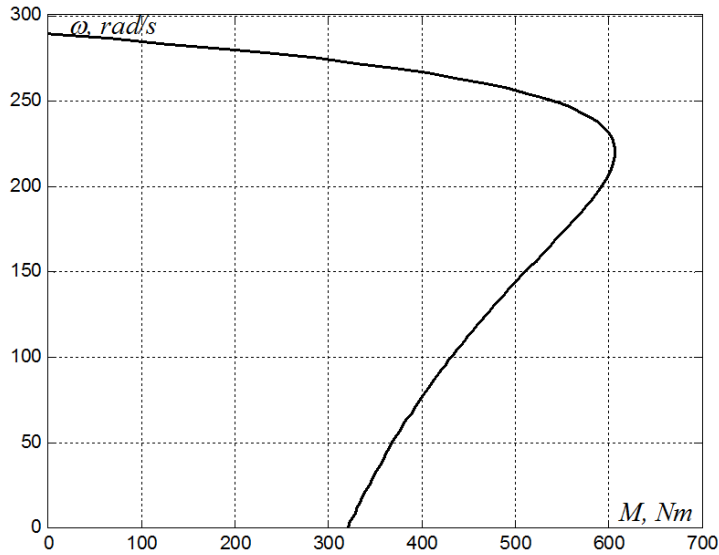


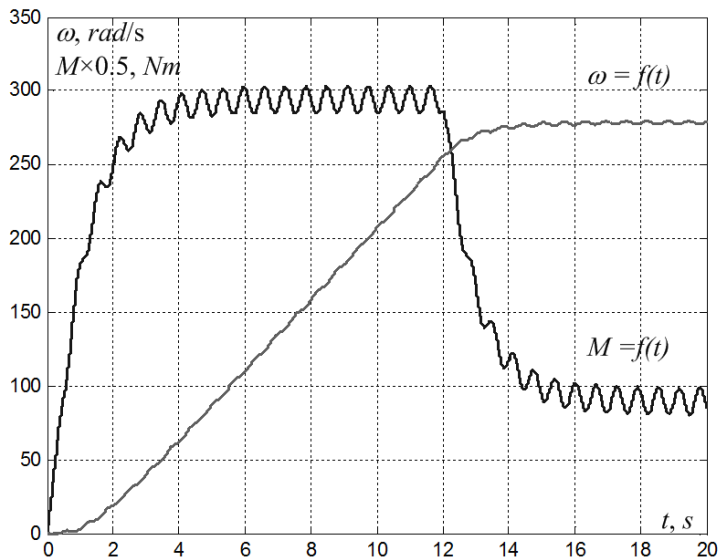
Fig. 7. Transients and mechanical characteristics of the neural network system

tram is accelerated from the intensity adjuster in the open control system. From the analysis of the presented graphs it is seen that during the acceleration of the tram to the nominal speed of movement, there are self-oscillations of the torque, speed and acceleration. This phenomenon is due to the fact that the mechanical load characteristic has a so-called "falling" section. When a working point is found, self-oscillations occur on this section, as a result of which the power consumption is

increased, the efficiency of the mechanism is reduced, its wear increases. In addition, an increase in linear acceleration to a value of 1.6–2 m/s² may lead to a drop of tram passengers which is unacceptable.



static mechanical characteristic of the traction induction motor
AD927A



transients in the traction induction motor AD927A

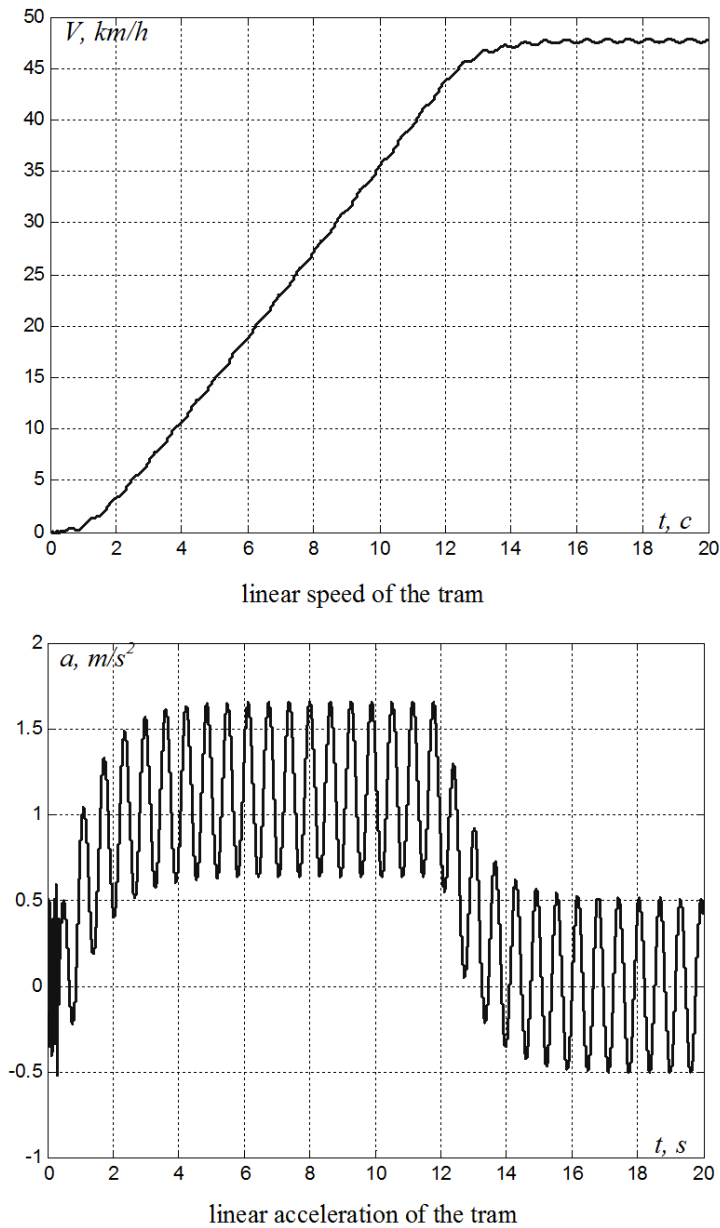


Fig. 8. Characteristics of the open control system of the traction induction electric motor of a tram

To ensure a qualitative start-up process and exclude auto-oscillations, a closed system using a neuroregulator was synthesized, see Fig. 9.

To construct a closed control system, we used a neuron network of the perceptron

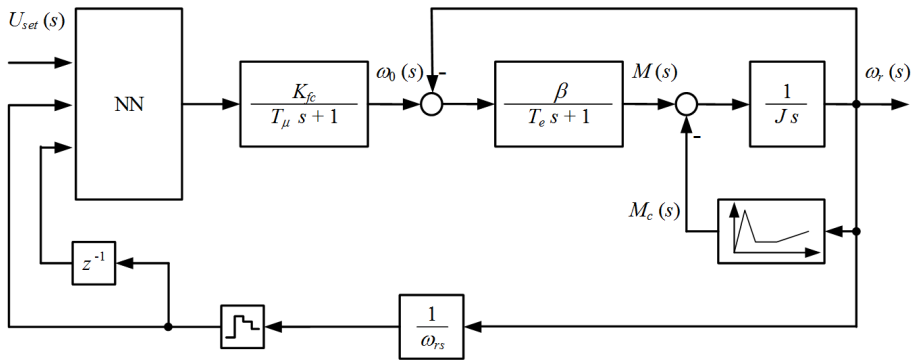


Fig. 9. Structural diagram of a closed neural network control system for the traction induction electric motor of the tram electric drive

type NN3-10-1 with sigmoidal alternating activation functions of the neurons of the hidden layer and a linear activation function of the output neuron. The input of such a neural network is fed with an input signal vector consisting of a control signal from the intensity adjuster necessary to limit the coordinates of the electric drive, the current value of the feedback signal on speed of the motor discretized in time (the discretization period is $T_0 = 0.01$ s) and the previous value of the signal of speed of the electric motor obtained by means of the digital link of pure delay. As earlier investigations shown [9–11], the choice of such a neural network is optimal for controlling single-mass and two-mass electromechanical systems. The output signal of the neural network is used as a signal for setting the frequency of the supply voltage of the traction induction motor generated by the frequency converter. The training of this neural network was carried out in exactly the same way as for ED with a DC motor of sequential excitation and using the same criterion (8).

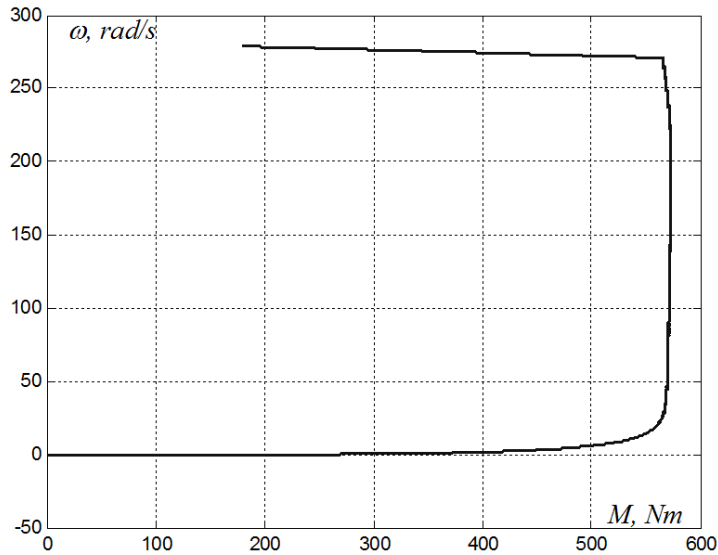
Training was carried out on a personal computer with a CPU type INTEL Core i7 with a clock frequency of 3 GHz. As test signals, we chose $|\pm 1 \pm 0.8 \pm 0.6 \pm 0.4 \pm 0.2| \omega_r$, where ω_r is the rated motor speed. The total computation time was 17 min 21 s, while the number of calculations of the objective function was 20000, and the minimum criterion value was 2.07. Figure 10 shows the dynamic characteristics of the traction induction when the tram is accelerated from the intensity adjuster in a closed neural network control system.

5. Conclusion

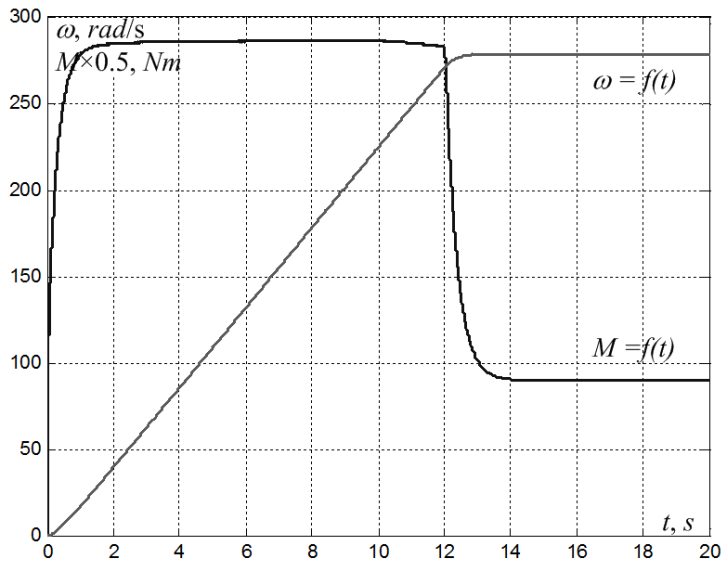
As can be seen from the obtained graphs, on the basis of neural networks it is possible to build a closed electric drive control system for the ARP14 electric locomotive with a higher quality of coordinate adjustment, in comparison with traditional systems. Here, the following values were achieved: regulation time 0.3 s, overregulation 7.8%, static regulation error 1, maximum motor torque 654 Nm.

For the closed control system of the traction induction electric motor of the tram, the use of a directional three-layer neural network of the "perceptron" type

with sigmoidal alternating activation functions of the hidden layer neurons makes it possible to exclude the occurrence of oscillatory dynamic modes. Acceleration of the tram to the nominal speed of movement takes place within an acceptable time, which is 12 to 13 s, and the acceleration does not exceed 1.15 m/s^2 , which provides a higher level of passenger comfort.



dynamic mechanical characteristic of the traction induction motor
AD927A



transients in the traction induction motor AD927A

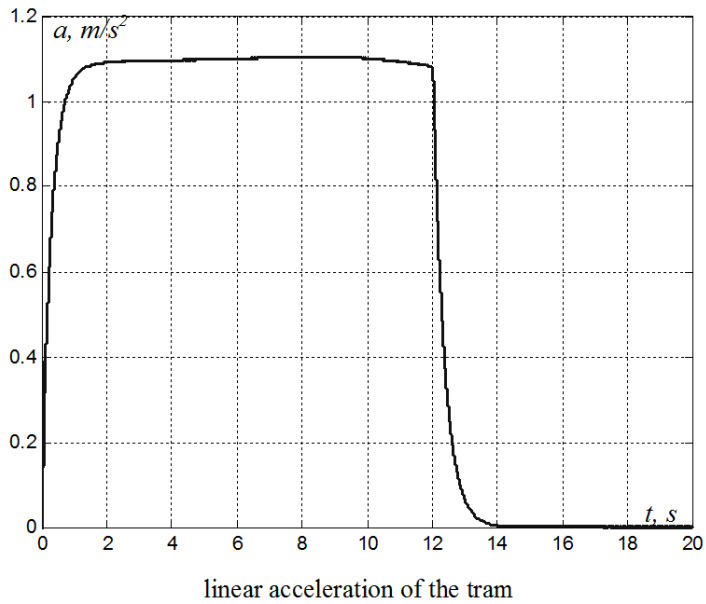
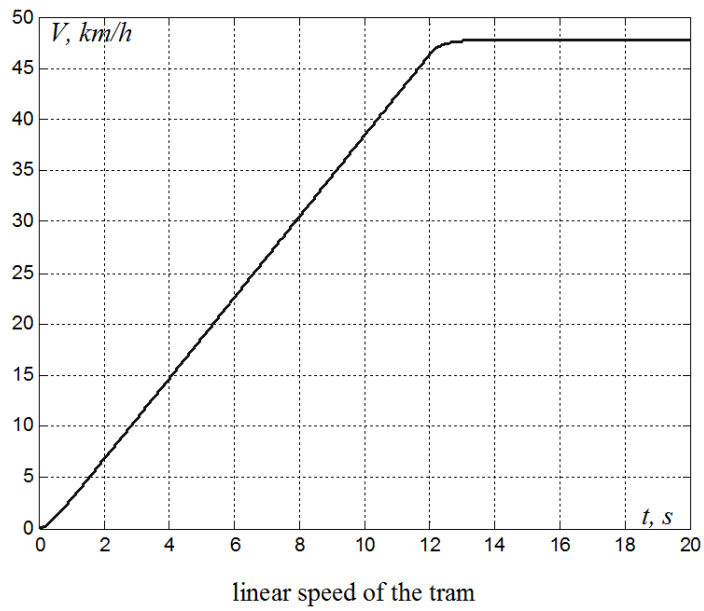


Fig. 10. Characteristics of the closed neural network control system of the traction induction electric motor of a tram

References

- [1] L. V. AKIMOV, V. T. DOLBINA, V. B. KLEPIKOV, A. V. PIROZHOK: *Synthesis of simplified structures of two-mass electric drives with nonlinear load (Sintez uproshchennykh struktur dvuchmassovykh elektroprivodov s nelinejnoy nagruzkoy)*. Editor V.B. Klepikov, KhPI, Kharkiv, ZNYU, Zaporizhzhia, 2002, 160 p. (in Russian).
- [2] K. P. VLASOV: *Theory of automatic control (Teoriya avtomaticheskogo upravleniya)*. Tutorial, Publishing house Humanitarian Center, Kharkiv, 2007, 322 p. (in Russian).
- [3] V. T. DOLBINA: *Topological methods of analysis and synthesis of electrical circuits and systems (Topologicheskie metody analiza i sinteza elektricheskikh cepej i sistem)*. High school. Publishing house at Kharkiv University, Kharkiv, 1974, 145 p. (in Russian).
- [4] A. I. GALUSHKIN: *The theory of neural networks, Book 1 (Teoriya nejronnykh setej, Kniga 1)*. Textbook for high schools, Publishing house IRPZh, Moscow, 2000, 416 p. (in Russian).
- [5] K. A. DE JONG: *Genetic algorithms: a 10-year perspective*. Applied Mathematical Modelling 35 (2011), No. 10, 4679–4714.
- [6] V. B. KLEPIKOV: *Features of the dynamics of electromechanical systems with negative viscous friction (Osobennosti dinamiki elektromekhanicheskikh sistem s otricatel'ny'm vjazkim treniem)*. Topical issue "Problems of modern electrical engineering", 2000, 40–45 (in Russian).
- [7] D. E. RUMELHART, G. E. HINTON, R. J. WILLIAMS: *Learning representation by back-propagation errors*. Nature 323 (1986), 533–536.
- [8] G. K. VORONOVSKY, K. V. MAKHOTILO, S. N. PETRASHEV, S. A. SERGEEV: *Genetic algorithms, artificial neural networks and problems of virtual reality (Geneticheskie algoritmy, iskusvennye nejronnye seti i problemy virtual'noj real'nosti)*. OSNOVA, Kharkiv, 1997, 112 p. (in Russian).
- [9] I. V. OBRUCH, YU. N. KUTOVYI: *Neural network control system for electric locomotive electric drive (Nejrosetevaja sistema upravlenija elektroprivoda elektrovoza)*. Electrotechnical and Computer Systems 91 (2014), No. 15, 132–35 (in Russian).
- [10] I. V. OBRUCH, YU. N. KUTOVYI: *Neural network control system for the electric drive of the ARP14 electric locomotive taking into account the elasticity of the kinematic connections (Nejrosetevaja sistema upravlenija elektroprivoda elektrovoza ARP14 s uchotom uprugosti kinematicheskikh svyazej)*. Journal of the National Technical University "Kharkiv Polytechnic Institute" 1121 (2015), No. 12, 248–250 (in Russian).
- [11] V. B. KLEPIKOV, S. A. SERGEEV, K. V. MAKHOTILO, I. V. OBRUCH: *Application of methods of neural networks and genetic algorithms in solving problems of control of electric drives (Primenenie metodov nejronnykh setej i geneticheskikh algoritmov v reshenii zadach upravlenija elektroprivodami)*. Electrical Engineering (1999), No. 5, 2–6 (in Russian).

Received April 8, 2018

Electromagnetic and thermal transients during induction heating of cylindrical workpieces¹

YEVGEN I. BAJDA¹, BORYS V. KLYMENKO¹,
MICHAEL G. PANTELYAT¹, DIDIER TRICHET²,
GUILLAUME WASSELYNCK²

Abstract. Accuracy of computer simulations of coupled electromagnetic and thermal multiphysics processes during induction heating of metals depends strongly on the correct account of peculiarities of electromagnetic and thermal transients in heated workpieces. The paper is devoted to numerical modelling of such phenomena in axisymmetrical formulation. Illustrative numerical results obtained during the benchmark problem solution regarding induction heating of aluminum tube taking into account convective and radiant heat transfer from the workpiece's surface are presented and analyzed.

Key words. Induction heating, numerical modeling, electromagnetic field, thermal field, transients.

1. Introduction, problem definition, novel contributions of the paper

There is a lot (at least, hundreds or even thousands) of publications devoted to computer simulations of various induction heating devices and technologies. The goal of this paper is to consider selected aspects of induction heaters numerical analysis that were not given sufficient attention in the papers by other authors.

Numerical modelling of the process of induction heating of metal workpieces regarding various technological processes and objects is carried out as follows: equations of the electromagnetic field in the complex form [1–8 and many others] (or,

¹Department for Electrical Apparatus, National Technical University "Kharkiv Polytechnic Institute"; e-mails: m150462@yahoo.com, b.v.klymenko@gmail.com

²IREENA, Polytech'Nantes, University of Nantes, 37 Boulevard de l'Université BP406 44600 Saint-Nazaire, France; e-mails: didier.trichet@univ-nantes.fr, guillaume.wasselynck@univ-nantes.fr

sometimes, transient equations [9]) and the transient heat transfer equation are solved in the coupled (multiphysics) formulation with corresponding boundary conditions. The complex electromagnetic quantities (phasors) and corresponding equations [2–8] are used to describe the most widely known and applied induction heaters with traditional sinusoidal AC excitation currents in the inductor. In its turn, transient equations of the electromagnetic field are solved to simulate relatively new and rarely used technological process of induction heating based on, for example, non-sinusoidal multiple capacitor discharges to the inductor [9].

Solving the electromagnetic field equations in the complex form, the authors of most of papers [2–8] consider the steady-state electromagnetic processes, i.e. they do not take into account transients when switching on the excitation current in the inductor. However, the authors of this paper suppose that it is interesting to investigate the influence on the electromagnetic and thermal characteristics of the inductor heaters of electromagnetic transients taking place at the AC current switching on. To do this, it is proposed to solve transient equations of the electromagnetic field for the first time points after switching on the induction heating device's sinusoidal excitation.

Accuracy of the computer simulation depends strongly on such a factor as the correct choice of boundary conditions of the electromagnetic and thermal problems. Regarding the boundary conditions of the electromagnetic field equations, it is important and interesting to compare various ways of imitation of the infinity of the ambient space around the objects (inductor-workpiece system). As a rule, the space occupied by ambient air is limited by using a finite region with zero conditions on its external boundaries. Another and insufficiently investigated approach is to use the Kelvin transform described in [10]. The comparison of both mentioned techniques is the next aim of this paper.

At the thermal field distribution computing the correct determination of convective heat transfer coefficients is extremely important. Currently, there are no “true” techniques of the convective heat transfer coefficients determination permitting to carry out calculations of these coefficients in separate points on the heated bodies' surfaces taking into account the surface temperature, physical properties of fluid or gas around the body and other factors influencing on the heat exchange of the heated body with fluid or gas, in particular when temperatures of separate surface points differ essentially. Known from the literature techniques of the heat transfer coefficient determination propose only different ways of calculation of average values of these coefficient based on the empirical data processing [4, 5]. In many works [2, 3, 5, 9, etc.] the value of the convective heat transfer coefficient is assumed to be constant for all workpiece's surfaces and independent on the temperature. The authors of this paper propose to substitute the full-scale experiment for the heat transfer coefficients determination by the calculation of the quasi-static heat exchange process between the heated inductor and the workpiece with ambient air using the Navier-Stokes equations.

This paper is devoted to the solution of above-mentioned problems in axisymmetrical formulation using Comsol Multiphysics code according the previous comments. Illustrative numerical results obtained during a benchmark problem solution regard-

ing induction heating of aluminum tube are presented and analyzed.

The novel contributions of this paper are the following:

- Numerical investigations of the influence on the electromagnetic and thermal characteristics of the inductor heaters of electromagnetic transients taking place at the AC current in the inductor switching on are carried out.
- The comparison of two ways of imitating infinity of the ambient space around the inductor-workpiece system (using a finite region with zero conditions on its external boundaries and utilization of the Kelvin transform) is carried out.
- Validation of the electromagnetic calculations correctness by the Comsol Multiphysics code is carried out.
- A technique for the convective heat transfer coefficients determination by the calculation of the quasi-static heat exchange process between the heated inductor and the workpiece with ambient air using the Navier-Stokes equations is proposed and used.

We consider problems of calculation of electromagnetic and thermal processes in the “inductor-workpiece” system where a circular aluminum tube is a workpiece, and a circular turn coaxial with workpiece and made from copper is an inductor (see Fig. 1).

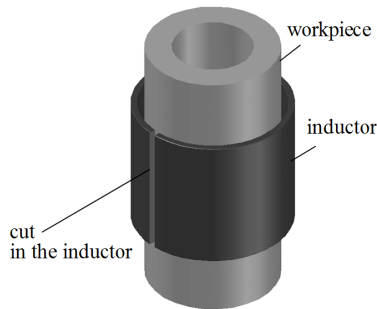


Fig. 1. Inductor and workpiece

Current in the inductor is excited by AC sinusoidal voltage with frequency of $f = 8$ kHz supplied from an external source to opposite planes of the thin cut in the inductor. Current in the workpiece is excited by electromagnetic induction. The amplitude value U_m of the voltage applied to the inductor should be such that in the steady-state mode amplitude of current in the inductor will equal to 10 kA.

Dimension of the inductor and the workpiece in mm are indicated in Fig. 2. This figure also shows the axes used in the solution of axisymmetric problems.

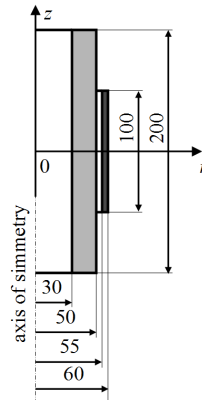


Fig. 2. Dimensions (in mm) of inductor and workpiece

2. Calculation of electromagnetic transients in inductor-workpiece system

2.1. Assumptions

a) Inductor is considered as a closed circular turn. As a result calculation problems are simplified to 2D axisymmetric problems in the cylindrical coordinate system r, z, θ with corresponding unit vectors $\mathbf{1}_r, \mathbf{1}_z, \mathbf{1}_\theta$.

b) To the inductor the following sinusoidal voltage u is applied:

$$u = U_m \cdot \sin(2 \cdot \pi \cdot f \cdot t + \psi),$$

where f is the frequency (8 kHz) and ψ is the initial phase of the voltage which is chosen from the condition of the maximal duration of transient.

c) Ambient medium is air with temperature $\vartheta_a = 20^\circ$. At the start of transient, both inductor and workpiece have the same temperature.

d) Magnetic permeabilities of inductor, workpiece and air are assumed to be equal to magnetic permeability of vacuum $\mu_0 = 4\pi \cdot 10^{-7}$ H/m.

e) Displacement currents are extremely small and neglected in the comparison with conduction currents.

f) As the thermal processes in this system are essentially more inertial than electromagnetic ones, temperatures of the inductor and the workpiece have no time to be changed during the electromagnetic transient. Therefore, we assume that resistivities ρ of the materials of the inductor and workpiece equal to values referred to the ambient air temperature: $\rho_1 = 1.67 \cdot 10^{-8}$ Ω m, $\rho_2 = 2.64 \cdot 10^{-8}$ Ω m. Here, index 1 corresponds to the inductor (copper), index 2 corresponds to the workpiece (aluminum). The corresponding values of conductivities equal to $\sigma_1 = 0.600 \cdot 10^8$ S/m, $\sigma_2 = 0.378 \cdot 10^8$ S/m, respectively. Conductivity of air is assumed to be equal zero ($\sigma_0 = 0$).

2.2. Differential equations to be solved

In the general case, the partial differential equation of the electromagnetic field in the terms of the magnetic vector potential \mathbf{A} in the arbitrary object obtained from the Maxwell equations is the following [11]:

$$\sigma \cdot \frac{\partial \mathbf{A}}{\partial t} + \text{curl}(\mu^{-1} \cdot \text{curl} \mathbf{A}) = \sigma \cdot \mathbf{E}, \quad (1)$$

where σ is the conductivity of the considered object's material, μ is the magnetic permeability of the object's material that equals μ_0 (see assumption (d)), and \mathbf{E} is the vector of the external electric field strength generated in the object by the external source.

In the regions occupied by air and the workpiece there are no external sources of the electric field strength, therefore in these regions $\mathbf{E} = \mathbf{0}$. To the inductor voltage u is applied, and vector of the electric field strength in the region occupied by the inductor is perpendicular to the plane passed through the axis of symmetry, therefore for this region vector \mathbf{E} will be equal:

$$\mathbf{E} = \frac{u(t)}{2 \cdot \pi \cdot r} \cdot \mathbf{1}_\theta, \quad (2)$$

where r is the distance from the axis of symmetry to the arbitrary point in the region of the inductor.

As a result, we obtain a system of three equations corresponding to three regions—the inductor, the workpiece and ambient air:

$$\sigma_1 \cdot \frac{\partial \mathbf{A}}{\partial t} + \text{curl}(\mu_0^{-1} \cdot \text{curl} \mathbf{A}) = \sigma_1 \cdot \frac{u(t)}{2 \cdot \pi \cdot r} \cdot \mathbf{1}_\theta \quad (\text{inductor}), \quad (3)$$

$$\sigma_2 \cdot \frac{\partial \mathbf{A}}{\partial t} + \text{curl}(\mu_0^{-1} \cdot \text{curl} \mathbf{A}) = \mathbf{0} \quad (\text{workpiece}), \quad (4)$$

$$\text{curl}(\text{curl} \mathbf{A}) = \mathbf{0} \quad (\text{air}). \quad (5)$$

The considered problem is axisymmetric, therefore the magnetic vector potential \mathbf{A} determined as a result of the solution of the differential equations of the electromagnetic field has the only azimuthal component A_θ which further will be marked as A ($\mathbf{A} = A_\theta \cdot \mathbf{1}_\theta = A \cdot \mathbf{1}_\theta$) which is the module of the vector \mathbf{A} and depends on two coordinates r and z only. So, the system of equations in terms of the vector \mathbf{A} is simplified to the system of 2D equations for the scalar A in the cylindrical coordinate system. These equations are very bulky and they are not presented here, especially as their solution is carried out by the Finite Element Method using the Comsol Multiphysics code which at the correct initial data proceeds the necessary transforms itself.

Initial data for numerical simulation follows:

- problem description (carried out by the choice from the proposed menu),

- regions' geometry description (main points connected by line segments or by arcs of circles),
- material characteristics (properties) for the corresponding regions,
- boundary conditions.

2.3. Geometry of regions and boundary conditions

Geometry of the inductor and the workpiece is input as rectangular regions in the plane rz , inductor's corner points have a rounding with radius of 0.5 mm, and ambient air represents an infinite space. At the solution of such problems by numerical methods, usually it is necessary to limit the space occupied by air by using a finite spherical region (see Fig. 3) with sufficiently large radius which is in 2–3 times more than objects' dimensions and with zero values of the magnetic vector potential on bounds. Such an approach gives admissible results even at the less radius of the limiting sphere if the magnetic field strength decreases quickly at the moving away from the objects. Besides, by using the Kelvin transform [10] it is possible to imitate the infinity of the ambient space around the objects, in our case around the inductor-workpiece introducing an additional spherical region (see Fig. 4) if on the surface of the limiting and additional spheres to set so called periodic conditions which, in fact, represent conditions of the field continuity. The Comsol Multiphysics code provides a possibility to use such boundary conditions.

On the axis of symmetry as boundary conditions zero Dirichlet conditions are usually used, in our case $A = 0$.

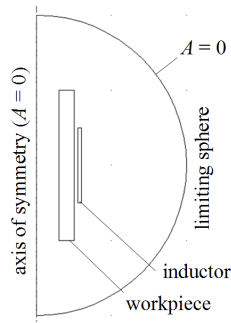


Fig. 3. Boundary conditions forming at introducing of limiting sphere

At the solution of transient electromagnetic field problems it is necessary to set initial conditions, i.e. the values of unknown quantities at some initial moment of time. In the problem under consideration the unknown quantity is the azimuthal component A of the magnetic vector potential, and its initial value $A|_{t=0}$ is assumed to be equal zero.

It is interesting to compute not only values of the magnetic vector potential A using the presented differential equations (3)–(5) and boundary conditions but also other quantities (as functions of coordinates and time) connected with magnetic vector potential, for example magnetic flux density, current density, heat sources

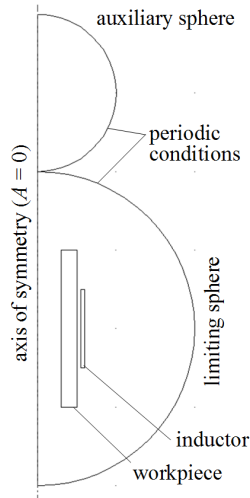


Fig. 4. Boundary conditions forming by using Kelvin transform

density, etc. as well as integral characteristics such as current, active (thermal) power, and other. Some numerical results for the problem under consideration are presented below.

Results of validation of the electromagnetic calculations correctness by the Comsol Multiphysics code are presented in Appendix A.

2.4. Results of calculations of electromagnetic transients in the inductor and workpiece

Calculations of transients have been carried out at the frequency $f = 8$ kHz of the sinusoidal voltage applied to the inductor. Amplitude of the voltage U_m has been chosen in such a way that in the steady-state mode the amplitude of the current in the inductor will be equal to 10 kA. By the selection it was determined that $U_m = 10.36$ V. Here, transients have been calculated at two above considered approaches for the boundary conditions forming—utilization of the Kelvin transform and by substitution of the infinite space by finite spherical region. Obtained results exhibit practically no difference, which can be seen in Figs. 5 and 6 presenting graphs of transient currents in the inductor and workpiece, as well as graphs of transient active (thermal) power in the inductor, respectively.

3. Calculation of electromagnetic and thermal characteristics of the inductor-workpiece system in the quasi-static mode

3.1. Assumptions

To carry out these calculations we apply the same assumption as at the solution of previous problem (see subsect. 2.1).

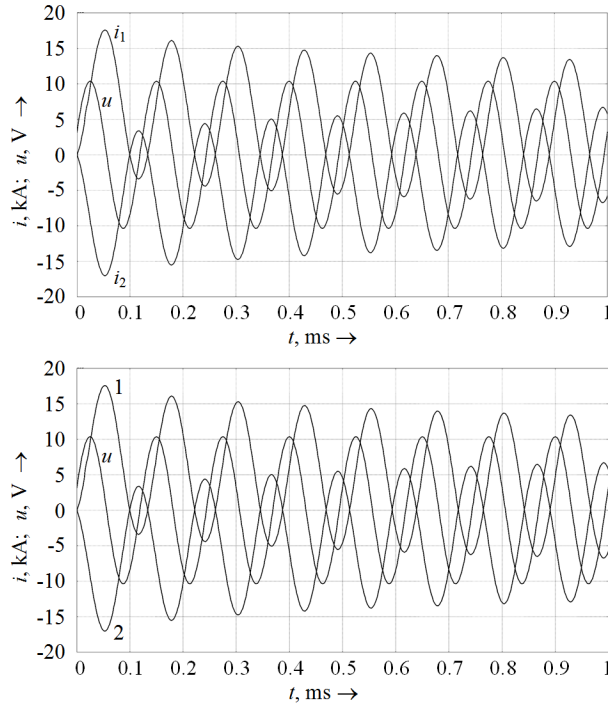


Fig. 5. Graphs of transient currents in the inductor (i_1) and the workpiece (i_2) at the sinusoidal applied voltage (u) and different approaches for the boundary conditions forming—using the Kelvin transform (left) and by substitution of the infinite space by finite spherical region (right)

3.2. Geometry of regions and boundary conditions

Geometry of the inductor and the workpiece is the same as in the previous problem (see subsect. 2.3). On the axis of symmetry and on the surface of limiting sphere as boundary conditions we assume Dirichlet zero conditions.

3.3. Differential equations to be solved

Differential equations of electromagnetic field in the inductor-workpiece system for the quasi-static mode can be obtained from (3)–(5). Here, the vector A is substituted by the complex quantity (phasor) \underline{A} , and the partial difference $\partial A/\partial t$ is substituted by the expression $j \cdot \omega A$, where j is the imaginary unit, $\omega = 2\pi f$ is the angular frequency. Besides, instantaneous voltage in (3) is substituted by the amplitude value U_m . As a result, the system of equation is written in the form:

$$j \cdot \omega \sigma_1 \underline{A} + \text{curl}(\mu_0^{-1} \text{curl} \underline{A}) = \sigma_1 \cdot \frac{U_m}{2 \cdot \pi \cdot r} \cdot \mathbf{1}_\theta \quad (\text{inductor}), \quad (6)$$

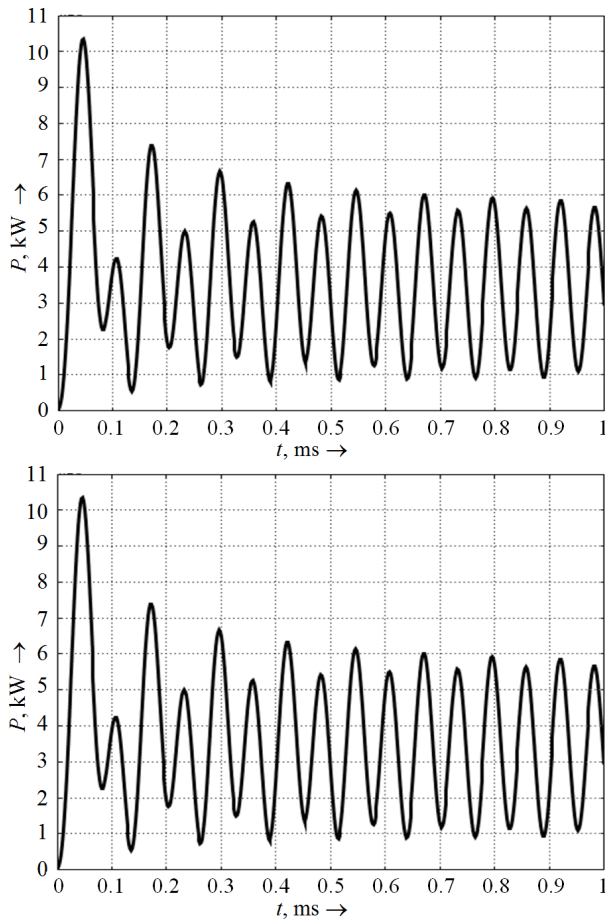


Fig. 6. Graphs of transient active (thermal) power P in the inductor at different approaches for the boundary conditions forming—using the Kelvin transform (left) and by substitution of the infinite space by finite spherical region (right)

$$\mathbf{j} \cdot \omega \sigma_2 \underline{\mathbf{A}} + \operatorname{curl}(\mu_0^{-1} \operatorname{curl} \underline{\mathbf{A}}) = \mathbf{0} \quad (\text{workpiece}), \quad (7)$$

$$\operatorname{curl}(\operatorname{curl} \underline{\mathbf{A}}) = \mathbf{0} \quad (\text{air}). \quad (8)$$

We solve the above-mentioned system of equations (6)–(8) in the terms of the complex quantity (phasor) of the magnetic vector potential $\underline{\mathbf{A}}$ and also determine another quantities (as functions of coordinates) connected with magnetic vector potential, for example magnetic flux density, current density, heat sources density, etc. as well as integral characteristics such as current, active (thermal) power, and other. Some numerical results for the problem under consideration are presented below (see sect. 3.4, Figs. 7–13).

3.4. Results of calculation of electromagnetic and thermal characteristics of the inductor-workpiece system in the quasi-static mode

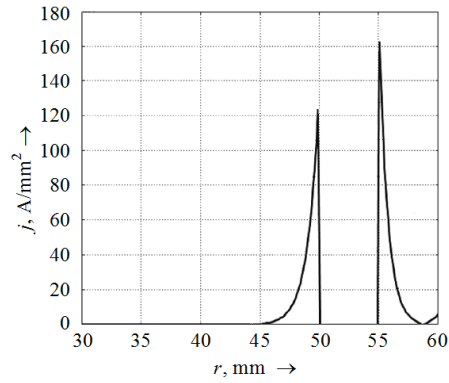


Fig. 7. Distribution of the current density module in the inductor and the workpiece along the r axis at $z = 0$ (in the middle section)

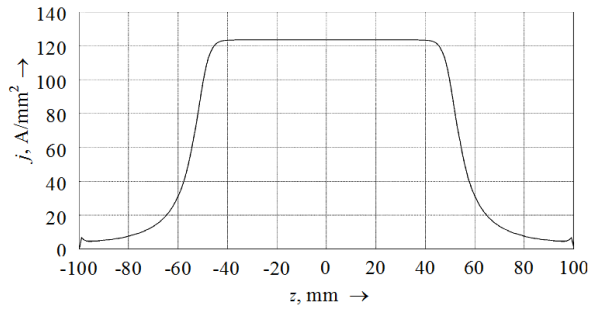


Fig. 8. Distribution of the current density module in the workpiece along the z axis at $r = 49.9$ mm (distance 0.1 mm from the workpiece's surface)

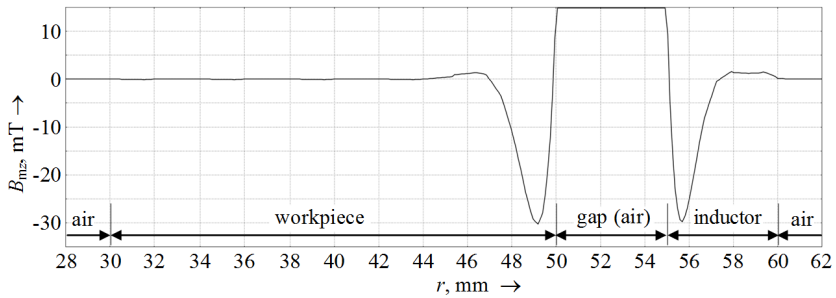


Fig. 9. Distribution of the axial component of the magnetic flux density B_{mz} in the air, inductor and workpiece along axis r axis at $z = 0$

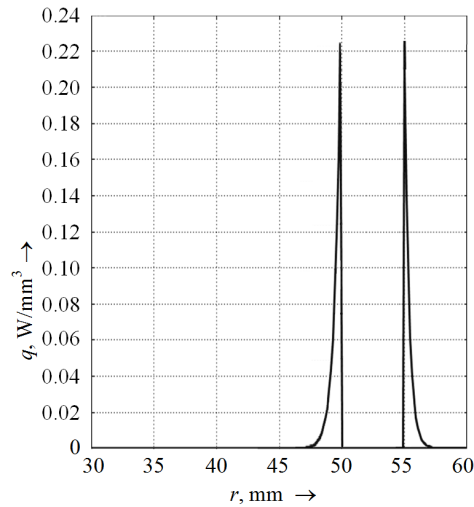


Fig. 10. Distribution of the heat sources density in the inductor and the workpiece along r axis at $z = 0$ (in the middle section)

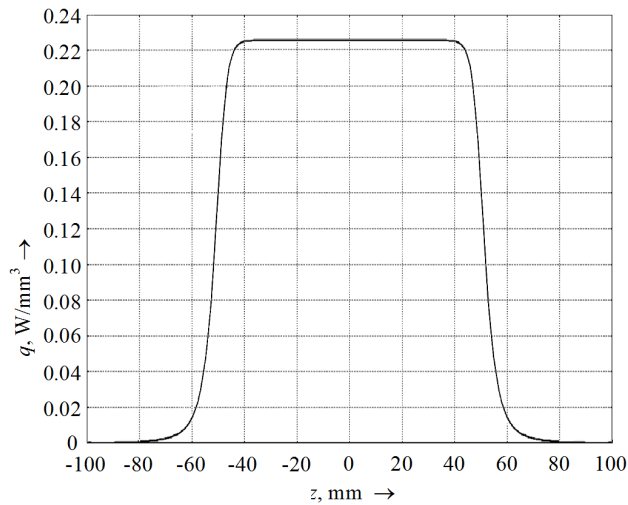


Fig. 11. Distribution of the heat sources density in the workpiece along axis z at $r = 49.9$ mm (distance of 0.1 mm from the workpiece's surface)

Finally, the computed values of some integral characteristics obtained as a result of this problem solution at the assumption that $U_m = 10.36$ V and the phase of the voltage equals to zero are the following:

- Complex value (phasor) of current in the inductor:
 $I_{m1} = 1.299 - j9.868$ kA.
- Amplitude and phase of current in the inductor:
 $I_m = 9.95$ kA, $\varphi_1 = -82.5^\circ$.

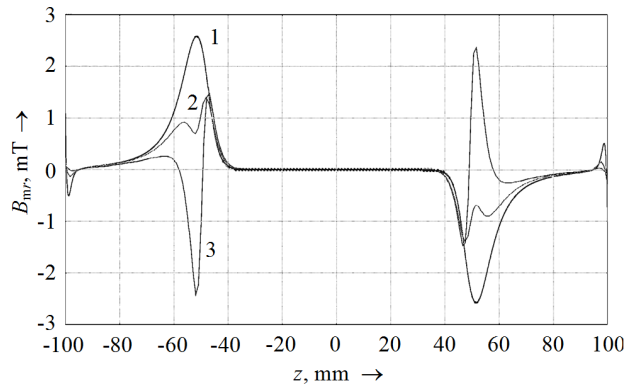


Fig. 12. Distribution of the radial component of the magnetic flux density amplitude B_{mr} along the z axis in the gap between the inductor and the workpiece on various distances a from the workpiece's surface: $a = 0$ (1—the workpiece's surface), $a = 1$ mm (2), $a = 2.5$ mm (3—in the middle of the gap)

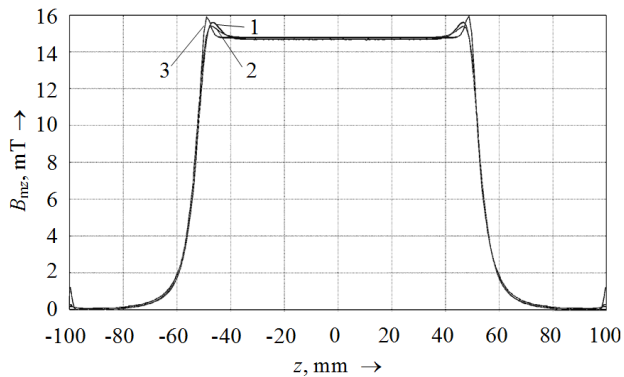


Fig. 13. Distribution of the axial component of the magnetic flux density amplitude B_{mz} along the z axis in the gap between the inductor and the workpiece on various distances a from the workpiece's surface: $a = 0$ (1—the workpiece's surface), $a = 1$ mm (2), $a = 2.5$ mm (3—in the middle of the gap)

- Complex value (phasor) of current in the workpiece:
 $I_{m2} = 1.30 + j9.712$ kA.
- Amplitude and phase of current in the workpiece:
 $I_m = 9.80$ kA, $\varphi_2 = 97.6^\circ$.
- Thermal (active) power dissipated in the inductor:
 $W_1 = 3.37$ kW.
- Thermal (active) power dissipated in the workpiece:
 $W_2 = 3.35$ kW.
- Active power consumed from the source:
 $W = W_1 + W_2 = 6.72$ kW.

4. Calculation of the workpiece's heating transient process

4.1. Assumptions

a) As appears from results of the electromagnetic problem solution presented in section 3, in the inductor and the workpiece approximately the same values of powers are dissipated but the inductor is heated more extensively because the inductor's sizes are essentially less than workpiece's ones. Therefore, in the real induction heaters the forced cooling of inductors is used which permits to hold the inductor's temperature on the given level. In the problem definition this temperature is not given. Let us assume this temperature equal to 100 °C because in order to guarantee lower temperatures the increase of the quenching fluid consumption is required, and at higher temperatures the material's strength characteristics become worse.

b) The workpiece's heating transient is considered as a multiphysics problem which solution represents the coupled solution of electromagnetic and thermal problems.

c) The thermal problem is considered as a problem of calculation of the workpiece's transient temperature field with distributed internal heat sources which density is taken from the electromagnetic problem solution. At the thermal problem solution the temperature dependencies of the specific thermal conductivity λ and the specific heat capacity c are taken into account.

d) Electromagnetic problem (EM problem—a problem of the electromagnetic field calculation in the inductor-workpiece system) is considered as quasi-static because the conventional time constant of the electromagnetic transient (order 10^{-3} s) is much less than the conventional time constant of the thermal transient (order 10^3 s). At the electromagnetic problem solution the nonlinear dependence of the workpiece's material (aluminum) resistivity is taken into account. Values of resistivity are taken from the thermal problem. The resistivity of the inductor's material (copper) is taken as a constant corresponding the value accepted in the assumption (a).

e) At the electromagnetic problem solution we suppose that displacement currents are extremely small and neglected in the comparison with conduction currents.

4.2. Differential equations to be solved

The system of partial difference equations consists of the electromagnetic field equations for the quasi-static state in the inductor-workpiece system and the transient heat transfer equation (the Fourier equation) [12] for the workpiece:

$$\mathbf{j} \cdot \omega \sigma_1 \underline{\mathbf{A}} + \operatorname{curl}(\mu_0^{-1} \operatorname{curl} \underline{\mathbf{A}}) = \sigma_1 \cdot \frac{U_m}{2 \cdot \pi \cdot r} \cdot \mathbf{1}_\theta \quad (\text{inductor}), \quad (9)$$

$$\mathbf{j} \cdot \omega \sigma_2 \underline{\mathbf{A}} + \operatorname{curl}(\mu_0^{-1} \operatorname{curl} \underline{\mathbf{A}}) = \mathbf{0} \quad (\text{workpiece}), \quad (10)$$

$$\operatorname{curl}(\operatorname{curl} \underline{\mathbf{A}}) = \mathbf{0} \quad (\text{air}), \quad (11)$$

$$c \cdot \gamma \cdot \frac{\partial \vartheta}{\partial t} + \operatorname{div}(-\lambda \cdot \operatorname{grad} \vartheta) = q \quad ((\text{thermal problem, workpiece})). \quad (12)$$

The significance of symbols in equations (9)–(11) is the same as in equations (6)–(8). In (12), ϑ denotes the temperature and q stands for the volumetric heat sources at a specific point depending on the coordinates r and z of this point as well as on time t . Parameters c , γ and σ are generally functions of the temperature and these functions for copper and aluminum are presented in Appendix B.

This problem like the previous ones is considered axisymmetrical and solved in the cylindrical coordinate system r, z, ϑ with the corresponding unit vectors $\mathbf{1}_r, \mathbf{1}_z, \mathbf{1}_\theta$. The system of the partial differential equations (9)–(12) should be, in principle, supplemented with the Navier-Stokes equations describing heating and movement of fluid (gas) around the heated solids. However, our experience with the Comsol Multiphysics code utilization demonstrates, that at the transient multiphysics problems solution together with Navier-Stokes equations, a bad convergence and even “sticking” of the numerical computation process take place frequently. Therefore, we simplified the simulation of the workpiece heating processes by the system of equations presented above, and the heat transfer with ambient air has been taken into account by assignment of some boundary conditions on the workpiece’s surface.

4.3. Boundary conditions

The inductor’s and workpiece’s geometry, solution area, and boundary conditions at the solution of the quasi-static electromagnetic problem are considered in sect. 2, 3. It is necessary to assign initial conditions (temperature values at all workpiece’s points at the initial moment of time) as well as boundary conditions, i.e., thermal state’s conditions on the workpiece’s surfaces. As above it was supposed that the ambient medium is air with temperature $\vartheta_a = 20^\circ\text{C}$, we assume this value as initial temperature values.

Ways of the boundary conditions assignment at the electromagnetic problem solution are considered in detail in the section 2. We use these boundary conditions at the solution of this multiphysical problem, too.

At the thermal problem solution on the inductor’s bound we will set the constant temperature which equals to 100°C (boundary conditions of the first kind). On the workpiece’s surfaces we will use boundary conditions of the third kind in the form

$$-\lambda \cdot \operatorname{grad}_n \vartheta = k \cdot (\vartheta - \vartheta_a), \quad (13)$$

where $\operatorname{grad}_n \vartheta$ is the normal component of the temperature gradient at an arbitrary point on the workpiece’s surface and k is the heat transfer coefficient from the workpiece’s surface at this point.

4.4. Heat transfer coefficients

The heat transfer coefficients k from the solid’s surface are usually represented as a sum of the convective k_c and radiant (k_r) heat transfer coefficients. A technique of

the determination of these coefficients used for solution of this problem is considered below.

The radiant heat transfer coefficient may be, in principle, determined from the Stefan-Boltzmann law for each point of the radiating surface if the temperature ϑ of this point, the temperature ϑ_a of the region to which the energy is radiated, and the emissivity ε of the radiating surface are known:

$$k_r = \frac{k_1 \cdot \varepsilon}{\vartheta - \vartheta_a} \left[\left(\frac{\vartheta + 273}{100} \right)^4 - \left(\frac{\vartheta_a + 273}{100} \right)^4 \right], \quad (14)$$

where $k_1 = k_B \cdot 10^8 = 5.67$ is the coefficient of radiation of the absolutely black body and $k_B = 5.67 \cdot 10^{-8} \text{ W m}^{-2} \text{ K}^{-4}$ is the Stefan-Boltzmann constant.

It is necessary to note that by using (14) it is possible to carry out estimative calculations only because in different literature sources there are essentially different values of the emissivity. For example, for rough aluminum in different sources values $\varepsilon = 0.055 - 0.07$ are presented, and for aluminum oxidated at the temperature 600°C $\varepsilon = 0.11 - 0.19$. So, the result of calculation by (14) may differ about 3.5 times. On the other hand, such a huge spread of values of the radiant heat transfer coefficient does not influence essentially the accuracy of the workpiece's heating temperature calculations, because the radiant heat transfer coefficient k_r represents only a little part of the total heat transfer coefficient. For example, for $\vartheta = 400^\circ\text{C}$, $\vartheta_a = 20^\circ$ and $\varepsilon = 0.07$, we obtain from (14) $k_r = 2.06 \text{ W}/(\text{m}^2 \text{ K})$, and values of the convective heat transfer coefficient (see below) for $\vartheta = 400^\circ\text{C}$ and $\vartheta_a = 20^\circ\text{C}$ along different parts of the workpiece's surface equal to $10 - 40 \text{ W}/(\text{m}^2 \text{ K})$. Validity of such values is sufficiently high because their determination is connected with solution of the Navier-Stokes equations which describe adequately the convective heat transfer.

At the calculation of the convective and radiant heat transfer coefficients we take into account some peculiarities of the heat transfer processes at different parts of the workpiece's surface (see Fig. 14). Here, at the determination of the radiant heat transfer coefficient for parts 1, 3, 4, 5, and 6 we assume $\vartheta_a = 20^\circ\text{C}$ (radiation to the ambient space with temperature 20°C), and for part 2 we assume $\vartheta_a = 100^\circ\text{C}$ (radiation to the internal inductor's surface), and at $\vartheta < \vartheta_a$ the value of this coefficient should be assumed negative (dissipation of the energy radiated by the inductor).

It is proposed to substitute the full-scale experiment for the heat transfer coefficients determination by the calculation of the quasi-static heat exchange process between the heated inductor and the workpiece with ambient air using the Navier-Stokes equations. Such a calculation gives a possibility to determine the average values of the heat transfer coefficient on the selected workpiece's surface parts (see Fig. 14) depending on the mean temperatures on these parts.

The technique of the determination of the convective heat transfer coefficients from separate workpiece's surface parts in the dependence on mean temperatures of these parts proposed by authors consists of the following two stages:

1. The workpiece's temperature distribution calculation is carried out by using solution of the steady-state heat transfer equation with distributed internal heat

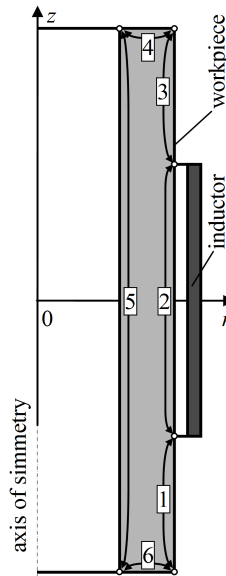


Fig. 14. Parts of workpiece's surface

sources (the Poisson equation)

$$\operatorname{div}(-\lambda \cdot \operatorname{grad}\vartheta) = q \quad (15)$$

at different values of the internal heat sources density q together with calculation of the air heating and movement by solution of the Navier-Stokes equations at the steady-state mode at $\vartheta_a = 20^\circ\text{C}$ and at the temperature on the inductor's bounds of 100°C .

2. As a result of the temperature distribution calculation for part i on the workpiece's surface we determine mean temperatures ϑ_i and corresponding values of the temperature differences $\theta_i = \vartheta_i - \vartheta_a$ as well as specific (from the surface's unit) heat fluxes q_{ni} normal to the corresponding workpiece's surface parts. Using these data, the average convective heat transfer coefficients for separate workpiece's surface parts in the dependence on the mean temperature differences of these parts are determined as

$$k_{ri}(\theta_i) = q_{ni}(\theta_i)/\theta_i. \quad (16)$$

The results of calculation of the average convective heat transfer coefficients for separate workpiece's surface parts versus the mean temperature differences of these parts are presented by dots in Fig. 15.

As it can be seen from Fig. 15, the calculated values of the average convective heat transfer coefficient change in a wide range (approximately from 4 to $43 \text{ W}/(\text{m}^2 \text{ K})$) depending on the considered workpiece's surface part and mean temperature difference) while in many works [2, 3, 5, 9, etc.] the value of the convective heat transfer coefficient is assumed to be constant (one value from the indicated range is adopted)

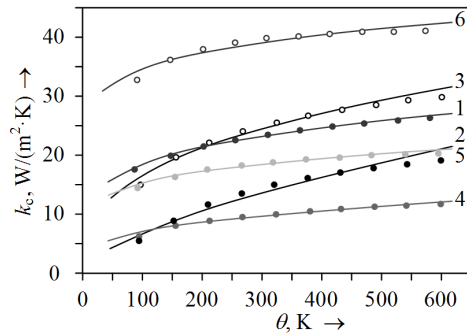


Fig. 15. Results of calculation of the average convective heat transfer coefficients for separate workpiece's surface parts versus mean temperature differences of these parts

for all workpiece's surfaces and independent on the temperature.

To carry out calculation of the workpiece's transient heating process by the differential equations system (9)–(12), the obtained (in the form of numerical data) dependencies of the convective heat transfer coefficients for separate workpiece's surface parts on mean temperature differences of these parts should be represented in the form of simple analytical functions which should be continuous and smooth (without discontinuities in the first derivative).

As such functions, power functions have been selected in the form

$$k_c = a \cdot \theta^p, \quad (17)$$

where a and p are empirical coefficients whose values for each part have been determined by the least-squares method. They are presented in Table 1.

Table 1. Values of empirical coefficients a and p for the calculation of average convection heat transfer coefficients for different workpiece's surface parts

Part No.	1	2	3	4	5	6
a	6.624	0.329	3.05	1.675	6.518	20.132
p	0.218	0.651	0.363	0.308	0.183	0.116

The results of calculations by (17) in the form of solid curves are presented in Fig. 15. It can be seen that the power function with values of empirical coefficients presented in Table 1 is satisfactorily approximated to the table values: the maximal deviation of the approximation dependencies from the table values does not exceed 8%.

4.5. Results of the workpiece's transient heating processes calculation

Computations of the transient heating processes in the workpiece (like the electromagnetic problem solutions) are carried out for the inductor supplied with a

sinusoidal voltage changing with frequency $f = 8 \text{ kHz}$ and with amplitude value $U_m = 10.36 \text{ V}$. At the electromagnetic problem solution we supposed that during the electromagnetic transient whose duration does not exceed a few ms the workpiece temperature does not change and remains equal to the ambient temperature $\vartheta_a = 20^\circ \text{C}$. However, during the duration of the workpiece's transient heating process its temperature changes from the ambient air temperature to the aluminum melting temperature $\vartheta_m = 658^\circ$, and as a result the workpiece's thermophysical properties change substantially. Here, the workpiece's resistance increases essentially resulting in the current decrease and the power ratio increase. The current decrease and power ratio increase take place in the inductor as a result of its electromagnetic interaction with workpiece despite the inductor's temperature during the thermal transient does not change and remains equal to 100°C . The temporal dependencies of currents' amplitudes, currents' mean-square values and power ratios in the inductor and the workpiece are presented in Fig. 16.

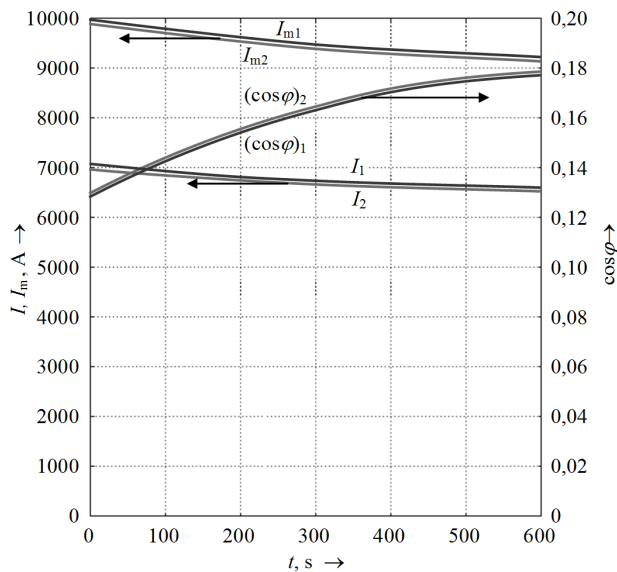


Fig. 16. Temporal dependencies of currents' amplitudes I_{m1} , I_{m2} , currents' mean-square values I_1 , I_2 and power ratios $\cos \varphi_1$, $\cos \varphi_2$ in the inductor 1 and workpiece 2

As a result of the inductor current's mean-square value decrease during the thermal transient process duration, heat losses in it decreases too, because the inductor's resistance does not change and current decreases. Simultaneously, the heat losses in the workpiece increase as a result of the resistance's increase despite the current's decrease. The active power consumed from the source, i.e. the sum of the power of heat losses in the inductor and workpiece increases in time. The temporal dependencies of the heat losses in the inductor and workpiece, as well as the active power consumed from the source are presented in Fig. 17.

Despite a very high heat conductivity of aluminum, the workpiece's temperature

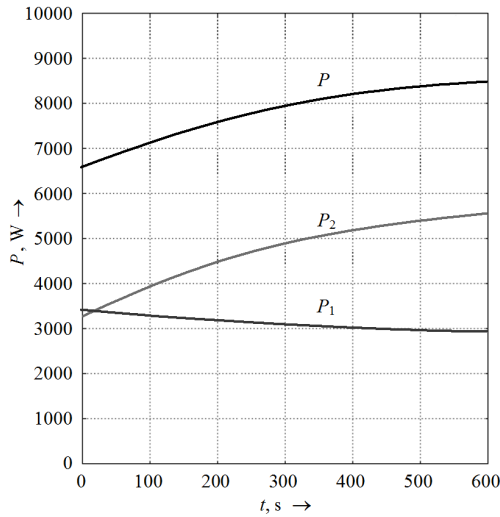


Fig. 17. Temporal dependence of the heat losses in the inductor (P_1), workpiece (P_2) and active power (P) consumed from the source

is distributed non-uniformly in its particular section, and the non-uniformity of the distribution increases in time, i.e., with the temperature's increase. Besides, as a result of different heat transfer conditions on the workpiece's end surfaces, there is the temperature distribution's asymmetry in the workpiece's cross-section along the z -axis. The dependencies presented in Fig. 18 demonstrate quantitatively the above-mentioned non-uniformity and asymmetry of the temperature distribution.

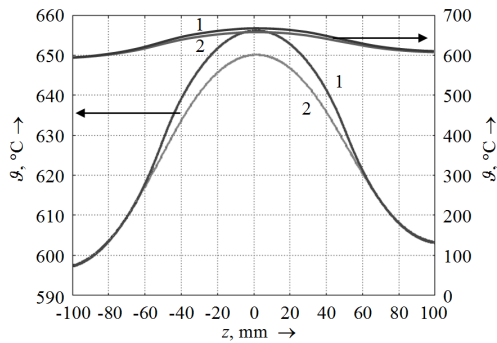


Fig. 18. Non-uniformity and asymmetry of the temperature distribution along the z -axis on the workpiece's external (1) and internal (2) surfaces at $t = 505$ s

From the dependencies presented in Fig. 18 it can be seen that the temperature difference of the maximally heated point (ϑ_{\max} in the center of the workpiece's external surface) and the minimally heated point (ϑ_{\min} on the boundary of the bottom end at the workpiece's internal surface) even at the final stage of the process when the workpiece's temperature approaches to the melting temperature $\vartheta_m = 658^\circ\text{C}$

may be very essential, for example for $t = 505$ s, $\vartheta_m = 658$ °C and $\vartheta_{\min} = 598$ °C (the difference is about 10% regarding ϑ_{\min}). One of reasons of such asymmetry of the temperature distribution is the above-mentioned dependence of the convective heat transfer coefficient on the considered workpiece's surface part and mean temperature difference.

The diagrams of transient processes of the temperature changes in the most heated workpiece's point and in the least heated one are presented in Fig. 19 (solid lines).

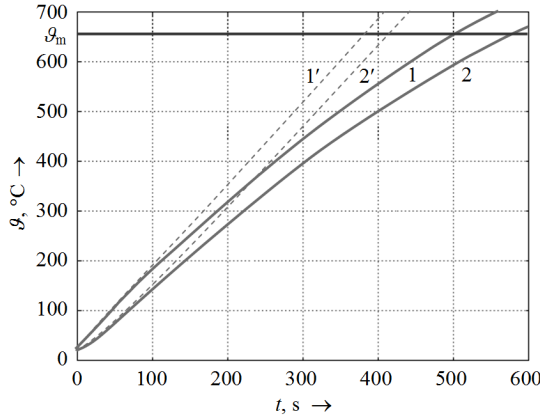


Fig. 19. Transients of the temperature changes at the most heated workpiece's point (1) and at the least heated one (2), as well as calculated temperature values at these points in the adiabatic mode (1' and 2', respectively)

At the initial stage of the transient (0–10 s) the velocity of the temperature increase at the most heated point equals approximately to 2 K/s, and at the least heated point 0.8 K/s. As a result at the same initial temperature ($\vartheta_a = 20$ °C), the curves of these points' heating diverge essentially, for example at $t = 47$ s one can see $\vartheta_{\max} = 100$ °C and $\vartheta_{\min} = 66$ °C (the difference is about 50% regarding ϑ_{\min}). Such a big temperature difference is caused by the concentration of all workpiece's heat power in the narrow band of thickness of about 2 mm near the workpiece's internal surface opposite the inductor (see Figs. 9, 10) at the inductor's thickness of 20 mm. Therefore, some time is required for the thermal front penetration deep into the workpiece.

The technique of the thermal calculation used by authors (heat exchange of the workpiece with ambient air is taken into account by using the boundary conditions of the third kind on the workpiece's surface) permits to calculate easily the adiabatic process of the workpiece heating for which in initial data it is enough to set zero values of the heat transfer coefficients for all surfaces. The diagrams of transient processes of the temperature changes at the most heated workpiece's point and at the least heated one at the adiabatic process are also presented in Fig. 19 (dashed lines). From the presented diagrams it can be seen that at the initial stage of heating the transient is close to the adiabatic process and during the temperature increase the heat transfer to the ambient medium increases too, and the temperature increase

becomes slower. These calculations did not take into account phase transitions, i.e., workpiece's material physical properties change at the melting temperature. Therefore, numerical results taking into account phase transitions after the melting temperature reaches at the most heated point (in this case, after 500 s) should differ from the results presented in Fig. 19, and not only at the most heated point but also at the points with lower temperatures. In general, it is necessary to solve thermal problems taking into account phase transitions but in this work such a problem is not considered.

As results of this problem solution show, at the above-mentioned initial data the workpiece may be fully heated till the melting temperature during the time of about 10 min (~ 600 s). The total thermal insulation of the workpiece, for example, by using spalling-resistant ceramics can decrease the heating time to 7 min (~ 420 s) approximately, and further acceleration of the heating process is only possible by the increase of the power supplied to the inductor.

5. Analysis of obtained results

1. The approach for the forming of boundary conditions imitating infinity of the ambient space around the inductor-workpiece system does not practically influence the results of the electromagnetic processes calculation even if radius of the sphere limiting the field area is not essentially more than the maximal dimension of the system's elements (in our case the limiting sphere's radius equals to twice workpiece's axial dimension). Therefore, at such problems solution it is not necessary to use the Kelvin transform and so it is possible to essentially reduce time necessary for the computations.

2. As appears from graphs presented in Fig. 5 duration of transient is sufficiently large and reaches 20–30 periods of the voltage oscillations. However, in the absolute value it equals to 2–3 ms only, therefore at the calculation of more inertial thermal processes, electromagnetic ones can be considered as quasi-static.

3. As appears from Figs. 7, 9 and 11, because of sharp skin effect as a result of high specific electrical conductivity of aluminum, magnetic field, eddy currents and heat sources concentrate in the thin surface layer of the workpiece. As an example, axial component of the magnetic flux density B_{mz} practically becomes equal to zero already on the distance of 3 mm from the workpiece's external surface (see Fig. 11).

As appears from Figs. 12 and 13, the edge effect becomes apparent in "spikes" of radial and axial components of the magnetic flux density in the vicinity of the inductor's edges ($z = 50$ mm and $z = -50$ mm) as well as (at essentially more less values of the magnetic flux density) in the vicinity of the workpiece's edges ($z = 100$ mm and $z = -100$ mm). Here, eddy current density and heat sources density distributions along the workpiece's length are "smooth" (without "spikes" under the inductor's edges and near the workpiece's edges).

5. Values of the heat (active) power dissipated in the inductor and in the workpiece have a difference less than 1% because of small value of the air gap between the inductor and the workpiece, and as a result of the sharp skin-effect currents in the inductor and in the workpiece concentrate in thin layers opposite one to another

therefore the magnetic coupling coefficient of the inductor and the workpiece is close to 1.

6. Calculated values of the radiant heat transfer coefficient may change in the wide range because in different literature sources there are essentially different values of the emissivity of aluminum. However, a huge spread of the radiant heat transfer coefficient values do not influence essentially on the accuracy of the workpiece's heating temperature calculations because the radiant heat transfer coefficient represents only a little part of the total heat transfer coefficient (a sum of the radiant heat transfer coefficient and the convective heat transfer coefficient). Validity of the calculated values of the convective heat transfer coefficient is sufficiently high because their determination is connected with solution of the Navier-Stokes equations which describe adequately the convective heat transfer.

7. As appears from Fig. 18, despite the very high heat conductivity of aluminum, the workpiece's temperature is distributed non-uniformly by its section, and the non-uniformity of the distribution increases in time, i.e., with the temperature's increase. Besides, as a result of different heat transfer conditions on the workpiece's end surfaces, there is the temperature distribution's asymmetry in the workpiece's cross-section along the z -axis.

8. At the given initial data, the workpiece may be fully heated till the melting temperature of aluminum (658°C) during the duration of about 10 min (~ 600 s). The total thermal insulation of the workpiece for example by using spalling-resistant ceramics can decrease the heating time to 7 min (~ 420 s) approximately, and further acceleration of the heating process is only possible by the increase of the power supplied to the inductor.

9. The calculations carried out did not take into account phase transitions, i.e., sharp workpiece's material physical properties change at the melting temperature reach. In general, it is necessary to solve thermal problems taking into account phase transitions but in this work such a problem is not considered.

6. Conclusion

The authors developed the computer model of strongly coupled (multiphysics) electromagnetic and thermal process during induction heating of cylindrical workpieces. The problem is solved in axisymmetrical formulation using Comsol Multiphysics code. Peculiarities of electromagnetic and thermal transients are investigated during a benchmark problem solution regarding induction heating of aluminum tube. Currently the authors develop a technique for experimental validation of the proposed numerical approach and obtained results.

7. Appendix A - Validation of the electromagnetic calculations correctness by the Comsol Multiphysics code

The Comsol Multiphysics code gives a possibility to calculate line and surface integrals that in its turn permits to carry out validation of the calculations correctness.

In particular, solution of problems connected with electromagnetic calculations may be checked on the correspondence of the obtained results to the Ampere's circuital law:

$$\oint \mathbf{H} \cdot d\mathbf{l} = i_0,$$

where \mathbf{H} is the instantaneous value of the magnetic field strength vector in the arbitrary point of some closed circuit, $d\mathbf{l}$ is the elementary vector of length directed by the tangent line to the closed circuit in the mentioned point, i_0 is the instantaneous value of the total current overlapping with given closed circuit. The current is supposed to be positive if it creates the magnetic field whose direction coincides with direction of the path-tracing selected at the calculation of the curvilinear integral, i.e., at the calculation of the magnetic field strength vector circulation.

Linear quasi-static problems solutions are sinusoidal functions whose amplitudes and phases are calculated at any point of the problem solution area. As such functions we can consider, in particular, sinusoidal functions of the current density vector \mathbf{J} (in our case, this vector is perpendicular to the plane of the drawing, i.e., the plane passing through the symmetry axis) and sinusoidal functions of the magnetic field strength vector \mathbf{H} as well as sinusoidal functions of the axial and radial components H_z and H_r of the vector \mathbf{H} .

Any sinusoidal function $y(t)$ can be represented in the form of a product of the complex value (phasor) \underline{Y} corresponding to this function and the "rotating vector" $e^{j\omega t}$. This rule can be expanded to scalar and also vector quantities. So, the above expression may be represented in the form

$$\oint \underline{\mathbf{H}} \cdot e^{j\omega t} \cdot d\mathbf{l} = \underline{I}_0 \cdot e^{j\omega t}.$$

Hence, the expression for the Ampere circuital law in the complex form is obtained in the form

$$\oint \underline{\mathbf{H}} \cdot d\mathbf{l} = \underline{I}_0.$$

Calculation of the magnetic field strength vector circulation phasor by the circuit limiting some rectangular area S (see Fig. 20) comes to the calculation of four line integrals along sides (ab, bc, cd and da) of the rectangle limiting the indicated area.

$$\oint \underline{\mathbf{H}} \cdot d\mathbf{l} = - \int_{ab} \underline{H}_z \cdot dz + \int_{bc} \underline{H}_r \cdot dr + \int_{cd} \underline{H}_z \cdot dz - \int_{da} \underline{H}_r \cdot dr,$$

where \underline{H}_z , \underline{H}_r are phasors of the axial (on sides ab, cd) and radial (on sides bc, da) components of the magnetic field strength along the rectangular area S . Signs "-" in the first and fourth terms indicate that at the calculation of these integrals the path-tracing (clock-wise) is opposite to the positive direction of r - and z -axes, respectively.

Table A1 presents the calculated phasors of the current \underline{I}_0 in the workpiece and magnetic field strength circulation around the workpiece's cross section for two values of the initial phase ψ —(0° and 90°) of the source's voltage $u = U_m \cdot \sin(\omega t + \psi)$,

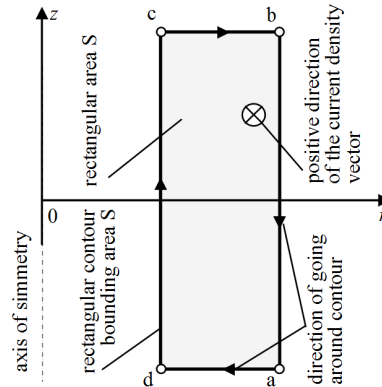


Fig. 20. On the calculation of instantaneous values of the current and line integrals around the rectangular cross section of the workpiece

its frequency being 8 kHz. The results demonstrate sufficiently high accuracy of the calculations: the phasors of the current and the magnetic field strength vector circulation differ by less than 1 % both in real component and imaginary components.

Table A1. Results of calculations of phasors of the current I_0 in the workpiece and the magnetic field strength vector circulation around the workpiece's cross section

ψ		\underline{I}_1	\underline{I}_2	\underline{I}_3	\underline{I}_4	$\oint \underline{H} \cdot d\mathbf{l}$	\underline{I}_0	$\arg(\underline{I}_0)$
0°	Re	-1290.57	0.715	0.440	0.658	-1288.76	-1299.65	$97^\circ 40'$
	Im	9667.54	-20.952	2.646	20.979	9712.12	9712.79	
90°	Re	-9667.54	-20.952	-2.646	-20.979	-9712.12	-9712.79	$187^\circ 32'$
	Im	-1290.57	0.715	0.440	0.658	-1288.76	-1299.65	

8. Appendix B - Temperature dependencies of the resistivity ρ , conductivity σ , specific thermal conductivity λ and specific heat capacity c of copper and aluminum

As the workpieces' temperature is changed in a wide range during the induction heating, it is necessary to take into account the temperature dependencies of main materials' thermophysical properties. In the problem definition the specific grades of copper and aluminum for the inductor and the workpiece are not given, therefore the authors decided to use properties of pure metals. These characteristics in the form of tables and diagrams are presented in various handbooks. Because in the problem definition an algorithm of the completion of the heating process calculation is not fixed, the authors decided to complete the simulation of workpiece's transient heating process on reaching the melting temperature at the least heated point and neglect the stick-slip change of the thermophysical parameters on the phase transition's bound. Besides, it was decided to approximate the table data by the least-squares

method with parabolic functions in the form

$$y(\vartheta) = y_0 \cdot (1 + \alpha\vartheta + \beta\vartheta^2),$$

where $y(\vartheta)$ is the value of the thermophysical parameter y at the temperature ϑ , y_0 is its value at the temperature 0°C and α , β are empirical coefficients.

In particular, empirical expressions for the resistivity ρ and specific heat capacity c of copper and aluminum are the following

$$\rho(\vartheta) = \rho_0 \cdot (1 + \alpha_\rho \cdot \vartheta + \beta_\rho \cdot \vartheta^2),$$

$$c(\vartheta) = c_0 \cdot (1 + \alpha_c \cdot \vartheta + \beta_c \cdot \vartheta^2).$$

The values of parameters in the above two equations are presented in Table B1.

Table B1. Values of empirical coefficients for the calculation of resistivity ρ , and specific heat capacity c of copper and aluminum

Material	ρ_0	α_ρ	β_ρ	c_0	α_c	β_c
Cu	$1.55 \cdot 10^{-8}$	$4.03 \cdot 10^{-3}$	$9.53 \cdot 10^{-7}$	383.3	$2.01 \cdot 10^{-4}$	$8.84 \cdot 10^{-8}$
Al	$2.44 \cdot 10^{-8}$	$4.19 \cdot 10^{-3}$	$1.28 \cdot 10^{-6}$	895.0	$3.92 \cdot 10^{-4}$	$3.13 \cdot 10^{-7}$

At the substitution of values of the temperature ϑ in $^\circ\text{C}$, the result of calculations by these formulae for the resistivity will have the dimensionality $[\Omega \text{ m}]$ and for the specific heat capacity $[\text{J}/(\text{kg}^\circ\text{C})]$.

Because the conductivity σ is the reciprocal quantity to the resistivity ρ , for calculation of the values of σ we did not approximate the corresponding table values by a separate empirical formula, and we used the expression

$$\sigma(\vartheta) = 1/\rho(\vartheta) = 1/(\rho_0 \cdot (1 + \alpha_\rho \cdot \vartheta + \beta_\rho \cdot \vartheta^2)),$$

When using the values of temperature ϑ in $^\circ\text{C}$, the results of calculations will have the dimensionality $[\text{S}/\text{m}]$.

For calculation of the values of λ , we did not approximate the corresponding table values either, but we used the Wiedemann–Franz–Lorenz law in the form

$$\rho(T) \cdot \lambda(T) = L \cdot T,$$

where $T = \vartheta + 273$ is the absolute temperature and $L = 2.47 \cdot 10^{-8}$ is the Lorenz constant. Hence

$$\lambda(\vartheta) = \frac{L \cdot (\vartheta + 273)}{\rho_0 \cdot (1 + \alpha_\rho \cdot \vartheta + \beta_\rho \cdot \vartheta^2)},$$

At the substitution of values of the temperature ϑ in $^\circ\text{C}$, the result of calculations by these formula will have the dimensionality $[\text{W}/(\text{m}^\circ\text{C})]$.

References

- [1] J. D. LAVERS: *State of the art of numerical modeling for induction processes*. COMPEL-International Journal for Computation and Mathematics in Electrical and Electronic Engineering *27* (2008), No. 2, 335–349.
- [2] M. FÉLIACHI, G. DEVELEY: *Magneto-thermal behavior finite element analysis for ferromagnetic materials in induction heating devices*. IEEE Transactions on Magnetics *27* (1991), No. 6, 5235–5237.
- [3] M. G. PANTELYAT, M. FÉLIACHI: *Magneto-thermo-elastic-plastic simulation of inductive heating of metals*. EPJ AP-European Physical Journal Applied Physics *17* (2002), No. 1, 29–33.
- [4] I. DOLEŽEL, J. BARGLIK, C. SAJDAK, M. ŠKOPEK, B. ULRYCH: *Modelling of induction heating and consequent hardening of long prismatic bodies*. COMPEL-International Journal for Computation and Mathematics in Electrical and Electronic Engineering *22* (2003), No. 1, 79–87.
- [5] J. BARGLIK, I. DOLEŽEL, P. KARBAN, B. ULRYCH: *Modeling of continual induction hardening in quasi-coupled formulation*. COMPEL-International Journal for Computation and Mathematics in Electrical and Electronic Engineering *24* (2005), No. 1, 251–259.
- [6] B. RAMDANE, D. TRICHET, M. BELKADI, J. FOULADGAR: *3-D numerical modeling of the thermo-inductive technique using shell elements*. IEEE Transactions on Magnetics *46* (2010), No. 8, 3037–3040.
- [7] K. BLINOV, A. NIKANOROV, B. NACKE, M. KLÖPZIG: *Numerical simulation and investigation of induction through-heaters in dynamic operation mode*. COMPEL-International Journal for Computation and Mathematics in Electrical and Electronic Engineering *30* (2011), No. 5, 1539–1549.
- [8] YILUN LI, SHIYOU YANG: *3D eddy current and temperature field analysis of edge induction heater*. COMPEL-International Journal for Computation and Mathematics in Electrical and Electronic Engineering *35* (2016), No. 2, 683–694.
- [9] M. G. PANTELYAT: *Coupled electromagnetic, thermal and elastic-plastic simulation of multi-impulse inductive heating*. International Journal of Applied Electromagnetics and Mechanics *9* (1998), No. 1, 11–24.
- [10] D. MEEKER: *Improvised open boundary conditions for magnetic finite elements*. IEEE Transactions on Magnetics *49* (2013), No. 10, 5243–5247.
- [11] J. A. STRATTON: *Electromagnetic Theory*. Publisher: John Wiley and Sons, Inc., Hoboken, New Jersey (2007).
- [12] J. P. HOLMAN: *Heat Transfer*. Publisher: McGraw-Hill Series in Mechanical Engineering, New York (2002).

Received June 8, 2018

Design of architectural models to enhance the security of buildings and urban areas against military with passive defense approach

HASSAN SALEHI¹, EHSAN AKBARI²

Abstract. Today, with the advancement of military technologies, for many reasons ethical principles has been degenerating and different countries threaten each other for unsubstantiated reasons and attack one another. One of the most important defensive strategies that is being considered by many developed countries in the world, is using passive defense requirements for increasing the security of buildings and areas in between buildings against explosion and its peripheral effects. The lack of secure sites in open urban spaces and residential environments poses many risks for the buildings and residents in the event of a crisis. By designing these spaces intelligently, not only most of environment and human resource vulnerability can be prevented, but also by creating a beautiful space it can add to the architectural enrichment of the environment. This is an applied research with main purpose being to explain various methods of reducing the destructive effects of explosions and their resulting waves in buildings and landscapes.

Key words. Urban spaces and inter-building spaces, passive defense, architectural and landscape design patterns, secure sites.

1. Introduction

Passive defense consists of a set of non-military actions that increase deterrence ability, reduce vulnerability, sustain the necessary activities, promote national sustainability, and facilitate crisis management against threats, military actions and unexpected events (Jalali Farahani [1]). Today, passive defense is always considered as one of the most effective and lasting methods of defense against threats by most countries in the world and even countries with considerable military power like USA and Russia pay special attention to this issue. It is for this reason that in recent

¹Khatam Ol Anbia University, Tehran, Iran; e-mail: h.salehi@srttu.edu

²Department of Architecture, ACECR Institute of Higher Education, Kermanshah, Iran; e-mail: Ehsan.akbariea69@gmail.com

years and during the Cold War a great deal of design arrangements has been done in this regard, in most countries in the world. Throughout human history, only a few years can be found when a war has not occurred at some spot in the world. As humanity entered an era of prosperity and advancement, not only the trend did not decrease, but also the methods of fighting changed in a way that the death of a large number of people in a fraction of a second became possible (Farzam Shad [2]). War equipment became more advanced day by day and the need for proper defense strategies to counter these weapons is felt more and more. This issue is more important especially in unequal and urban warfare, so as to achieve the best possible defense against the enemy using the least amount of power and equipment.

Passive defense measures can be implemented on a fixed or moving target from conceptual design and study stage until the operation of the target, and these measures include special methods and techniques at various stages of the target's life cycle. Recognizing modern methods and technologies and applying them in the design of secure landscapes and residential complexes in their proper time reduces the cost of secondary measures, and increases the effectiveness of passive measures and preservation and survival of the subject. With intelligent combination of natural elements, the architectural ideas and the principles of passive defense, these injuries can be minimized.

2. Problem statement

Attacking the cities and their strategic spaces (such as public urban areas) is always one of the most important goals of the invading countries and the reason for it is that a blow to these centers has vast destructive effects on military, defensive and psychological functions and that is of key importance in the invader's victory. So much that even the international regulations do not prevent the invading country from attacking such centers and waiving the benefits of its psychological superiority. Therefore, attention to reducing the vulnerability of such sites is important in increasing the defense capability of each city and country. Such an important issue requires finding solutions and preventive measures for decreasing damages to these centers, preserving forces and personnel as human capital (Farzam Shad [2])

Today, due to vast advances in science and technology, by designing long range missiles it is possible to accurately target and take down the targets identified by satellite imagery from very long distances. Now the question that comes to mind is: what can be done to counter the destructive effects of an enemy's air-to-surface and surface-to-surface missiles?

Without doubt the least costly and most effective way is using camouflage patterns and techniques that reduces the destructive power of the explosion wave and creates a good potential to hide and shelter human resources. Now, the main issue of this research is investigating the type, quality and sustainable design methods for public urban spaces and landscapes between the buildings; so that while creating a barrier in front of the destructive power of explosion waves, a good potential for temporary hiding of the human resources in the complex is also provided.

3. Objectives

Today, with the advancement of military technologies, for many reasons ethical principles has been degenerating and different countries threaten each other for unsubstantiated reasons and subject each other to military attacks (Shayesteh Afshar [3]). In this time, USA, as the top military power and a world super power goes unchallenged and in this way has caused irreparable damage to several countries and occupied them.

Considering its Islamic nature and existing in one of the strategic spots of the world (the Middle East), the Islamic Republic of Iran has always been exposed to various threats by different countries; Therefore it is necessary that it secure itself against any sort of military threats from enemies using the most complete defensive measures. In this regard it can be said that in terms of active defense and military equipment and weapons, most countries in the world are in same situation and level and what determines the result of a war would be war strategies and passive defense associated with nullifying the attacks and surprising the enemy. With the aforementioned points in mind the main objective of this research is exploring and analyzing effective architectural and structural components in defining a pattern for planning and design of residential neighborhoods and public spaces in urban area in order to counter the effects of a terrorist military invasion (from land and air) to the cities. Other secondary objectives of this research include:

- Increasing survival capability, sustaining vital activities and providing services to vital public urban spaces and community centers,
- Maintaining the spirit, solidarity and unity, strategic proposals to reinforce deterring factor and raising people's resistance threshold,
- Increasing the probability of durable structure activity, the continuity of vital activities and the improvement in the level of resilience of buildings and the perimeter spaces during the enemy attack, using proper design methods,
- Reducing the vulnerability and minimizing the damage to equipment and human resources as well as sensitive and strategic points of the complex,
- Saving expenses and time, to camouflage complexes and strategic and sensitive spots in time of danger,
- Attempting to divest the enemy and terrorists from the freedom and initiative by deceiving them through design,
- Decreasing the destructive power of the explosion wave (in a very small amount) and approximate control of its resulting tension, reducing casualties by designing curved guiding shapes and removing corners from landscapes and building facades.

4. Scientific or technical basis and the method of implementing the plan

This is a descriptive-analytic research whose data is collected using theoretical methods and field study. In this regard, by reviewing library resources and approved regulations such as: FEMA Regulations, Architectural and Landscape Design regulations of the USA Department of Defense, and the CD of Landscape Design of

Passive Defense of the Islamic Republic of Iran, practical and at the same time low cost parameters were identified in order to enhance the security of urban public spaces and inter-building landscapes and was then introduced to architects and designers as designable ideas.

5. Comparison of the efficiency of deception and retrofit designs on the safety of semi-buried structures

In this research, the probability of continuity of activity as the main criterion of the efficiency and the efficiency of the scheme of "deception and disturbance" and the "retrofitting" scheme for a buried structure are counted in depth and compared with each other.

In this research, in order to observe the worst computational conditions, the effect of prevention programs on the identification of buried structures is ignored and the visibility of the structure is considered to be 100%. In this case, two strategies to secure buried structures can be imagined:

Create deception schemes to increase the CEP error of ammunition;

Reinforcing the concrete walls of the structure by adopting a strategy of increasing the thickness of the wall to reduce the permeability of the structural line.

To compare the efficacy of immunization techniques, a simple scenario is used where a buried structure at a low depth of 300 square meters is powered by the GBU-28 Enhanced Paveway III DMLGB bombs combining two types of laser sensors and the satellite is being invaded. For this purpose, the probability of continuity of the structure after the implementation of 10 air strikes was calculated for different levels of rigging and levels of deception. For this purpose, five levels of retrofitting for wall thickness from 30 cm to 1/1 m were considered. Also, five levels of deception for ammo misses were compared from 10 meters to 90 meters. Thus, 25 different statuses were obtained as shown in the table below.

Table 1. Comparison of deception and retrofit schemes (Hosseini, 2013)

	PoC	Wall thickness (m)				
		0.3	0.5	0.7	0.9	1.1
Enemy ammo error (m)	10	0%	0%	0%	0%	0%
	30	23 %	32 %	37 %	40 %	42 %
	50	59 %	66 %	70 %	72 %	73 %
	70	76 %	81 %	83 %	84 %	85 %
	90	85 %	88 %	89 %	90 %	91 %

Note: PoC - Probability of continuity (in %) of the sample structure after 10 attacks with intruding ammunition

- There is no need for retrofitting for an error value of more than 90 meters (while for a wall thickness of 1 meter, if the enemy's mistreatment error is 10 meters,

the probability of continuity of the structure is zero percent and the structure is completely destroyed.

- The rate of change in efficiency versus the ammunition error is much higher than its rate of change compared to the structural upgrading.

- For a constant error value, the yield variations with a wall thickness increase of up to 28 %, while for a constant thickness, the yield variations are maximally 55 %, about twice as high.

Now that it has been assured that the likelihood of structural survival in deception patterns is more efficient than retrofit patterns, we will examine the possibility of monitoring the targets by imaging satellites in a mathematical model in three different situations. There are three basic ways to calculate the coverage of the circuit:

1. Assuming flatness of the ground;
2. Supposing the globularity of the ground;
3. Assuming an ellipticity using a triangle other than the right side for applications that require high precision. Solving the right triangle can be sufficient (the following):

$$SW_m = \arctan S_p h . \tag{1}$$

For most applications, a spherical earth model is desirable. A solution to calculate the ground cover is to depict the satellite's line perpendicular to the surface of the earth, and then the angle (α) between the line drawn from the point of intersection of the radius of the earth and the satellite's line with the center of the earth, and the line between the center of Earth and Satellite (Fig. 1). The distance in the direction of this arc on Earth can be calculated from the following equation:

$$SW_m = \frac{\alpha}{2\pi} R_e . \tag{2}$$

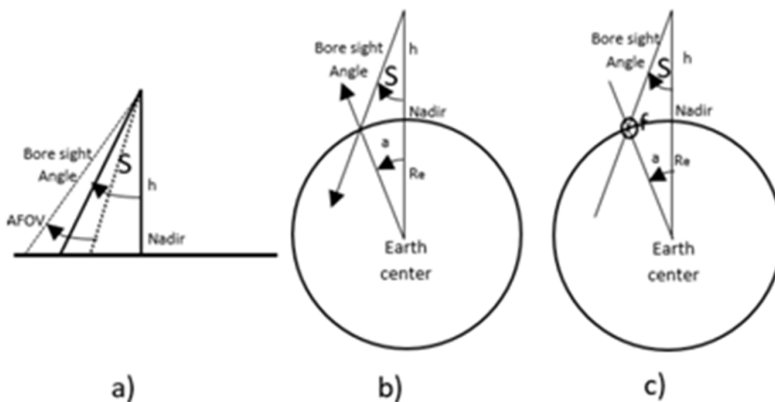


Fig. 1. Determining the satellite image coverage for three modes, flat Earth and spherical Earth (Feizi & Khazaei, 2017)

Another mathematical solution is to find the inclining angle f of an open or steep

triangle and then the peripheral angle. Satellite elevation h , Earth's radius R_e , and angle outside Nader S are problem information. The answer to find F is based on sinus law, which is as follows:

$$\sin(f) = \sin(s)(R_e + h)/R_e. \quad (3)$$

The algebraic expression can be arranged as follows to obtain the inclining angle f . The three angles α , φ , and s should be 180 degrees in total. Since $f = 180 - \alpha - s$, we get

$$\sin(\alpha + s) = \sin(s)(R_e + h)/R_e. \quad (4)$$

Finally, the following equation is obtained:

$$\alpha = \sin^{-1}\{\sin(s)(R_e + h)/R_e\} - s. \quad (5)$$

When the bandwidth of the circuit is calculated, the left and right positions on the azimuth maps at angles perpendicular to the satellite's path are as follows:

$$X_{\text{right}} = \cos(\text{heading} - 180) \cdot (-SW), \quad (6)$$

$$Y_{\text{right}} = -\sin(\text{heading} - 180) \cdot (-SW), \quad (7)$$

$$X_{\text{left}} = \cos(\text{heading} - 180) \cdot (SW), \quad (8)$$

$$Y_{\text{left}} = -\sin(\text{heading} - 180) \cdot (SW). \quad (9)$$

6. Landscape design requirements from passive defense viewpoint

Paying attention to principled design of open spaces by residential complex designers and urban planning rules regulators on the basis of defensive ideas, will increase the safety factor of these spaces and, consequently, reduce damages and injuries. With intelligent combination of natural elements, architectural components and passive design principles these damages can be minimized. Of course in many sites and urban spaces securing every open space is not possible. Therefore, it is only possible to secure limited spaces so that users can feel calmer and safer in times of recreation and rest.

The experience of Iraq's imposed war against Iran, the Six-Day War between the Arabs and the Zionist regime and many of the wars in the world shows that the enemy has started a sudden attack on the country using the element of surprise. This causes the people that were in open area to be exposed to serious injuries. These injuries often are due to the following factors:

- Direct impact of shrapnel caused by the explosion,
- Explosion wave,

- Flying pieces of destroyed objects,
- Collapsing debris,
- Explosion of cars and fuel tanks in the area.

Therefore, with intelligent design of the landscapes, vulnerability of the urban environment in times of crisis and enemy attack can be reduced to a large extent.

6.1. Enclosing the space

Enclosing the space is one of the most effective way to create secure spaces that can be achieved using various methods. Some of these methods include enclosure using walls, floor level difference and a row of tress. Of course it should be considered that the proportions in these spaces should never create an unpleasant, monotonous, cold and soulless and prison like environment for the users.

6.2. Creating safe corners

Creating safe corners can be planned and designed in different ways and some of the main methods include:

6.2.1. Creating level difference using ground slope. Ground slope is another possibility that the environment provides for us to create safe corners. Spaces that are on a lower level can be protected from threats on higher levels by setting some arrangements such as building walls, planting trees or creating a cavity in the slope's walls, and creating that make people feel calm and secure.

If the exterior space is leveled higher than the interior there is no need for a tall wall and short walls or a flower box can provide the security for the enclosure. It is necessary that the minimum distance of this level difference from the building be equal to the height of the building to reduce the risk of falling debris (Figs. 2 and 3).

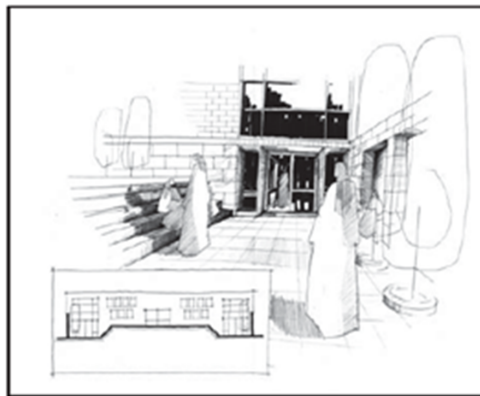


Fig. 2. Enclosing the space using ground slope (Farzm Shad [2])

6.2.2. Buildings around the enclosure. While designing a building, the general form can be designed to create safe spaces and corner in various parts. Also, creating

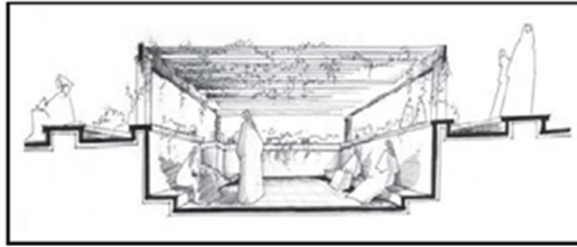


Fig. 3. Enclosing the space using level difference (Farzm Shad [2])

a pilot space under the building can create a warm space and prevent debris from falling on the pedestrians as well as providing a proper roof against sun in the summer and precipitation (Fig.4). In addition, it causes the wave of explosion to pass from beneath and between the buildings and reduces its friction with the building's engaging surface.

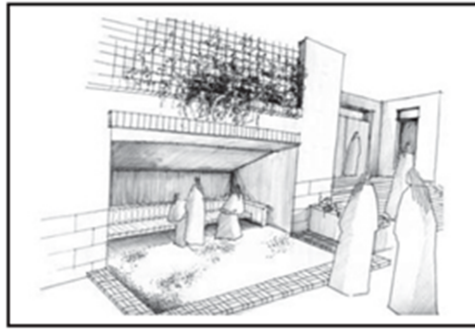


Fig. 4. Creation of safe corners into the building (Farzm Shad [2])

6.3. Form of the buildings

Leaning towards horizontal and staggered shapes can have a considerable effect in preventing debris to collapse into the open space. Also, using filleted corners and curved shapes in the buildings can also play an important role in diverting and depreciating the wave of the explosion.

6.4. Removing appending and ornamental elements from the building

Appending elements to the buildings such as terraces and balconies, shades etc. are one of the most important factors in increasing the damages. Because on one hand these components are separated from the building due to the resulting vacuum and suction from the explosion and will collapse in the yards; and on the other hand anything in them like flower pot, cooler etc. will be thrown around and into the yard and if they hit people or personnel they can cause serious and deadly injuries

to them.

6.5. Using blast pockets and bends.

In order to prevent the wave of the explosion to enter from one space to another in structures and reduce its effects, corridors and circulation paths can usually be created intricately and at different angles so that in an event of an explosion, less waves can reach other sections through tunnels. It is obvious that in straight tunnels, wave reduction happens slowly; therefore in order to prevent the entrance of explosion waves and reducing their effects on the safe spaces, we can use tunnels with deviating routes and different angles. In Fig. 5, a set of bends at various angles is presented. Symbol K_p is a factor that is multiplied by the amount of pressure in lieu of using each bend in the measured path compared to a straight tunnel. For example, a 90-degree bend reduces the peak pressure by about 30 %, and a T-shaped split does this by about 50 %.

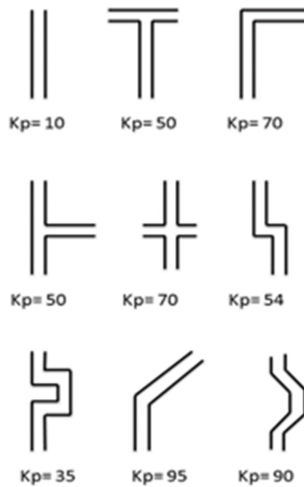


Fig. 5. Comparison between some of wave pressure reductive bends

In addition to bends, at the end of the corridors some blast pockets can be designated to depreciate the resulting waves from an explosion so that less waves can reach other corridors around (Us Army fundamentals of protective design [4]).

6.6. Using trees, elements and proper furniture.

Trees are one of the other components that can play an effective role in creating a safe space. In addition to creation of a pleasant and refreshing environment, they can be a very effective factor against shrapnel from explosion, pressure reduction and deviation of the explosion wave. Thick vegetation is also great for hiding and exiting field of view in aerial attacks. For this purpose, it is recommended to use evergreen trees such as pine and cedar trees and shrubs like Box-tree (see Fig. 6).

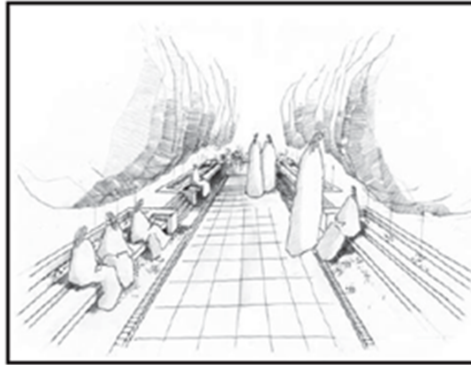


Fig. 6. Proper use of trees and vegetation (Farzm Shad [2])

6.7. Attenuating coatings

The destructive power of an explosion depends on the energy of its waves and to decrease their power, the waves should be weakened in some way or in other words their energy should be depreciated. Positioning the coatings against the waves can cause them to die out faster. These lightweight coatings have an important influence on distribution of the explosion waves and protect the physical integrity of the walls and other elements during the explosion. Available types of coating include:

6.7.1. Protective coatings with liquid mediator. The basis of protection in these protective coatings is their capacity to hold a necessary amount of water. Their main characteristics are their ability to discharge the water at the required time and its easy transfer.

6.7.2. Protective coatings with solid-gas mediator. These coatings are a type of protection that resist the resulting waves from powerful explosions and consist of oval metal beads in a mesh. A large amount of these beads that also contain a gas phase due to the cavity between them are poured in net covers. These covers are then installed on the structure for protection. The top layer must be porous so that the waves can pass through it. If this layer is hard the protection acts as a solid panel and will be destroyed. The high plasticity of this structure considerably depletes the energy of the explosion wave.

6.7.3. Protective coatings with liquid-gas mediator. The efficiency of the explosion waves absorbers increases by replacing the liquid with a liquid-gas mediator and this two-phase mediator reduces the energy of the explosion several folds due to its compressible quality. Linear or non-linear speed reduction by several times in the two-phase mediator affects the explosion wave profile. The three introduced types of coatings have some specific qualities (Keenan, 2002):

- Coatings with liquid mediator: Due to the ability of charging and discharging of a liquid and easy transportation, its usage is recommended in the areas with a

possibility of explosion.

- Coatings with solid-gas mediator: Due to its high plasticity, this structure can considerably depreciate the explosion wave.
- Compounds with liquid-gas mediator: Due to the gas phase of this coating it can reduce the speed and lengthen the time it takes for the explosion wave to pass on.

6.8. Refuge and protective walls

In open spaces, having large and smooth area is not acceptable. Therefore using simple components on surfaces can enrich the space for intended activities in normal circumstances as a well as creating immediate refuge.

- The location of the refuges should be placed outside range of rubble.
- Low capacity refuges with high distribution are better than high capacity but concentrated ones.
- Since the best body position against explosion forces is the prone position, refuges should be designed according to this position in the open space complexes (FEMA 430). Best surfaces that provide refuge in prone for a person are ornamental walls, flower boxes, benches and kennels (Fig. 7). Maximum distance radius to a refuge in open space, considering average running speed (about 3 meters per second) is suggested to be 30 meters to be reached in 10 seconds.



Fig. 7. Using flower box as a refuge (FEMA 430)

- Length of the parapet edge or any other hard barrier should be as short as possible with bends along the way in proper distances to help speed up the depletion of the explosion waves.

Wall is one of the most important elements that can provide security in open spaces; provided that materials texture and shape of the walls be taken into consideration. Vast flat surfaces in yards and gathering places are not acceptable from a security stand point. By building ornamental walls in various shapes (parallel, intersecting, etc.) we can create safe corners as well as nice and diverse spaces (Figs. 8, 9). It should be noted that any edge in an emergency is a refuge.

Also creating bends in walls not only adds to the walls resistance against lateral forces but also prevents the wall from becoming monotonous and creates small spaces and corner along the wall that will be useful as a refuge (Fig. 10).



Fig. 8. Using wall as a refuge (Naghsh Novin CD)



Fig. 9. Using ornamental walls as refuge (Naghsh Novin CD)

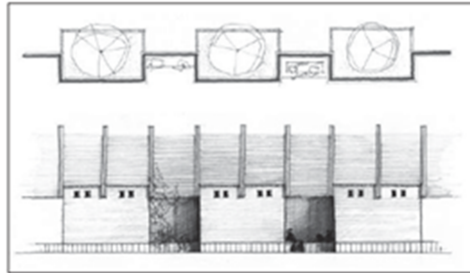


Fig. 10. Creating bends and breaks in the walls as refuge (Farzam Shad [2])

6.9. Using plasma vapor

The first time it was Russia that accidentally discovered the ability of ionized materials in changing the nature of waves. After they sent a satellite into orbit and lost the contact with in after a few days, they started searching for the possible reasons and found out that a layer of ionized oxygen exists above Earth's atmosphere and when radar waves hit this layer their nature changes and are no longer readable by the receivers on earth. They used this method in designing radar evading air crafts and getting out of missiles range (Hashemi Fesharaki, 2008). Nowadays, since the missiles are guided to the target with radar waves, special generators can be used to create ionized materials and use them with tubes on the ground level to misguide the missiles.

6.10. *Polystyrene materials*

Polystyrenes are materials that are achieved through polymeric processes. Polystyrene foams are very light and white in color and are made from polystyrene beads. According to the studies expanded polystyrenes has been shown to have an acceptable performance in reducing tensions caused by shock waves. Making use of inhibitors such as cavities, blocks etc. can reduce the maximum tension as well as delaying the arrival of a shock wave (Journal of Engineering Regulatory Organization, No, 524, 2009).

6.11. *Landscape flooring*

Anything that limits speedy escape from danger should be omitted from the landscape. The floor of open public gathering spaces should be made from soft materials. Hard, uneven surfaces like decorative and stone floors are not recommended because they may cause additional injuries. At the same time, surfaces that limit freedom of movement like soft, dry sand or sticky and muddy surfaces are recommended only in the small scale. The floor of play areas should be made from soft materials if possible. Movement paths should be made without uneven patches or unnecessary steps, especially single steps because these pose a tripping risk in the time of crisis. Ramps are recommended in such instances as they suit the situation better than steps. The slope of the ramp should be 5 percent at most and the diameter should be at least 1.8 meters for the speedy passage of two people side by side (Fig. 11).

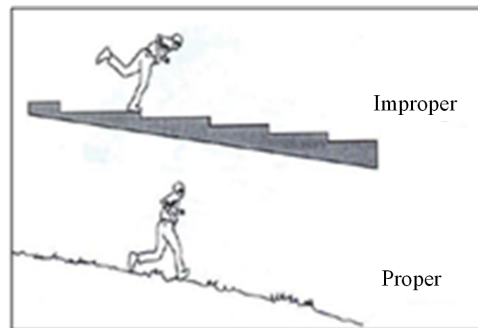


Fig. 11. Using ramps instead of stairs (National Building Regulations: Topic 21)

Green areas should be covered by grass when possible. Any kind of small stone structures (with little resistance against blast forces) is not recommended in these areas for decorative purposes. But big stone structures without sharp corners that can serve as decoration as well as a resistant shelter are a good choice (Fig. 12)

Benches are another part of open area furniture that with the right design can also be used for shelter in addition to their main purpose (FEMA 430), see Figs. 13 and 14.



Fig. 12. Using ornamental elements as refuge (FEMA 430, 4–28)



Fig. 13. Using bench as refuge (FEMA 426, 2-48)

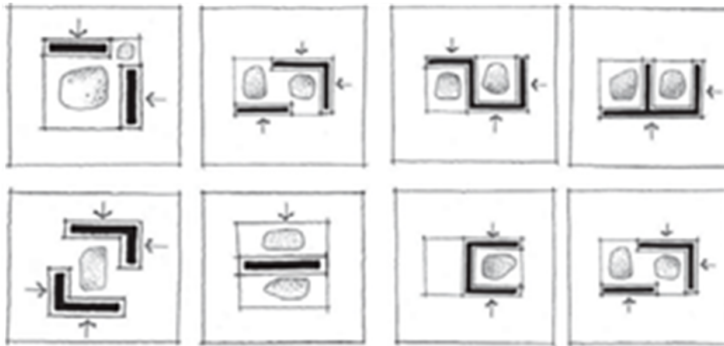


Fig. 14. Arrangement patterns for landscape benches and usage as refuge (Farzam Shad [2])

6.12. Windows and facades adjacent to the landscape

Using glass facades and large windows adjacent to yards without carrying out the necessary precautions can be an effective factor in increasing damages and casualties in the area due to pieces of glass getting thrown around. In case of using these components, firstly the glass parts should be as small as possible and be restrained in a frame, and secondly type of the glass that is used should be armed. Recessed windows can also be effectively helpful in reducing damages.

6.13. *Proper distance between building blocks and the landscape*

To prevent collapsing debris from destroyed buildings into the site and the people in it, proper distance between them must be observed. Also, appropriate distance between building blocks plays an important role in keeping the passages between them safe and the open space can be used for temporary accommodation and relief and rescue operations (Fig. 15).

Cars and fuel tanks are risk factors that in case of explosion can cause a lot of damage to the surrounding area. Therefore it is important that a safe distance between parking and the site be observed so that if a fire broke, it would not reach the buildings and also for a suitable place to be provided for reservoirs with protective measures and if possible lower than ground level or buried.

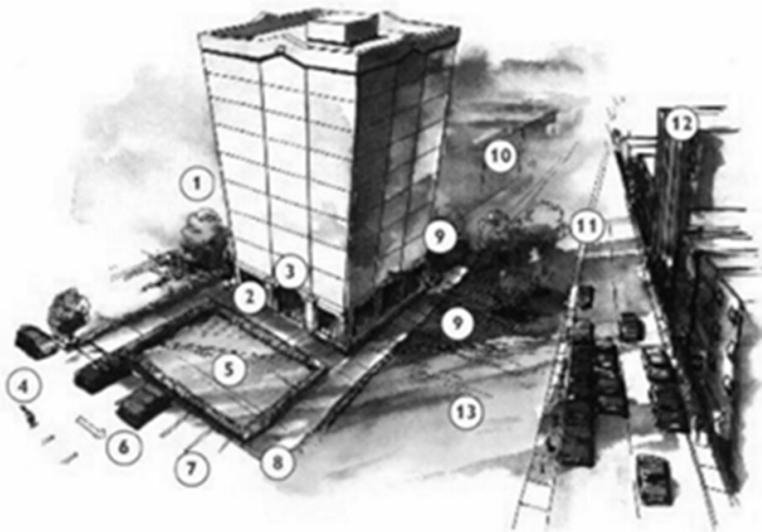


Fig. 15. A graphic design of the general set of measures to enhance the safety of the site and residents of the building (FEMA 426): 1-Locate assets stored on site, but outside the building within view of occupied rooms in the facility, 2-Eliminate parking beneath building, 3-Minimize exterior signage or other indications of asset locations, 4-Locate trash receptacles as far from the building as possible, 5-Eliminate the lines of approach perpendicular to the building, 6-Locate parking to obtain stand-off distance from the building, 7-Illuminate building exteriors or sites where exposed assets are located, 8-Minimize vehicle access points, 9-Eliminate potential hiding places near the building; provide an unobstructed view around building, 10-Site building within view of occupied buildings on the site, 11-Maximize distance from the building to the site boundary, 12-Locate building away from natural or man-made vantage points, 13-Secure access to power/heat plants, gas mains, water supplies and electrical service

6.14. Kennels

Kennels, if designed with proper dimensions, are a good place to take refuge. The minimum depth of the kennel should be 5 cm more than the average body thickness of a male human and therefore about 40 cm. The material of the kennels should also be strong and resistant against explosion forces.

6.15. Using dampers

In strengthening the structures, one of the methods of reducing the lateral forces resulting from explosions is to use dampers. During the explosion a great amount of energy is applied to the structure. This energy is applied to the structure as both kinetic and potential energy that is either absorbed or depreciated. If the structure does not have dampening qualities the vibrations will be continuous but due to the dampening effect of the materials, the vibrations will be reduced.

Dampers, depending on their function, are categorized into some types such as frictional, metal (yielding), viscous, viscoelastic, shape-memory alloys (SMA) and mass dampers (Journal of Engineering Regulatory Organization, No.524, 2009). Therefore, depending on the amount of impact analyzed software such as Autodyne in a modeled space, dampers with appropriate hardness and correct arrangement (serial, parallel, and serial-parallel) can be used to absorb maximum amount of energy in the initial cycles (see Fig. 15).

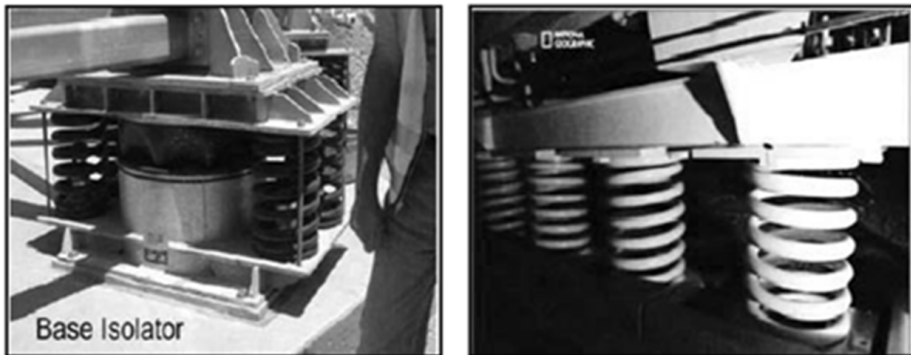


Fig. 16. A view of the damper springs at NORAD control and command center (Alhamad, 1996)

6.16. Using dampers

Damage to grids such as electricity or gas can exacerbate the losses; because gas leakage in space, can create large fires. It is necessary that proper security measures like burial of gas pipes at proper depth, automatic cut-off valves and other regulations be foreseen and for aerial passage of electricity cables be prevented.

7. Conclusion

In this paper, various methods of improving the security of urban public spaces and inter-building landscapes were investigated. In this regard, firstly, possible threats and damage, such as the explosion wave and its destructive effects, were identified on the basis of previous experiences, and solutions for creating a sanctuary, reducing the demolition power of waves, and the manner in which design of the site and placement of space, flooring and walls of the landscapes should be done were suggested. Results clearly showed that it is possible to create beautiful and pleasant spaces without affecting their functions using architectural measures as well as reducing the severity and extent of the enemy's attacks in times of crisis; without it requiring exorbitant costs.

References

- [1] B. ARASH, E. SHAHLA: *An analytical approach to the issue of passive defense in relation with preservation of urban elements*. Current World Environment 9 (2014), No. 2.
- [2] A. REZAEI, J. NAKHAEI: *Analysing criteria to locate medical centers in approach to passive defense (Case study: Treata hospital in 22nd district of Tehran municipality)*. Electronic Journal of Biology 13 (2017), No. 3, 234–242.
- [3] S. A. ELHAM: *Determining the optimal city form based on passive defense principles*. First Conference for Passive Defense and Resistant Structures, Nushirvani University of Technology, Babol, Iran, 2010.
- [4] *US Army fundamentals of protective design (non-nuclear)*. Dept. of army Technical manual TM5-855, Washington, USA, 1965.
- [5] M. KEENAN: *Water-based apparatus to mitigate damage and injuries from a fully or partially confined explosion*. Patent No. 6, 397, 753 b2, www.uspto.gov., 2002.
- [6] *FEMA-453 (2006) and FEMA-430 (2007): Site and urban design for security*.
- [7] H. FESHARAKI, S. JAVAD: *Understanding passive defense*. PhD thesis, Malek Ashtar University, Tehran, Iran, 2008.
- [8] Iran's Engineering Regulatory organization No. 524: *A guide to seismic improvement methods of existing buildings and construction details*. Deputy Directorate for Strategic Planning and Supervision of Presidential Foundation, Tehran publication, Tehran, Iran, 2009.
- [9] S. ALHAMAD: *Anti-explosion pads with steel mesh, slitted metal foil and expanded metal net*. Patent No. 5, 576, 511 b2, www.uspto.gov., 1996.

Received October 12, 2017

Temperature influence of load current of overhead electrical distribution networks in difficult weather conditions

OLEKSANDR KOZLOVSKIY¹, DMITRO TRUSHAKOV²,
SERHIY RENDZINYAK³

Abstract. In order to increase the efficiency of overhead power lines operation in distribution electrical networks under conditions of ice formation, the effect of load currents on the wires temperature of overhead lines is estimated. As a result of the analysis of daily electric loads schedule for typical agricultural consumers, it was established that during the period of the most probable formation of glaze and rime deposits their load is in the range from 11 % to 35 % relative to the daily maximum. Theoretical study of the temperature change law for the wire showed that the load currents of overhead power lines up to 25 % of the nominal value increase the wire temperature to from 0.3 °C to 2.2 °C, depending on the wind speed. When creating technical devices for implementing information systems for monitoring overhead lines in icing conditions, it is advisable to use indirect approach to control, since the wire branching to 10/0.4 kV substations of the distribution net-work temperature is similar with the ambient temperature, due to their low loading.

Key words. Overhead power lines, graph electrical load, temperature wire.

1. Introduction

On the territory of Ukraine over the past decade, the largest number of climatic records was captured in the history of regular meteorological observations. It goes to show that irreversible climate changes have occurred, which are manifested in the growth of the frequency of extreme weather conditions, in particular, in the cold season. The wind-icing phenomena are causing significant damage to the economy

¹Department of Electrical Systems and Energy Management, Central Ukrainian National Technical University, CNTU Kropivnitskiy, Ukraine; e-mail: kozlovskiyoa@gmail.com

²Department of Automation and Control in Technical Systems, Central Ukrainian National Technical University, CNTU Kropivnitskiy, Ukraine; e-mail: dmitro.trushakov@gmail.com

³Institute of Power Engineering and Control Systems, Lviv Polytechnic National University, Lviv, Ukraine; e-mail: emd@polynet.lviv.ua

and population. Unfortunately, forecasts of climatologists are disappointing; such trends will continue in the future [1]. Therefore, urgent adaptation to the climate changes of the basic area of the economy of Ukraine – power engineering.

An analysis of experience in the exploitation of power equipment shows that the most sensitive part of the energy system to atmospheric loads are the overhead power lines, and the maximum of technological disruptions in their work are accounted for electrical distribution networks 6/10 kV. Damages of overhead lines resulting from the action of excessive mechanical loads from the influence of ice-and-wind phenomena constitute only up to 20 % of all damages for overhead power lines, but they occur on the territory of several regions and are massive by its nature. For example, icing in 2000 led to the blackout of 3861 settlements in 11 regions of Ukraine as a result of damage to 15 800 overhead power lines. Only in the Vinnytsia region 95 % and in Odessa region—90 % of towers of electrical distribution networks were destroyed. The total losses from these damages amounted to 512 million UAH [2].

2. Statement of the problem

Today, the increase in the efficiency of the exploitation of overhead power lines in the icing conditions is achieved by the use of automated ice melting systems. Those systems are created on the basis of complex information systems of overhead power lines monitoring in icing conditions. The structure of a typical complex system includes the following local systems: monitoring the state of the overhead power line, early confirmation of the formation of glaze and rime deposits, determining the integral parameters of glaze and rime deposits (density, sediment type), ice load control, data communication system. With the technical implementation of these systems, two approaches are possible to control of the wire parameters: the direct and indirect ones [3].

A direct approach involves placing the measuring sensors directly on the wire of an overhead power transmission line and transmitting the information that received by a high-frequency radio channel. In the case of an indirect approach, the sensors are placed on a wire analog unit, which is created on the basis of the wire section of the monitored line and has a zero potential in relation to the ground [4]. Despite its significant advantage—its accuracy, the local systems built using the direct method have significant disadvantages: high cost and complexity of maintenance. The system is built by an indirect approach with low cost and easy maintenance, but their accuracy is depends on the current load of the line. At the same time, the economic crisis and the reform of the agrarian sector were led to a decrease in the output of agricultural products, and as a result, the overhead power lines of the distribution networks of 6–10 kV were under loaded to their designed values. Therefore, in order to choose a rational approach for the construction of local control systems for overhead lines in the icing conditions, it is necessary to estimate the level of the effect of the electric load of the overhead power line on the temperature of its wire.

Thus, the study of thermal modes of overhead electrical distribution networks with glaze and rime deposits before the process is urgent.

3. Research goal and results

Power distribution network of 10 kV in Ukraine is mostly created by the principle of building backbone networks. In this case, the intersection guidance routes chosen taking into account the requirements of mechanical strength, providing normalized voltage drops, the possibility of reserving of nearby highways and also taken into account the prospects of 5% annual growth of electrical loads. As a result, the network provided the necessary reliability of power supply, but the intersection of highways wire was detected 1.5–3 times higher than branching to transformer substations 10/0.4 kV.

Figure 1 represents the sample of a typical distribution network scheme section 10 kV, which consists of 6 backbone networks L121–L126 and is located in 4-th territorial region by icing characteristic parameters [5]. Overhead power lines are designed with using the wires of AC and A types [6], which are positioned on ferroconcrete supports. For realization of backbone networks, the linear disconnectors of DS-185, DS-63 and DS-202 types were installed. Customers is powered by substations consisting of power transformers with power capacity ranging from 40 to 400 kVA.

In the shown scheme, the branching load does not exceed 10% from permitted current, and backbone networks is loaded to its 15% nominal in the scheduled conditions, and to 25% in accidental conditions.

The loads of agricultural electric power customers, as for industrial, is determined by production and the number of working shifts. The daily schedules of its power consuming for working winter day for typical agricultural customers: repair mechanical workshop, etc. are characterized by two strictly expressed daily maximums and single working shift (see Fig. 2).

In Ukraine rime often forms at night, and glaze in the morning, but the same number of cases recorded glaze and rime accretion in daytime, between 12 and 15 hours of day.

Thus, during the days of the formation of glaze and rime deposits the overhead power lines of distributive networks 6–10 kV are loaded within 11 to 35% compared to daytime maximums. Also it should be noted that the years of economic crisis led to a significant reduction in the livestock number, resulting that cattle farm work in partially loaded conditions.

Thus, it is advisable to research the influence current load on wires temperature in distribution networks when they are loaded to 30% from their scheduled current.

To determine the temperature of wire t_{wr} , we used the temperature change law founded in the work [7] for wire section in time flow

$$t_{wr} = t_a + t_w = t_a + \frac{P_j - P_{fr} + m_w c_w S_{p.a} (t_a + t_{dr})}{h_c S + m_w c_w S_{p.a}} \left(1 - e^{-\frac{\tau}{T_0}}\right), \quad (1)$$

where P_j is the power, P_{fr} denotes the internal sources of heating and cooling, $+m_w$ denotes the mass of water falling per unit of area of the wire per unit time, c_w stands for the specific heat of water, S represents the surface area of the wire section, $S_{p.a}$ is the projection area of the wire section, t_w denotes the temperature

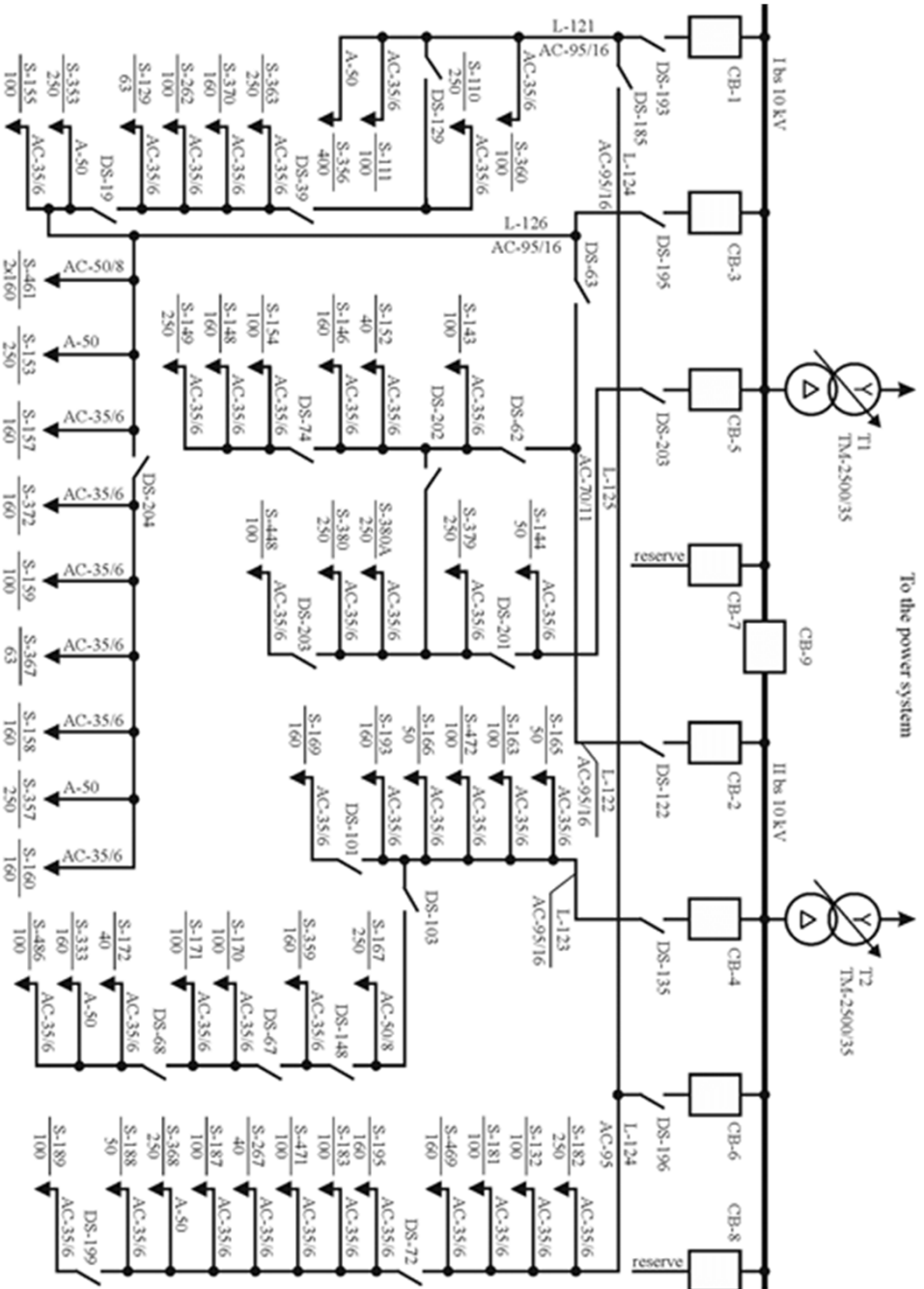


Fig. 1. Example of distribution system 10kV (number of substation is in numerator, rated power of transformer in kVA is in denominator)

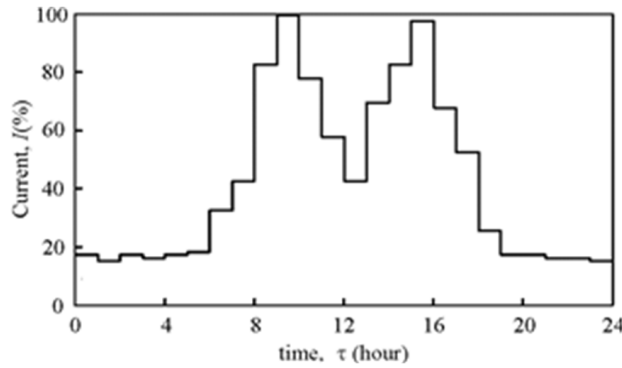


Fig. 2. Daily schedule of power consumption on winter weekdays of the common agricultural consumers

of the wire section, t_a stands for the temperature of ambient air, t_{dr} represents the temperatures of rain drops, τ is the current time, h_c is the heat transfer coefficient [8] and T_0 stands for the wire heating time constant that is given by the expression

$$T_0 = \frac{mc}{h_c S + m_w c_w S_{p.a}},$$

where m is the wire section weight and c denotes the the heat capacity of the wire.

For normal exploitation conditions (dry wire, $m_w = 0$, there is no internal source of cold— $P_{ir} = 0$), eq. (1) takes the form

$$t_{wr} = t_a + \frac{P_j}{h_c S} \left(1 - e^{-\frac{\tau}{T_0}}\right), \tag{2}$$

where P_j is the power losses transferred heat that can be expressed as

$$P_j = r_{20} (1 + \alpha (t_{wr} - 20)) I_1^2 l_{wr},$$

r_{20} denotes electrical resistivity of the wire for direct current at 20 °C, I_1 is the load current of the line, l_{wr} denotes the length of wire section and α stands for the temperature coefficient for material of wire.

After substituting for P_j into (2) we have

$$t_{wr} = t_a + \frac{r_{20} (1 + \alpha (t_{wr} - 20)) I_1^2 l_{wr}}{h_c S} \left(1 - e^{-\frac{\tau}{T_0}}\right). \tag{3}$$

From equation (3), it follows that the temperature of the wire is determined by the current load of line I_1 , weather conditions h_c , t_a , and the resistivity value r_{20} which depends on the temperature of the wire. A preliminary investigation showed that the temperature of wires changes in boundaries $t_0 \pm 5^\circ\text{C}$, while their resistivity varies within 2.5 %.

Therefore, in case of a small wire overheating, the replacement of t_{wr} by t_a does not introduce a significant error in calculations. Then the expression (3) may be

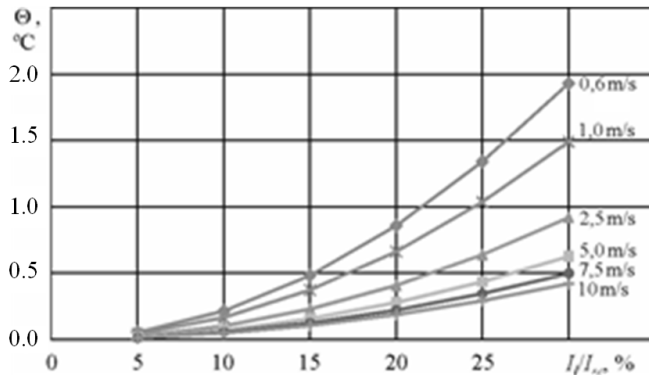


Fig. 3. Calculated curves of temperature change default values overheating wire AC-35/6

simplified to the form

$$t_{\text{wr}} = t_a + \frac{r_{20} (1 + \alpha (t_a - 20)) I_1^2 l_{\text{wr}}}{h_c S} \left(1 - e^{-\frac{\tau}{T_0}} \right). \quad (4)$$

If $\tau \rightarrow \infty$ then $T_0 \rightarrow 0$, so that (4) takes the form

$$t_{\text{wr}} = t_a + \frac{r_{20} (1 + \alpha (t_a - 20)) I_1^2 l_{\text{wr}}}{h_c S}. \quad (5)$$

Consequently, the overheating temperature of overhead power lines wire against ambient air will be

$$\Theta = t_{\text{wr}} - t_a = \frac{r_{20} (1 + \alpha (t_a - 20)) I_1^2 l_{\text{wr}}}{h_c S}. \quad (6)$$

According to equation (6) we calculated the temperature of overheating of the most common wires type A (AC) [6] which are used in electrical distribution networks. The calculations are produced for the most typical environmental conditions preceding process of icing: $v_0 = 0.6 \text{ div } 10 \text{ m/s}$, $t_0 = 1.0 \text{ }^\circ\text{C}$.

The results showed that the load currents of up to $0.25 I_{r.c}$ ($I_{r.c}$ being the operating current) do not affect the temperature of the wire, even with natural convection. A similar results were obtained in [9] for calculating the active resistance of overhead wires.

The calculated curves change default values of wires overheating level depending on its load factor $k_l = I_l / I_{r.c}$ taken for environmental conditions shown in Figs. 3–6.

4. Conclusion

Given the research results, it is possible to draw the following conclusions. In modern climatic and economic conditions, to develop measures to increase the effi-

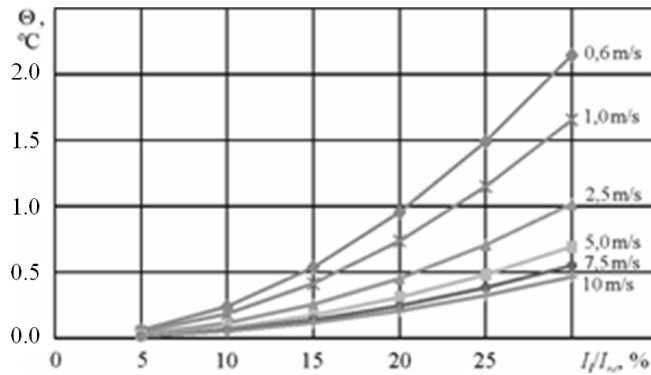


Fig. 4. Calculated curves of temperature change default values overheating wire AC-50

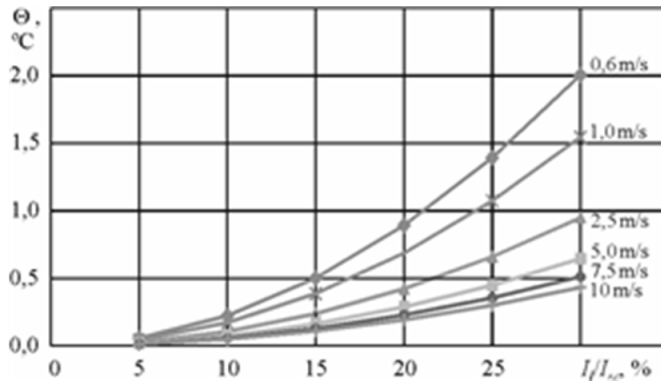


Fig. 5. Calculated curves of temperature change default values overheating wire AC-50/8

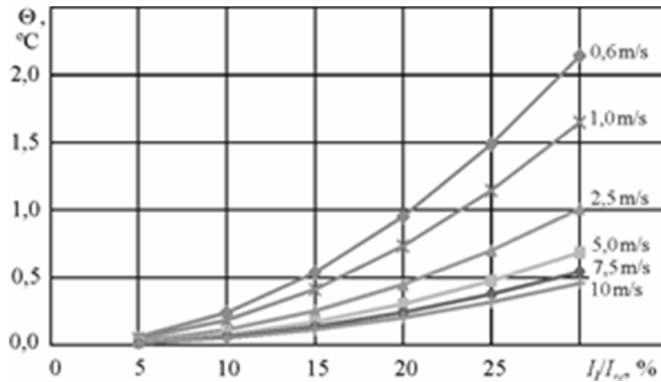


Fig. 6. Calculated curves of temperature change default values overheating wires AC-70/11 and 95/16

ciency of exploitation of 6–10 kV overhead power lines in icing formation conditions, there is a need to assess the effect of load currents on the temperature of the wire lines.

As a result of analysis of the schedules of daily electric loads for typical agricultural consumers, it was established that during the period of the most probable formation of glaze and rime deposits their load is in the range from 11 % to 35 % relative to the daily maximum.

As a result of a theoretical study of the temperature variation law of the wire in time flow for the most characteristic meteorological conditions, it is established that the load currents of lines up to $0.3 I_{r,c}$ increase the wire temperature from 0.3°C to 2.2°C , depending on the wind speed.

When creating technical devices for the implementation of information systems for monitoring overhead power lines in the conditions of icing, it is advisable to use an indirect approach to control. Since the actual temperatures of the branching wires to 10/0.4 kV transformer substations and the backbone networks at their loading $0.2 I_{r,c}$ that practically do not differ from the temperature of ambient air.

References

- [1] *Climate change in CIS countries in the 21st century*. Byulleten' federal'noy sluzhby po gidrometeorologii i monitoringu okruzhayushchey sredy 35 (2012), 13–15 (in Russian).
- [2] O. KOZLOVSKYI, A. ORLOVICH, S. SEREBRENNIKOV: *Automated system for forecasting of destructive atmospheric loads on elements of overhead power lines structures*. Technical Diagnostics and Non-Destructive Testing (2002), No. 2, 46–48 (in Russian).
- [3] O. KOZLOVSKYI, D. TRUSHAKOV, S. RENDZINYAK: *A measuring transducer in the system of technical diagnosis of overhead lines icing in electrical distribution networks*. Computational Problems of Electrical Engineering 5 (2015), No. 1, 17–22.
- [4] M. TS. TSYBIKORZHIEV, A. I. SELIVAKHIN, A. E. ORLOVICH, A. Z. VINAROV, R. SH. SAGUTDINOV: *A section of the power transmission line with a device for determining the surface temperature of its wires*. USSR Certification of authorship 1591118, September 07, 1990 (in Russian).
- [5] *Electrical installation regulations*. Kharkiv, Ukraine: Fort, 2014 (in Ukrainian).
- [6] *Uninsulated wires for aerial power lines. Specification*. GOST 839, 1980 (in Russian)
- [7] O. KOZLOVSKYI, A. ORLOVICH, A. NEKRASOV: *Rationale selection reasoning of icing test parameter on overhead lines of electric distribution network*. Electromechanical and Energy Saving Systems (2015), No. 3, 149–157 (in Ukrainian).
- [8] W. Z. BLACK, R. L. REHBERY: *Simplified model for steady state and real-time ampacity of overhead conductors*. IEEE Transactions on Power Application Systems 104 (1985), No. 10, 2942–2953.
- [9] V. VOROTNICKIY, O. TURKINA: *Estimation of variable losses calculation errors of electrical power HV line caused by unaccounted meteoconditions*. Elektrieskiye stantsii (2008), No. 10, 42–49 (in Russian).

Received 26. 10, 2017

Numerical study of the possibility of using cermet inserts in electromagnetic stirring application

KIRILL BOLOTIN¹, EVGENIY SHVYDKIY¹, IVAN SMOLYANOV¹, FEDOR TARASOV¹

Abstract. In a number of electromagnetic stirring applications in metallurgy there is a large working gap challenge due to the high temperature of liquid metal. An innovative approach to decreasing the non-magnetic gap is the application of magnetodielectric material. The proposed materials are capable of retaining their magnetic properties under the influence of high temperature. By means of COMSOL Multiphysics a numerical model for laboratory electromagnetic stirrer for electrically conductive fluid in rotating magnetic field is developed. Three dimensional electromagnetic, heat transfer and turbulence models are applied for the coupled problem. The results indicate a new path in the development of electromagnetic stirring technology

Key words. Electromagnetic stirring, magnetodielectric materials, rotating magnetic field, computational fluid dynamics, numerical simulation, COMSOL Multiphysics.

1. Introduction

Electromagnetic stirring technology occupies an important place in metallurgy. Slab [1], [2], round billet [3], [4] and bloom [5], [6] continuous casting machines are equipped with electromagnetic mold stirrers. Forced melt convection in a mold promotes a higher quality of cast steel [7] and a decrease in casting defects.

The solidification of light metals alloys and composite materials in the presence of traveling [8], [9] or rotating magnetic fields (RMF) [10], [11] has been widely investigated for many years. Crystal growth with electromagnetic stirring has a significant potential in semiconductor production [12], [13], [14].

Besides the listed above electromagnetic stirring applications for material quality control, this technology is successfully applied in the area of metallurgical processes. Electromagnetic stirrer installed on electric arc furnaces shows clear customer ben-

¹Department of Electrical Engineering and Electrotechnology, Ural Federal University, Mira st. 19, 620002, Ekaterinburg, Russian Federation

efits in energy saving, iron yield, alloy savings, as well as in other areas [15]. The necessity to save energy and increase productivity in aluminum re-melting furnaces is satisfied using electromagnetic stirrer also known as magnetohydrodynamic (MHD) stirrer which is placed under the furnace bottom [16] and can be used alongside different inductor design [17].

Large presence of presented installation in industry is explained by several advantages, such as the occurrence of induced Lorenz forces directly in the liquid metal. Introducing these forces does not require the use of any mechanical moving parts. Electromagnetic influence is easily controllable and almost inertialess, since it is only necessary to control the electric power of the device. That is why it is used for modernization of the electromagnetic stirring units to improve efficiency and reduce energy costs, in the following directions:

- studies of the effect of the supply frequency and current,
- studies of the effect of the inductor design,
- studies of the effect of the width of non-magnetic working gap.

The working gap represents the space between the melt and the near side of the inductor. Usually it is filled with a furnace lining which carries heat-insulation and exhibits refractory functions. The correlation between the thickness of the working gap and the efficiency of the inductor has been studied well [18], [19]. The width of the gap is limited by the thermal end electromagnetic efficiency. An increase in gap leads to an almost thermally insulated furnace condition, but magnetic flux density in the melt will be damped. And the opposite decrease in gap thickness will generate high magnitude of magnetic flux density in melt. This problem can be solved in several ways:

- increasing the length of the inductor tooth and putting it in the lining,
- using special insertion from materials combining the dielectric and magnetic properties that are also capable of working at high temperature conditions.

The first method has a number of significant disadvantages, of which the main ones are the mechanical weakening of the refractory lining structure and a differing coefficient of volume thermal expansion between the tooth and furnace lining. The aforementioned disadvantages can lead to accidents in the plant.

The second method does not have these disadvantages. The typical materials used in electrical motors and electrotechnological installations are ferrites and magnetodielectrics. Ferrites have a high operating temperature, but low saturation induction which prevents them from being used in metal stirring units. Magnetodielectrics are composite materials consisting of soft magnetic powder and an epoxy resin. They have a high saturation induction, but the working temperature is limited by the working temperature of the used resin and rarely exceeds 250 °C [19].

To eradicate this disadvantage, it is possible to use one of cermet compounds in which the resin is replaced with a ceramic filler. The basic magnetic properties such as Curie point, saturation induction and relative magnetic permeability depend on

the choice of material. Out of these three parameters, only the magnetic permeability depends on the concentration of magnetic material in the cermet. Therefore, it is important to use a magnetic material which has a maximum value of relative magnetic permeability in pure form.

The most suitable and affordable is the compound $\text{Fe-Al}_2\text{O}_3$, because the iron contained in it has one of the largest relative permeability values, with $\mu = 20000$. Various research has shown that the values of the relative magnetic permeability in such compounds ranging from 5 to 90 [20], [21], [22]. This paper presents the results of numerical simulation of the standard and modernized laboratory stirrer, as well as a comparison of the results. At the second stage, the melt temperature homogenization time was compared between the modernized and standard stirrer.

2. The model of the stirrer

Geometry preparing, meshing, and coupled multiphysics numerical calculation were performed in COMSOL Multiphysics simulation software.

2.1. Three-dimensional geometry

The investigated model of modernized stirrer is shown in Fig. 1. The model includes molten metal, magnetodielectric inserts, inductor windings, magnetic core and air (hidden). The inductor is a group of copper rods which are arranged into magnetic core slots. Magnetodielectric inserts are placed above the laminated magnetic core. The inductor is supplied from a 3 phase source and generates rotating magnetic field (RMF), which goes through core teeth and inserts into molten metal. The well electrically conductive melt under RMF begins to rotate around an axis Z .

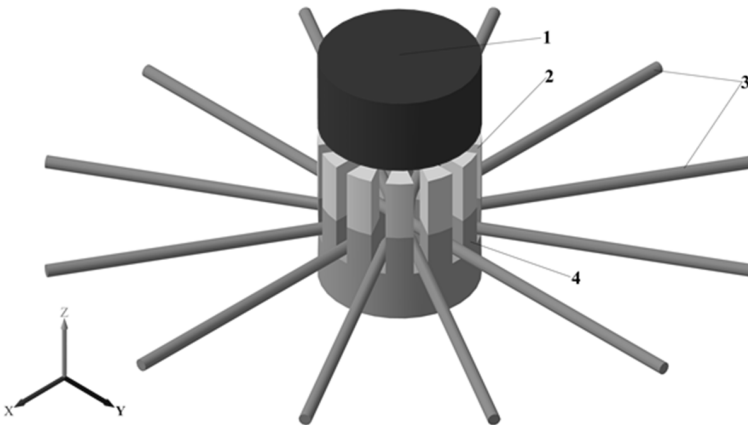


Fig. 1. The modernized electromagnetic stirrer with melt: 1—molten metal, 2—magnetodielectric inserts, 3—inductor windings, 4—magnetic core of inductor

The physical parameters and dimensions of the model correspond to the real-life laboratory stirrer parameters and are shown in Table 1.

Table 1. Dimensions and parameters of the model

Item	Value
molten metal diameter [mm]	100
molten metal height [mm]	60
magnetic core diameter [mm]	100
magnetic core slot depth [mm]	27
relative permeability of magnetic core	1200
molten metal conductivity [S/m]	$5 \cdot 10^6$
molten metal density [kg/m ³]	2400
molten metal dynamic viscosity [Pa·s]	0.002
current magnitude [A]	500
supply frequency [Hz]	50

2.2. Electromagnetic part

At the first stage the electromagnetic problem was solved. Taking the complexity of numerical simulation into consideration, the following assumptions are accepted to simplify the model:

- the electromagnetic (EM) field is quasistatic and the displacement currents are ignored,
- the time varying EM force is replaced by the time averaged EM force,
- the influence of molten steel movement on EM field is ignored, since the magnetic Reynolds number is greater than 1.

The distribution of electromagnetic field in space is described by Maxwell's equations. For the quasi-static magnetic field in this article, differential forms of Maxwell's equations are expressed as

$$\nabla \times \underline{\mathbf{H}} = \underline{\mathbf{J}}, \quad (1)$$

$$\underline{\mathbf{B}} = \nabla \times \underline{\mathbf{A}}, \quad (2)$$

$$\underline{\mathbf{E}} = -j\omega \underline{\mathbf{A}}, \quad (3)$$

$$\underline{\mathbf{J}} = \sigma \underline{\mathbf{E}} + j\omega \underline{\mathbf{D}}, \quad (4)$$

where \mathbf{E} is the electric field strength, \mathbf{B} is the magnetic flux density, \mathbf{H} is the magnetic field strength, \mathbf{J} is the current density, \mathbf{D} is the electric flux density and σ is electrical conductivity. The underlined symbols mean phasors of the above quantities.

In the software, coil modeled by an additional block in physic interface is called Multi-turn coil. The current density in it is

$$\mathbf{J}_e = \frac{N \cdot I_{\text{coil}}}{A} \mathbf{e}_{\text{coil}}, \quad (5)$$

where \mathbf{J}_e is the external current density, N is number of turns in the coil, I_{coil} denotes the magnitude of current in coil; A represents the total cross-section of the coil wire and \mathbf{e}_{coil} stands for the unit vector of current direction.

During the numerical simulation, the obtained volumetric force \mathbf{f} is expressed as a time averaged quantity in the form

$$\mathbf{f} = \frac{1}{2} \cdot \text{Re}(\mathbf{J} \times \mathbf{B}^*), \quad (6)$$

where Re is the real part of the complex quantity and \mathbf{B}^* is the conjugate complex number of magnetic flux density.

2.3. Hydrodynamic part

The source term for transient hydrodynamic (HD) part is the volumetric EM force. The HD calculation is based on Navier-Stokes equations with an additional EM force term

$$\rho(\mathbf{u} \cdot \nabla)\mathbf{u} = \nabla[-p\mathbf{I} + (\eta + \eta^T)(\nabla\mathbf{u} + (\nabla\mathbf{u}^T))] + \mathbf{f}, \quad (7)$$

$$\nabla \cdot \mathbf{u} = 0, \quad (8)$$

where ρ is the density, η is the viscosity for the turbulent flow, p is the pressure, and \mathbf{u} denotes the Favre-averaged velocity vector.

Table 2 shows the values of basic criteria to determine the type and parameters of the liquid metal motion

Table 2. Estimated parameters for HD part

Parameter	Values
Reynolds number	$10^4 - 10^5$
magnetic Reynolds number (Re_m)	10^{-2}
Hartmann number	$3 \cdot 10^2$

The Reynolds number indicates on fully developed turbulent flow, thus the $k - \omega$ SST turbulence model is used. In magnetohydrodynamic applications, this model corresponds well to experimental data [23]. The magnetic Reynolds number indicates that the magnetic field of the melt does not affect the inductor magnetic field ($Re_m \ll 1$). And the electromagnetic forces are significantly superior to viscous forces as is shown by the Hartmann number.

Intensive liquid metal moving leads to change of free surface shape and position

[24] especially in induction crucible furnace [25]. But in our case of rotating liquid in cylindrical free surface vessel [26] this is not a crucial factor and will not be included in computations.

2.4. Heat transfer part

In heat transfer formulation certain physical properties such as density and viscosity are dependent on temperature. The thermal convection which is caused by temperature difference is ignored.

The initial condition for thermal part is a temperature gradient between top and bottom melt surface and is equal to $\Delta T = 15^\circ\text{C}$.

The heat equation for model heat transfer in fluids can be written in the form

$$\rho C_p \frac{\partial T}{\partial t} + \rho C_p \mathbf{u} \cdot \nabla T + \nabla \cdot \mathbf{q} = Q, \quad (9)$$

$$\mathbf{q} = -k \nabla T, \quad (10)$$

where ρ is the density of the environment, C_p is the fluid heat capacity at a constant pressure, k is the fluid thermal conductivity, and Q denotes the Joule heating sources from the EM part.

2.5. Mesh parameters

Since different types of problems have different requirements concerning the size of the mesh elements, two types of meshes were built. The first one was designed for the electromagnetic problem, the second one for the hydrodynamics and heat transfer.

Figure 2 shows the first mesh, the size of the finite elements in the melt was determined based on the depth of current penetration at 50 Hz, which is equal to 3 mm, the number of elements in the melt of 250 000, the total number of elements is 540 000.

Figure 3 depicts the second mesh. It was built only in the melt subdomain in order to save computing power, the size of elements is equal to $\sigma = 0.1$ mm, the total number of elements is 440 000.

3. Numerical results and discussion

At the first stage the electromagnetic problem was calculated for the unmodernized unit (without inserts) with the working gap ranging from 10 to 100 mm, as well as the modernized unit, with the same values of the working gap, thus, the distance between melt bottom surface and the upper side of the magnetodielectric inserts always remained constant and equal to 10 mm. The inserts length varies from 10 to 90 mm. The effect of the inserts' relative magnetic permeability changing from 5 to 90 is studied. Because the maximum electromagnetic force is directly proportional

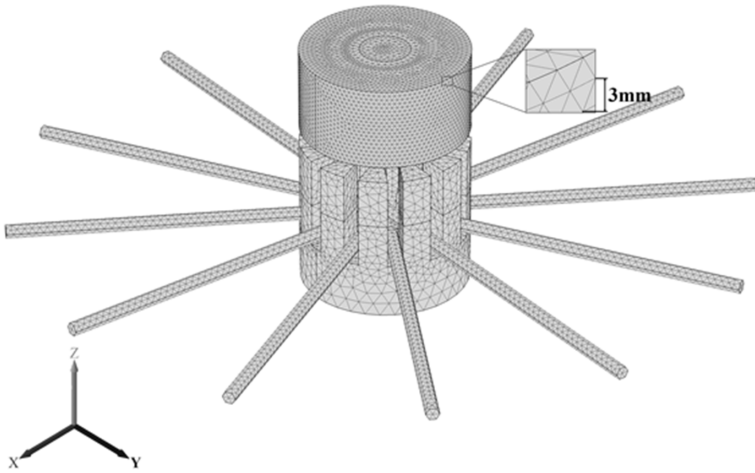


Fig. 2. Mesh for electromagnetic part

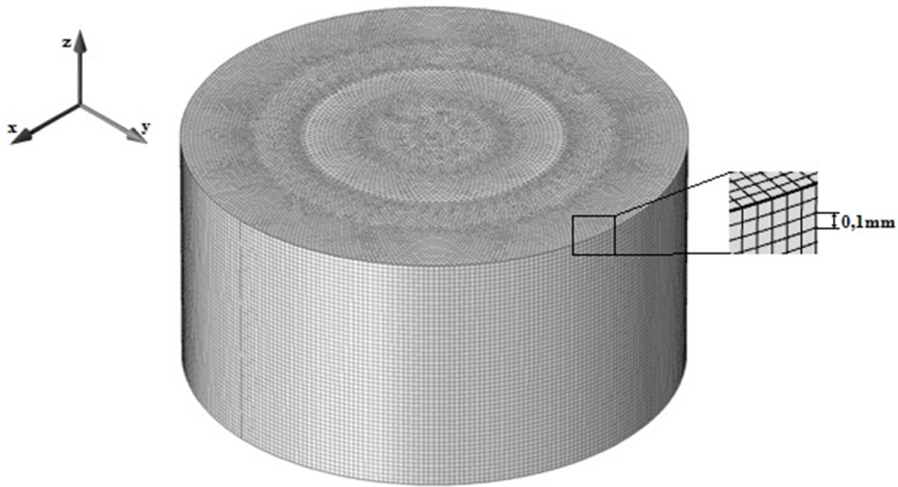


Fig. 3. Numerical mesh for hydrodynamic and heat transfer calculations

to the square of magnetic flux density B , it was chosen as the evaluation parameter.

Figure 4 shows a three-dimensional view of the magnetic flux density in the inductor core, two maximum values corresponding to three-phase power supply.

Figure 5 shows a 3D view of the electromagnetic volume force vector field in the melt subdomain for the standard stirrer with a working gap 25 mm (left) and for the modernized stirrer with a working gap equal to 40 mm. The value of relative magnetic permeability is equal to 5. Two maximum values of volume force correspond to the pattern of magnetic flux density.

The results of the magnetic flux density calculations for the modernized and

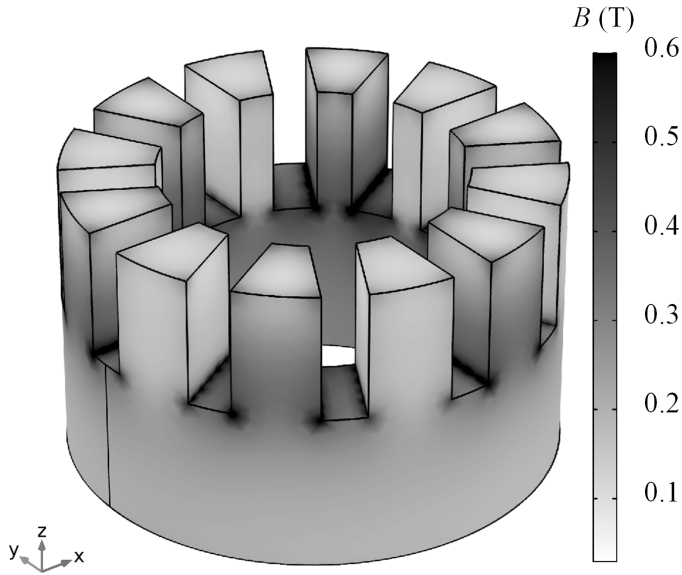


Fig. 4. Magnetic flux density in magnetic core of inductor

standard stirrers, depending on the size of the working gap are showed in Fig. 6. As can be seen, the presence of inserts allows the value of induction to be maintained with increasing working clearance. It is also clear that the value of relative magnetic permeability significantly affects the amount of induction at a constant value of the working gap.

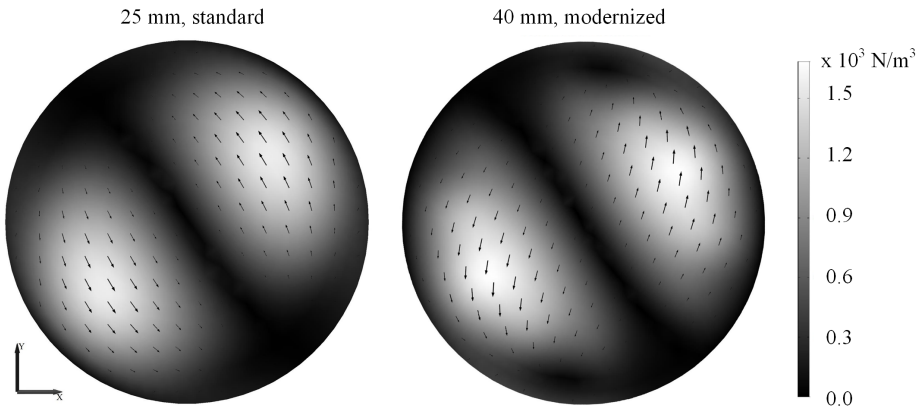


Fig. 5. Electromagnetic force vector field for standard and modernized stirrers

The occurring electromagnetic forces begin to spin up the liquid metal. Our velocity field evaluation is available as a supplementary online material. Due to the fact that the inductor is under the melt, first the velocities arise in the lower layers

of the vessel. Then they gradually penetrate into the upper layers and untwist the entire volume of liquid metal to 0.16 m/s. In the axial zone they create complex vortices. This indicates developed turbulent flow and the $k - \omega$ SST HD model is suitable to model this application.

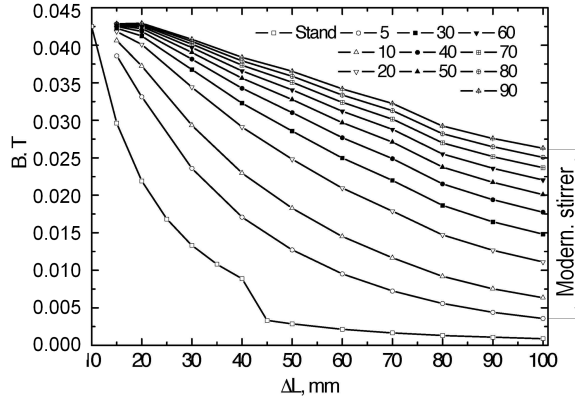


Fig. 6. Magnetic flux density for standard and modernized stirrers for different value of relative magnetic permeability depending on the width of working gap

Temperature homogenization is a crucial factor indicating the efficiency of stirring. The shorter homogenization time determines the more effective mixing mode. A comparison of a standard stirrer with a working gap value of 10 mm, 25 mm and 40 mm, and a modernized stirrer with the working gap of 40 mm and relative magnetic permeability of 5 is given in Fig. 6. Thus, a comparison was made for a unit with magneto-dielectric insert, a standard stirrer having the same working gap value of 40 mm and for a stirrer having a close value of the induced magnetic flux density $B \approx 17 - 18$ mT, as well a comparison with a standard laboratory stirrer.

Figure 7 shows the time dependence of temperature equalization in the central plane of the melt for a standard stirrer with working gap 25 mm and modernized stirrer with working gap equal 40 mm. We can observe the dynamics of the metal temperature equalization. First, the metal retains the temperature gradient. Second, it is seen how in two places the hot metal penetrates into the upper layer. Third, centrifugal forces prevail, the hotter metal is pressed to the walls of the vessel. After 8 seconds, the entire volume of metal obtains the same temperature in both cases. And it can be seen that an increase of the working gap does not reduce the stirring speed.

Figure 8 shows the dependence of the maximum and minimum values of the temperature in molten metal volume on time, for three types of stirrers.

It can be seen from the above results that not only the maximum value of the magnetic flux density, and hence the EM force value, is retained in the modernized stirrer, but also its general nature, which allows the speed and time to be maintained for which the temperature in the molten metal volume is equalized, increasing the value of the working gap by a factor of 1.5–2. At the same time, the modernized stirrer with inserts, and relative magnetic permeability value equal to 5 was studied

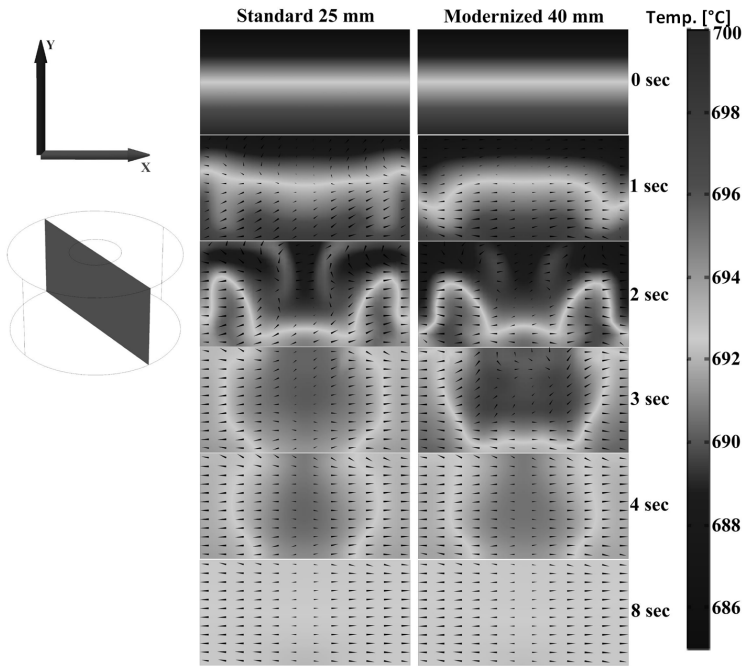


Fig. 7. Numerical result of the time dependence of temperature homogenization in the central plane of the melt for a standard stirrer with working gap 25 mm and modernized stirrer with working gap 40 mm (arrows show velocity field and grade of grey color shows temperature)

in detail. Thus, the use of inserts with a large value of this parameter will be able to further increase the working gap while maintaining the inductor efficiency.

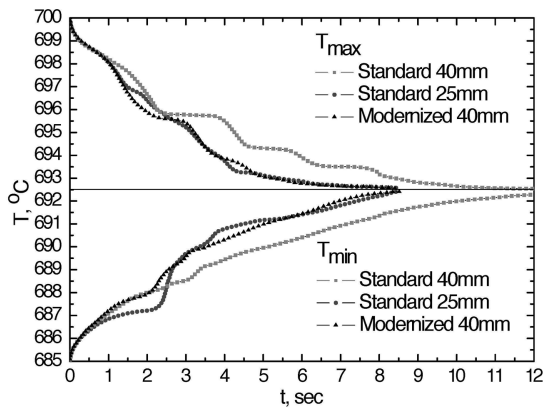


Fig. 8. Dependence of maximum and minimum values of temperature in molten metal on time

4. Conclusion

The proposed method for the modernization of electromagnetic metallurgical stirrer has been numerically investigated.

The use of cermet based on Fe-Al₂O₃ inserts allows holding a high efficiency of electromagnetic stirring to be maintained with the assumption that the thermal insulation layer (working gap) will be increased by the factor from 1.5 to 2. However, these magnetic materials have not been studied well at high temperatures and carrying out such experimental research is the next step a long term project. Successful tests will increase the demand for electromagnetic stirring technology and reduce costs in the production of steel and non-ferrous metals.

The additionally proposed method might be applied to model liquid aluminium MHD transportation systems [25], [27].

References

- [1] K. FUJISAKI: *In-mold electromagnetic stirring in continuous casting*. IEEE Transactions on Industry Applications *37* (2001), No. 4, 1098–1104.
- [2] C. T. LIU: *Three-dimensional design and performance assessments of a linear induction-type electromagnetic stirrer*. IEEE Transactions on Industry Applications *46* (2010), No. 1, 54–59.
- [3] Y. HAIQI, Z. MIAOYONG: *Three-dimensional magnetohydrodynamic calculation for coupling multiphase flow in round billet continuous casting mold with electromagnetic stirring*. IEEE Transactions on Magnetics *46* (2010), No. 1, 82–86.
- [4] X. GENG, X. LI, F. B. LIU, H. B. LI, H. JIANG: *Optimisation of electromagnetic field and flow field in round billet continuous casting mould with electromagnetic stirring*. Ironmaking & Steelmaking: Processes, Products and Applications *42* (2005), No. 9, 675–682.
- [5] R. HIRAYAMA, K. FUJISAKI, T. YAMADA: *Dual in-mold electromagnetic stirring in continuous castings*. IEEE Transactions on Magnetics *40* (2004), No. 4, 2095–2097.
- [6] L. B. TRINDADE, A. C. F. VILELA, A. F. F. FILHO, M. T. M. B VILHENA, R. B. SOARES: *Numerical model of electromagnetic stirring for continuous casting billets*. International IEEE Transactions on Magnetics *38* (2002), No. 6, 3658–3660.
- [7] H. Q. YU, M. Y. ZHU: *Influence of electromagnetic stirring on transport phenomena in round billet continuous casting mould and macrostructure of high carbon steel billet*. Ironmaking & Steelmaking: Processes, Products and Applications *39* (2012), No. 8, 574–584.
- [8] V. BOJAREVICS, K. PERICLEOUS, M. GARRIDO, Y. FAUTRELLE, L. DAVOUST: *Travelling magnetic field mixing for particle dispersion in liquid metal*. Magnetohydrodynamics *51* (2015), No. 3, 249–255.
- [9] E. L. SHVIDKIY, B. A. SOKUNOV, I. A. USKOV, I. A. SMOLYANOV: *Simulation of continuous casting process with electromagnetic influence to the ingot liquid phase*. Proc. IEEE North West Russia Section Young Researchers in Electrical and Electronic Engineering Conference, 2–3 Feb. 2016, Saint Petersburg, Russia, 685–688.
- [10] S. ECKERT, P. A. NIKRITYUK, B. WILLERS, D. RÄBIGER, N. SHEVCHENKO, H. NEUMANN-HEYME, V. TRAVNIKOV, S. ODENBACH, A. VOIGT, K. ECKERT: *Electromagnetic melt flow control during solidification of metallic alloys*. The European Physical Journal Special Topics *220* (2013), No. 1, 123–137.
- [11] S. DENISOV, V. DOLGIKH, S. YU. KHRIPCHENKO, I. KOLESNICHENKO, I. NIKULIN: *The effect of traveling and rotating magnetic fields on the structure of aluminum alloy*

- during its crystallization in a cylindrical crucible. *Magnetohydrodynamics* 50 (2014), No. 4, 407–422.
- [12] K. DADZIS, K. NIEMIETZ, O. PÄTZOLD, U. WUNDERWALD, J. FRIEDRICH: *Non-isothermal model experiments and numerical simulations for directional solidification of multicrystalline silicon in a traveling magnetic field*. *Journal of Crystal Growth* 372 (2013), No. 8, 145–156.
- [13] N. DROPKA, W. MILLER, R. MENZEL, U. REHSE: *Numerical study on transport phenomena in a directional solidification process in the presence of travelling magnetic fields*. *Journal of Crystal Growth* 312 (2010), No. 8, 1407–1410.
- [14] V. GEŽA, B. NACKE, E. BAAKE, A. JAKOVICS: *Anisotropy of flow and transition between mixing regimes in a physical model of directional solidification*. *Magnetohydrodynamics* 51 (2015), No. 1, 15–24.
- [15] R. B. FDHILA, U. SAND, J. E. ERIKSSON, H. YANG: *A stirring history*. *ABB Review* 3 (2016), 45–48.
- [16] V. N. TIMOFEEV, M. Y. KHATSAYUK: *Theoretical design fundamentals for MHD stirrers for molten metals*. *International Journal of Heat and Mass Transfer* 53 (2010), Nos. 11–12, 2477–2483.
- [17] S. YU. KHRIPCHENKO, S. DENISOV, V. DOLGIKH, F. PAVLINOV: *Use of a travelling magnetic field "ROD" inductor for stirring molten metal in an aluminum bath*. *Magnetohydrodynamics* 52 (2016), No. 3, 407–416.
- [18] A. PEDCHENKO, YU. GELFGAT: *Study of the influence of current frequency and non-magnetic gap value on the efficiency of Al-alloys stirring in metallurgical furnaces*. *Magnetohydrodynamics* 43 (2007), No. 3, 363–375.
- [19] T. V. AKIMOVA, D. G. KRUTOGIN, YU. M. KRAYUSHKINA, A. D. ROGOVOI: *Ferrite materials for high temperature applications*. *Materials of Electronic Technics* 54 (2010), No. 2 (in Russian).
- [20] J. T. KLOMP: *Microstructural and physical properties of Al_2O_3Fe cermets*. *Ceramurgia International* 4 (1978), No. 2, 59–65.
- [21] C. TIEN, E. V. CHARNAYA, V. M. GROPYANOV, I. S. MIKHAILOVA, C. S. WUR, A. A. ABRAMOVICH: *Magnetic properties of a cermet on the base of $FeAl_2O_3$* . *Journal of Magnetism and Magnetic Materials* 220 (2000), Nos. 2–3, 147–151.
- [22] M. YAGHTIN, A. H. TAGHVAEI, B. HASHEMI, K. JANGHORBAN: *Structural and magnetic properties of $FeAl_2O_3$ soft magnetic composites prepared using the sol-gel method*. *International Journal of Materials Research* 105 (2014), No. 5, 474–479.
- [23] S. SPITANS, A. JAKOVICS, E. BAAKE, B. NACKE: *Numerical modeling of free surface dynamics of melt in an alternate electromagnetic field: part I. Implementation and verification of model*. *Metallurgical and Materials Transactions B* 44 (2013), No. 3, 593–605.
- [24] I. DOLEŽEL, P. ŠOLIN, M. ZÍTKA, B. ULRYCH: *On electromagnetic stirring of molten metals*. *Acta Technica CSAV* 50 (2005), No. 1, 35–51.
- [25] E. GOLOVENKO, E. PAVLOV, V. KOVALSKY, V. GOREMYKIN, A. AVDULOV, Y. AVDULOVA: *Numerical simulation of the operation modes of the cylindrical MHD-pump for dispensing molten aluminum from the stationary mixer*. *Magnetohydrodynamics* 46 (2010), No. 1, 425–436.
- [26] B. MIKHAILOVICH, O. BEN-DAVID, AVI LEVY: *Liquid metal rotating flow under permanent magnetic system impact*. *Magnetohydrodynamics* 51 (2015), No. 1, 171–176.
- [27] K. E. BOLOTIN, E. L. SHVYDKIY, V. E. FRIZEN, I. A. SMOLYANOV: *Numerical simulation of electromagnetic processes of the modernized MHD-pump for dispensing molten aluminium from the stationary induction furnace*. *Proc. IEEE Conference of Russian Young Researchers in Electrical and Electronic Engineering*, 1–3 Feb. 2017, Saint Petersburg, Russia.

Effects of viscous dissipation and heat generation in a Maxwell fluid flow past a stretching surface in a porous medium with radiation

MANISH RAJ¹, ABHAY KUMAR JHA^{2,3}, ANIL SHARMA¹

Abstract. This paper examines the problem of a non-Newtonian fluid flow over a continuously stretching permeable surface in the presence of thermal radiation, viscous dissipation and heat generation. The governing non-linear partial differential equations are transformed to a system of non-linear ordinary differential equations by using suitable similarity transformations. The transformed systems of equations are solved numerically using fourth-order Runge–Kutta method along with the shooting technique. The effects of Maxwell parameter, permeability parameter, suction/blowing parameter, thermal radiation parameter and heat generation parameter are shown graphically.

Key words. Heat generation, viscous dissipation, Maxwell fluid, stretching surface, thermal radiation.

1. Introduction

The studies of boundary layer flows of a non-Newtonian fluid over a stretching surface of a moving plate have received much attention because of their extensive applications in the field of metallurgy, chemical engineering and particularly, in the extrusion of polymer sheet, from a die or in the drawing of plastic films [1–5]. The mathematical model of Maxwell fluid has been used as a simplified description of dilute polymeric solution/fluids and has also been used to describe the rheology of flows clough as well as other fluids including glycerin, tolerance, crude oil etc. [6–7]. The effect of viscous dissipation changes the temperature distribution by playing a role as energy source and affects the heat transfer rates. The most of the

¹Department of Mathematics, University of Rajasthan, Jaipur-302004, India

²Department of Mathematics, J. N. College Madhubani (Bihar), India

³Corresponding author; e-mail: itsabhay@rediffmail.com

effect of viscous dissipation depends on whether the plate is being cooled or heated. Chen [8] examined the effect of combined heat and mass transfer on MHD free convection from a vertical surface with the Ohmic heating and viscous dissipation. Pal and Hiremath [9] determined the heat transfer characteristics in the laminar boundary layer flow over an unsteady stretching sheet placed in a porous medium in the presence of viscous dissipation and internal absorption or generation. Vajravelu and Hadjirinicolaou [10] studied the effects of viscous dissipation and internal heat generation. Veena et al. [11] obtained the studied heat transfer in a viscoelastic fluid past a stretching sheet with viscous dissipation and heat generation.

The study of heat generation or absorption and effects of radiation on heat transfer is important in many physical problems. The effects of non-uniform heat generation/absorption on heat transfer in Newtonian and non-Newtonian fluid flow over stretching/shrinking surface has been studied by many authors [12–23] under various physical situations.

2. Mathematical formulation

We consider an unsteady flow of non-Newtonian Maxwell fluid past stretching sheet in porous medium with radiation and heat generation, taking into account. The governing equations for the flow can be written as

$$\frac{\partial u}{\partial x} + \frac{\partial v}{\partial y} = 0, \quad (1)$$

$$\frac{\partial u}{\partial t} + u \frac{\partial u}{\partial x} + v \frac{\partial u}{\partial y} + \lambda \left(u^2 \frac{\partial^2 u}{\partial x^2} + v^2 \frac{\partial^2 u}{\partial y^2} + 2uv \frac{\partial^2 u}{\partial x \partial y} \right) = \nu \frac{\partial^2 u}{\partial y^2} - \frac{\nu}{k} u, \quad (2)$$

$$\frac{\partial T}{\partial t} + u \frac{\partial T}{\partial x} + v \frac{\partial T}{\partial y} = k_m \frac{\partial^2 T}{\partial y^2} - \frac{1}{\rho C_p} \frac{\partial q_r}{\partial y} + \frac{\mu}{\rho C_p} \left(\frac{\partial u}{\partial y} \right)^2 + \frac{q'''}{\rho C_p}. \quad (3)$$

Here, u , v are the components of velocity in the x and y directions, respectively, ρ is the fluid density, C_p is the specific heat, k denotes the permeability parameter and

$$q_r = \frac{4\sigma}{3K^*} \frac{\partial T^4}{\partial y}, \quad k(t) = k_0(1 - \alpha t),$$

where ν is the kinematic viscosity of the fluid, k is the thermal conductivity and k_m stands for the thermal diffusivity.

The internal heat generation or absorption form q''' is modeled as

$$q''' = \frac{\rho k u_w}{K x} [A^* T_w - T_\infty] e^{-\eta} + B^* (T - T_w), \quad (4)$$

where A^* and B^* are the coefficient of space and temperature dependent sheet generation/absorption. Here $A^* > 0$ and $B^* > 0$ corresponds to internal heat generation, while $A^* < 0$ and $B^* < 0$ corresponds to internal heat absorption.

The appropriate boundary conditions are:

$$\left. \begin{aligned} y = 0 : \quad & u = U(x, t), \quad v = v_w(t), \quad T = T_w(x, t), \\ y \rightarrow \infty : \quad & u \rightarrow 0, \quad T \rightarrow T_\infty. \end{aligned} \right\}, \quad (5)$$

where $T = T_w$ is taken as $T_w(x, t) = T_\infty + bx(1 - \alpha t)^{-2}$, T_∞ is the constant free-stream temperature, $v_w(t) = -v_0/\sqrt{1 - \alpha t}$ is the velocity of suction ($v_0 > 0$) or blowing ($v_0 < 0$). If b is positive (negative), then the wall temperature T_w increases (decreases) the expressions for $U(x, t)$, $T_w(x, t)$, $\lambda(t)$, $K_1(t)$ and $v_w(t)$ valid for the time $t < \alpha^{-1}$.

3. Analysis of the problem

The continuity equation (1) is identically satisfied by a stream function $\psi(x, y)$ defined as

$$u = \frac{\partial \psi}{\partial y}, \quad v = -\frac{\partial \psi}{\partial x}.$$

For the solution of momentum and energy equations, the following dimensionless variables are defined:

$$\theta = \frac{T - T_\infty}{T_w - T_\infty}, \quad \eta = \sqrt{\frac{c}{\nu(1 - \alpha t)}}y, \quad \psi = \sqrt{\frac{\nu c}{(1 - \alpha t)}}xf(\eta), \quad T = T_\infty + \frac{bx\theta(\eta)}{(1 - \alpha t)^2}.$$

With the help of these relations, the governing equations reduce to

$$M \left(\eta \frac{f''}{2} + f' \right) + f'^2 - ff' + \beta(f^2 f''' - 2ff' f'') = f''' - k_1 f', \quad (6)$$

$$M \frac{\eta \theta'}{2} + f' \theta - f \theta' = \frac{1}{\text{Pr}} \left(1 + \frac{4}{3N} \right) \theta'' + \text{Ec} |f''|^2 + \gamma^* e^{-\eta} + \gamma \theta \quad (7)$$

and the boundary conditions (4) become

$$\left. \begin{aligned} \eta = 0 : \quad & f' = 1, \quad f = S, \quad \theta = 1, \\ \eta \rightarrow \infty : \quad & f' \rightarrow 0, \quad \theta \rightarrow 0. \end{aligned} \right\} \quad (8)$$

In equations (6)–(8) the quantity $M = \alpha/c$ denotes the unsteadiness parameter, $\beta = c\lambda_0$ is the Maxwell parameter, $k_1 = \nu/(k_0 c)$ stands for the permeability parameter, $\text{Pr} = \nu/k_m$ represents the Prandtl number, $N = k_m k^*/(4\sigma T_\infty)$ is the radiation parameter and $S = v_0/\sqrt{\nu c}$ denotes the suction/blowing parameter. Further, Ec is the Eckert number ($\text{Ec} = U(x, t)^2/(C_p(T_w - T_\infty))$), $\gamma = kB^*/(KC_p)$ is the temperature-dependent generation/absorption parameter and $\gamma^* = kA^*/(KC_p)$ denotes the space-dependent generation/absorption parameter.

For $\text{Ec} = 0$, $\gamma^* = 0$ and $\gamma = 0$, equation [6] reduces to the corresponding energy equation given by S. Mukhopadhyay [23]

Equations (5) and (6) along with the boundary condition (7) were solved nu-

merically using Runge–Kutta fourth order algorithm with a systematic guessing of $f''(0)$ and $\theta'(0)$ by shooting technique until the boundary condition in infinity are satisfied. The step size $\Delta\eta = 0.001$ is used while obtaining the numerical solution and accuracy upto seventh decimal place.

4. Results and discussion

Figures 1(a) and 1(b) show the effect of the Maxwell parameter β on the velocity profiles for both steady and unsteady motions. The value $\beta = 0$ gives a viscous incompressible Newtonian fluid. It is observed that for both steady and unsteady motions, increasing values of β decrease the velocity; hence the thickness of the boundary layer decreases. An increase in β enhances the temperature and its gradient on the surface (Fig. 1(c)). Thus, the heat transfer rate at the surface increases with increasing β .

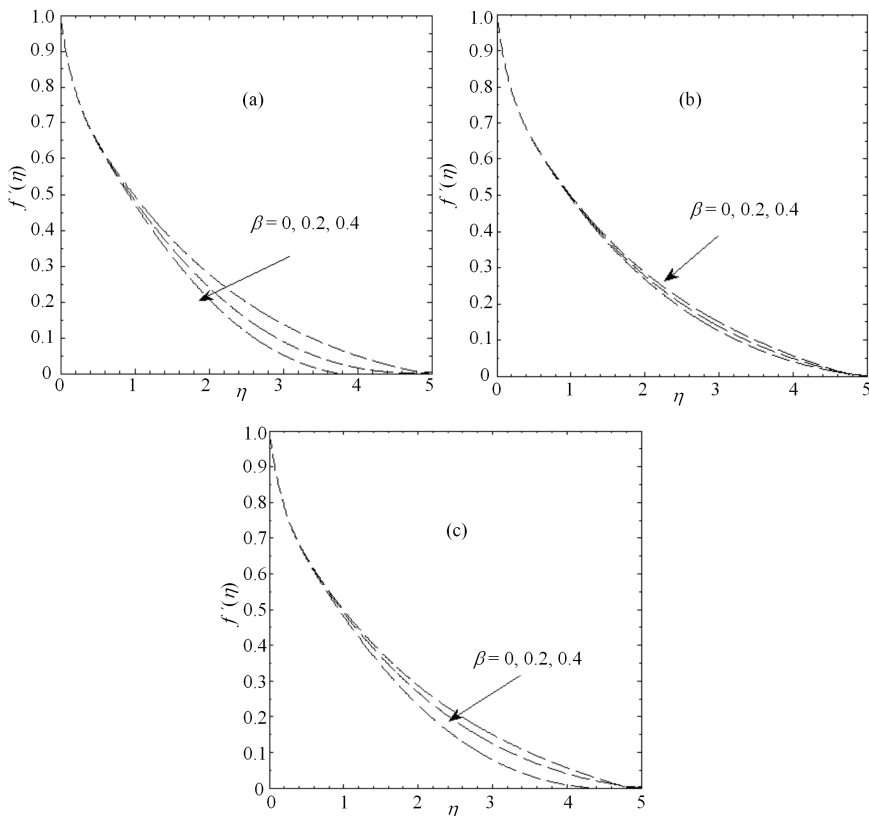


Fig. 1. Velocity (a),(b) and temperature profiles (c) for $k_1 = 0.1$, $S = 0.1$, different values of Maxwell parameter β and for (a) $M = 0$, (b) $M = 0.3$, (c) $M = -0.3$, $N = 1$, $Pr = 0.7$, $\gamma^* = \gamma = Ec = 0$

The effects of the permeability parameter k_1 on the velocity field and temperature profile are exhibited in Fig. 2(a) and 2(b).

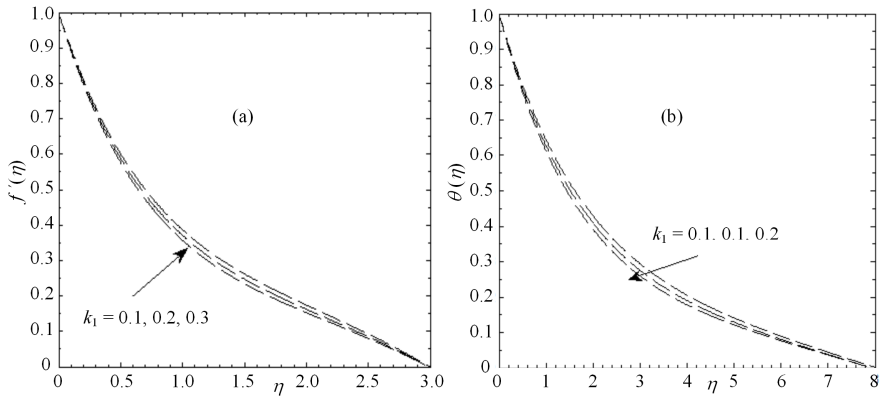


Fig. 2. Velocity (a) and temperature profiles (b) for different values of permeability parameter k_1 and for (a) $M = 0.3$, $\beta = 0.2$, $S = 0.1$, (b) $M = 0.3$, $\beta = 0.2$, $S = 0.1$, $N = 1$ and both (a) and (b) $\text{Pr} = 0.7$, $\gamma^* = \gamma = \text{Ec} = 0$

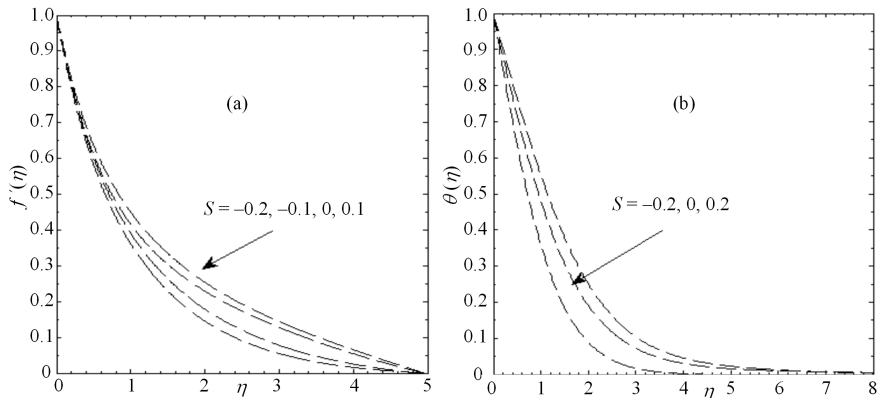


Fig. 3. Velocity (a) and temperature profiles (b) for different values of of blowing/suction parameter S and for (a) $M = 0.3$, $\beta = 0.2$, $k_1 = 0.1$, (b) $M = 0.3$, $k_1 = 0.1$, $N = 1$ and both (a) and (b) $\text{Pr} = 0.7$, $\gamma^* = \gamma = \text{Ec} = 0$

For large porosity of the medium, that is, for smaller values of k_1 (as the porosity of the medium increases, the value of k_1 decreases), the fluid has more space of flow, and, as a consequence, its velocity increases. However, this change in the velocity near the surface (its the maximum at far away from the surface) is small and finally approaches zero. Thus, an increase in the permeability parameter k_1 leads to decrease of the horizontal velocity profile, which enhances deceleration of the flow. An increase in the permeability parameter k_1 leads to an increase in skin friction and shear stress on the boundary whereas the boundary layer thickness and the absolute value of the temperature gradient at the surface decrease, as shown

later in detail. Thus, the heat transfer rate at the surface decreases with increasing k_1 . The presence of porous medium reduces the fluid velocity and enhances the temperature.

Figure 3(a) displays the effect of the suction/blowing parameter S on the velocity profiles. The fluid velocity is found to decrease with increasing values of the suction/blowing parameter S . That is, suction causes a decrease in the fluid velocity in the boundary layer region and, as consequence, a decrease in the wall shear stress. An increase in suction causes progressive thinning of the boundary layer. Figure 3(b) shows that the temperature in the boundary layer also decreases with increasing S ($S > 0$). This causes a decrease in the rate of heat transfer from the fluid to the sheet surface, while blowing ($S < 0$) exhibits an opposite trend. The thermal boundary layer is thinner in the case of suction ($S > 0$) as compared to the case of impermeability ($S = 0$) and thicker in the case of blowing ($S < 0$).

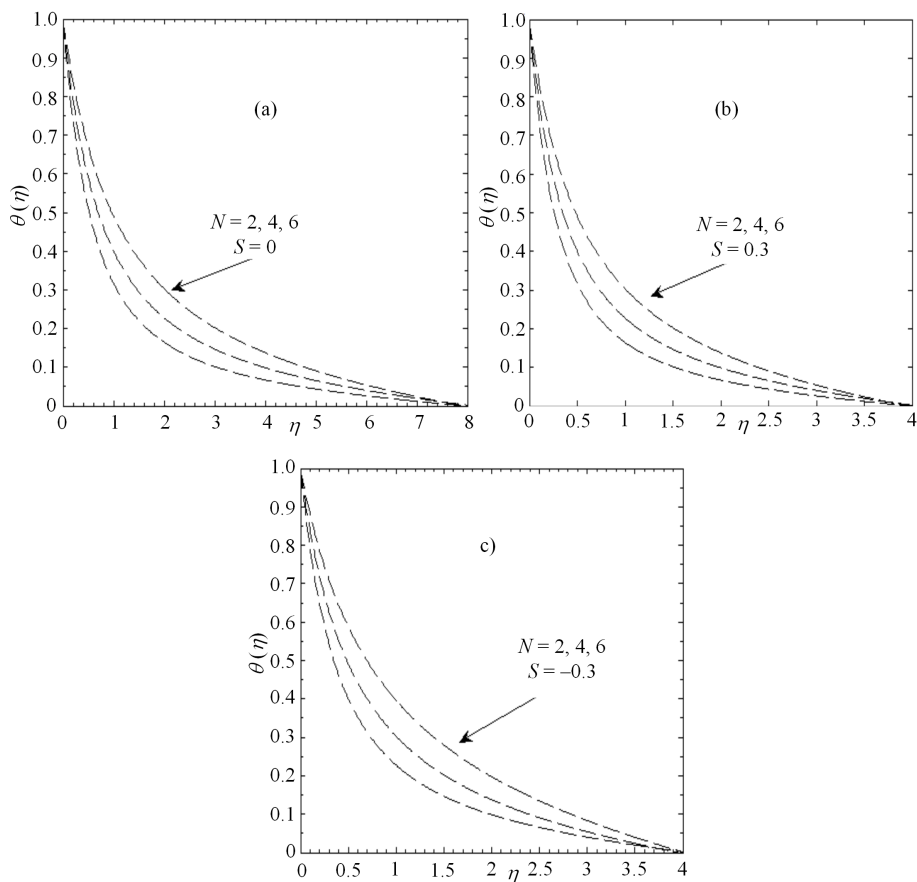


Fig. 4. Temperature profiles for $M = 0.3$, $\beta = 0.2$, $k_1 = 0.1$, $\text{Pr} = 0.7$ and different values of radiation parameter N ($\gamma = \gamma^* = \text{Ec} = 0$); (a) $S = 0$, (b) $S = 0.3$, (c) $S = -0.3$

Figure 4(a) gives the effect of the radiation parameter N on the temperature field. With increasing radiation parameter N , the temperature in the boundary layer decreases. Figures 4(b) and 4(c) exhibit the radiation effect on the temperature field in presence of suction and blowing. An increase in the radiation parameter means the release of heat energy from the flow region therefore the fluid temperature decreases because the thermal boundary layer becomes thinner.

Figures 5 and 6 illustrate the effect of temperature dependent heat absorption ($\gamma < 0$) or generation ($\gamma > 0$) parameter on the dimensionless temperature. It is shown that the effect of heat absorption causes a drop in the temperature, while the reverse effect is observed when $\gamma > 0$.

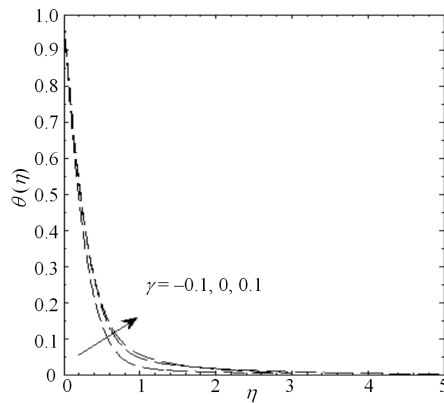


Fig. 5. Temperature profiles for $\beta = 0.1$, $k_1 = 0.1$, $S = 0.1$, $N = 1$, $\text{Pr} = 0.7$ with different values of γ ; $\gamma^* = \text{Ec} = 0$

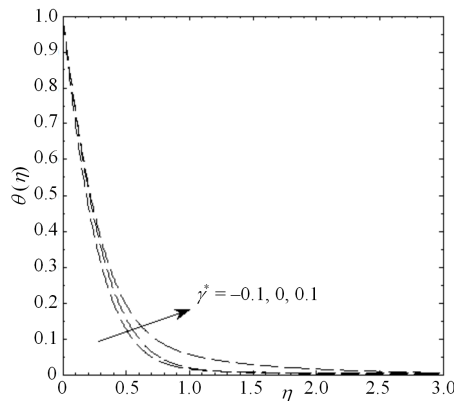


Fig. 6. Temperature profiles for $\beta = 0.1$, $k_1 = 0.1$, $S = 0.1$, $N = 1$, $\text{Pr} = 0.7$ with different values of γ^* ; $\gamma = \text{Ec} = 0$

The dimensionless temperature distribution within the boundary layer region for various values of Eckert number Ec are illustrated in Fig. 7. It can be seen that the

temperature increases as Ec increases. The increase in the fluid temperature due to frictional heating is observed to be more pronounced for higher value of Ec as expected.

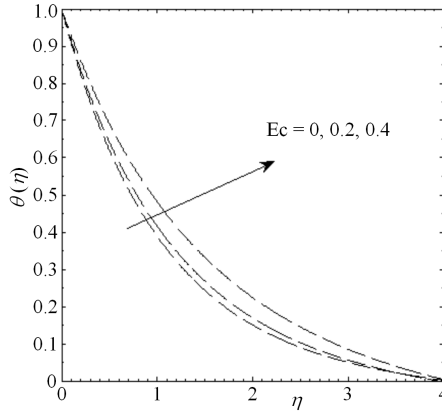


Fig. 7. Temperature profiles for $\beta = 0.1, k_1 = 0.1, S = 0.1, N = 1, Pr = 0.7$ with different values of $Ec; \gamma^* = \gamma = 0$

5. Conclusion

The results obtained are compared with some of earlier published results for selected limiting cases and listed in Tables 1 and 2.

Table 1. Values of $-f''(0)$ in a steady flow in the absence of the porous medium with no blowing/suction and $\gamma^* = \gamma = Ec = 0$, for different values of Maxwell parameter β

β	$-f''(0)$		
	Sadeghy et al. [24]	Abel et al. [25]	present paper
0	0.999962	0.999963	0.999960
0.2	1.051948	1.051949	1.051947
0.4	1.101856	1.401851	1.101847
0.6	1.150163	1.150162	1.150164
0.8	1.966920	1.196693	1.196694

Table 2. Value of $Nu_x Re_x^{-1/2}$ for $M = 0, \beta = 0, S = 0, k_1 = 0, N \rightarrow \infty$ and $\gamma^*; \gamma = Ec = 0$, for different values of Pr

Pr	$-\theta'(0)$		
	Abel et al. [25]	Mukhopadhyay et al. [27]	present paper
0.01	0.02942	0.02944	0.02945
0.72	1.08853	1.08855	1.08869
1.00	1.33334	1.33334	1.33335
3.00	2.50972	2.50971	2.50972

Here, Nu_x is the local Nusselt number and Re_x denotes the local Reynolds number. There holds: $Nu_x Re_x^{-1/2} = -1/(2 - \beta)$.

The values of $f''(0)$ for the steady flow of a viscous incompressible non-Newtonian Maxwell fluid in a non-porous medium for variable values of the Maxwell parameter β in the absence of the magnetic field are compared with the available results of Sadeghy et al. [24] and Abel et al. [25] (table 1). The results are found to be in a good agreement with the published results.

References

- [1] H. I. ANDERSSON, K. H. BECH, B. S. DANDAPT: *Magnetohydrodynamic flow of a power-law fluid over a stretching sheet*. International Journal of Non-Linear Mechanics 27 (1992), No. 6, 929–936.
- [2] I. A. HASSANIEN: *Flow and heat transfer on a continuous flat surface moving in a parallel free stream of power-law fluid*. Applied Mathematical Modelling 20 (1996), No. 10, 779–784.
- [3] K. SADEGHY, M. SHARIFI: *Local similarity solution for the flow of a "second-grade" viscoelastic fluid above a moving plate*. International Journal of Non-Linear Mechanics 39 (2004), No. 8, 1265–1273.
- [4] S. BANS, M. SALIH DOKUZ: *Three-dimensional stagnation point flow of a second grade fluid towards a moving plate*. International Journal of Engineering Science 44 (2006), Nos. 1–2, 49–58.
- [5] M. SAJID, I. AHMAD, T. HAYAT, M. AYUB: *Unsteady flow and heat transfer of a second grade fluid over a stretching sheet*. Communications in Nonlinear Science and Numerical Simulation 14 (2009), No. 1, 96–108.
- [6] M. M. HEYHAT, N. KHABAZI: *Non-isothermal flow of Maxwell fluids above fixed flat plates under the influence of a transverse magnetic field*. Proceedings of the Institution of Mechanical Engineers, Part C: Journal of Mechanical Engineering Science 225 (2011), No. 4, 909–916.
- [7] C. H. JOHNSON, P. CHENG: *Possible similarity solutions for free convection boundary layers adjacent to flat plates in porous media*. International Journal of Heat and Mass Transfer 21 (1978), No. 6, 709–718.
- [8] C. H. CHEN: *Combined heat and mass transfer in MHD free convection from a vertical surface with Ohmic heating and viscous dissipation*. International Journal of Engineering Science 42 (2004), No. 7, 699–713.
- [9] D. PAL, P. S. HIREMATH: *Computational modeling of heat transfer over an unsteady stretching surface embedded in a porous medium*. Meccanica 45 (2010), No. 3, 415–424.
- [10] K. VAJRVELU, A. HADJINICOLAOU: *Heat transfer in a viscous fluid over a stretching sheet with viscous dissipation and internal heat generation*. International Communications in Heat and Mass Transfer 20 (1993), No. 3, 417–430.
- [11] P. H. VEENA, M. SUBHASH-ABEL, K. RAJAGOPAL, V. K. PRAVIN: *Heat transfer in a visco-elastic fluid past a stretching sheet with viscous dissipation and internal heat generation*. Zeitschrift für Angewandte Mathematik und Physik ZAMP 57 (2006), No. 3, 447–463.
- [12] A. J. CHUMKHA, A. A. KHALED: *Similarity solutions for hydromagnetic simultaneous heat and mass transfer by natural convection from an inclined plate with internal heat generation or absorption*. Heat and Mass Transfer 37 (2001), Nos. 2–3, 117–123.
- [13] R. C. BATALLER: *Viscoelastic fluid flow and heat transfer over a stretching sheet under the effects of a non-uniform heat source, viscous dissipation and thermal radiation*. International Journal of Heat and Mass Transfer 50 (2007), Nos. 15–16, 3152–3162.
- [14] M. S. ABEL, P. G. SIDDHESHWAR, N. MAHESHA: *Effects of thermal buoyancy and variable thermal conductivity on the MHD flow and heat transfer in a power-law fluid*

- past a vertical stretching sheet in the presence of a non-uniform heat source.* International Journal of Non-Linear Mechanics *44* (2009), No. 1, 1–12.
- [15] M. M. NANDEPPANAVEAR, M. S. ABEL, J. JAWADE: *Heat transfer in a Walter's liquid B fluid over an impermeable stretching sheet with non-uniform heat source/sink and elastic deformation.* Communications in Nonlinear Science and Numerical Simulation *15* (2010), No. 7, 1791–1802.
- [16] D. PAL, H. MONDAL: *Effect of variable viscosity on MHD non-Darcy mixed convective heat transfer over a stretching sheet embedded in a porous medium with non-uniform heat source/sink.* Communications in Nonlinear Science and Numerical Simulation *15* (2010), No. 6, 1553–1564.
- [17] MUSTAFA A. A. MAHMOUD, AHMED M. MEGAHED: *Non-uniform heat generation effect on heat transfer of a non-Newtonian power-law fluid over a non-linearly stretching sheet.* Meccanica *47* (2012), No. 5, 1131–1139.
- [18] A. RAPTIS: *Flow of a micropolar fluid past a continuously moving plate by the presence of radiation.* International Journal of Heat and Mass Transfer *41* (1998), No. 18, 2865–2866.
- [19] A. RAPTIS: *Radiation and viscoelastic flow.* International Communications in Heat and Mass Transfer *26* (1999), No. 6, 889–895.
- [20] A. RAPTIS, C. PERDIKIS, H. S. TAKHAR: *Effect of thermal radiation on MHD flow.* Applied Mathematics and Computation *153* (2004), No. 3, 645–649.
- [21] MOSTAFA A. A. MAHMOUD: *Thermal radiation effects on MHD flow of a micropolar fluid over a stretching surface with variable thermal conductivity.* Physica A: Statistical Mechanics and its Applications *375* (2007), No. 2, 401–410.
- [22] M. S. ABEL, M. NARAYANA: *Heat transfer in MHD viscoelastic fluid flow over a stretching sheet with variable thermal conductivity, non-uniform heat source and radiation.* Applied Mathematical Modelling *32* (2008), No. 10, 1965–1983.
- [23] S. MUKHOPADHYAY: *Effect of thermal radiation on unsteady mixed convection flow and heat transfer over a porous stretching surface in porous medium.* International Journal of Heat and Mass Transfer *52* (2009), Nos. 13–14, 3261–3265.
- [24] K. SADEGHY, H. HAJIBEYGI, S. M. TAGHAVI: *Stagnation-point flow of upper-convected Maxwell fluid.* International Journal of Non-Linear Mechanics *41* (2006), No. 10, 1242–1247.
- [25] M. S. ABEL, J. V. TAWADE, M. M. NANDEPPANAVAR: *MHD flow and heat transfer for the upper-convected Maxwell fluid over a stretching sheet.* Meccanica *47* (2012), No. 2, 385–393.
- [26] S. MUKHOPADHYAY, P. RANJAN, G. C. LAYEK: *Heat transfer characteristics for the Maxwell fluid flow past an unsteady stretching permeable surface embedded in a porous medium with thermal radiation.* Journal of Applied Mechanics and Technical Physics *54* (2013), No. 3, 385–396.

Received April 17, 2018

Exact solutions of blood flow obeying Bingham plastic model through a tapered artery¹

SUBRATA MUKHOPADHYAY², SWATI MUKHOPADHYAY^{3,3}

Abstract. Blood flow in a narrow, tapered and stenosed artery has been investigated. The non-Newtonian character of blood in small arteries at low shear rates is analyzed mathematically by considering the blood as a Bingham plastic fluid. Bingham plastic fluid is a type of generalized Newtonian fluid which exhibits yield stress. Flow of blood is considered to be steady, laminar, incompressible and axi-symmetric. The effects of tapering, shape and height of stenosis on blood flow have been investigated through the presentation of axial velocity, wall shear stress and resistance to flow. Comparisons are made with the available results for Newtonian flow. It is noted that the wall shear stress and the resistance to flow increase with the increasing size of stenosis and are higher than those of Newtonian fluid flow.

Key words. Bingham plastic fluid, steady flow, tapered artery, stenosis, wall shear stress, resistance to flow.

1. Introduction

Atherosclerosis, a common arterial disease, is considered as one of the leading causes of human mortality in the modern industrialized world. In case of such disease fatty substances like cholesterol, lipid, etc. are deposited in the arterial lumen and thickens the arterial wall. This type of abnormal internal growth in the arterial lumen is known as stenosis. Due to the formation of stenosis, the arterial lumen becomes typically narrowed and the wall becomes stiff. In some cases the arterial wall remodels itself by increasing its internal radius to accommodate a plaque without narrowing its lumen. This is not possible in most of the cases. As a result,

¹One of the authors (S. M.) acknowledges the financial support received from CSIR, New Delhi, India through Major Research Project 25(0244)/15/EMR-II.

²Department of Mathematics, Krishnagar Govt. College, Krishnagar, Nadia, W. B., India

³Department of Mathematics, The University of Burdwan, Burdwan-713104, W. B., India

⁴Corresponding author; e-mail: swati_bumath@yahoo.co.in

stenosis significantly alters the normal flow of blood, causing malfunction of the cardiovascular system. This ultimately results in the cardiac arrest [1, 2]. The ability of describing the flow through a stenosed tube can provide the possibility of diagnosing the disease in its earlier stages and can be used as a basis of surgical intervention.

The exact causes and mechanisms responsible for the initiation of plaque deposition in the arterial wall and formation of stenosis are not known clearly. But it has already been established that once a mild stenosis is developed, the resulting flow disturbances influences the development of the disease significantly and changes the regional blood flow characteristics [3–5]. Blood behaves like a Newtonian fluid during its flow through larger arteries at high shear rates [6]. On the other hand, it behaves like a non-Newtonian fluid during its flow through smaller arteries at low rates of shear $\dot{\gamma}$ (s^{-1}) [7]. In the past few decades several experimental and theoretical research works have been done on this particular area [8–12]. To study the blood flow in stenosed arteries using Newtonian/non-Newtonian fluid models several attempts can be found in [13–17]. Mostly the coronary arteries are of diameter less than 0.5 mm. So, for accurate prediction blood must be modeled as non-Newtonian fluid in such arteries. In most of the investigations, the flow is considered through cylindrical pipes of uniform cross section. But it is well known that the blood vessels bifurcate at frequent intervals and the radius of the vessels may vary with the distance [18]. Hence, the effects of vessel tapering deserves special attention. Moreover, the non-Newtonian behavior of the streaming blood in arteries having small diameter should be taken into account.

Motivated by this, an attempt is made in the present theoretical investigation to develop a mathematical model in studying the significant characteristics of the non-Newtonian blood flow through a tapered narrow artery having a mild stenosis. Experiments conducted on blood reveal that blood has a finite yield stress of 0.04 dynes/cm² at 40% hematocrit. The yield stress of blood changes during various pathological situations and diseased conditions. The effect of yield stress has been found to be significant when blood flows in vessels of smaller diameters (less than 0.5 mm). Bingham plastic exhibits shear dependent viscosity and a finite yield stress before the starting of the flow. Hence to accommodate the yield stress property in the present study, Bingham plastic fluid model has been used to characterize the non-Newtonian behavior of the streaming blood. The velocity profile for Bingham plastic is blunted from the parabolic profile in the core region and exhibits plug flow which is consistent with the flow behavior in smaller arteries [19]. With view of these properties Bingham plastic presents a good model for blood. The existence and uniqueness as well as the stability characteristics of such flow problems have been established by Malek et al. [20, 21]. In view of those studies, the existence of the flow characterized by the Bingham plastic fluid model is not investigated in the present article. Attention is only paid to finding the analytical solutions of the governing equations. The expression for axial velocity, resistance to flow, wall shear stress and shear stress at the throat of the stenosis have been obtained. The flow behavior in case of different types of tapering (see Fig. 1) has also been explained graphically.

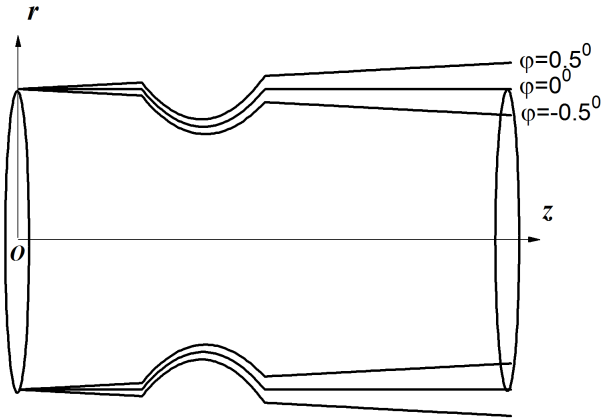


Fig. 1. Schematic diagram of the stenosed ($n = 2$) and tapered artery

2. Formulation of the problem

Let us consider a steady, laminar, incompressible and axi-symmetric flow of blood in a narrow tapered artery with a mild axi-symmetric stenosis in its lumen. It is assumed that the segment of the artery under consideration is axi-symmetric and straight. Consider the cylindrical polar co-ordinates (r, θ, z) where $r = 0$ gives the axis of the artery.

The geometry of the stenosed tapered arterial segment may be described as

$$R(z) = \begin{cases} (R_0 + \xi z) [1 - \eta \{b^{n-1} (z - a) - (z - a)^n\}], & a \leq z \leq a + b, \\ (R_0 + \xi z), & 0 \leq z \leq a \text{ or } a + b \leq z \leq L, \end{cases} \tag{1}$$

where $R(z)$ and R_0 are the radii of the tapered artery at a distance z and at $z = 0$, respectively, ξ is the tapering parameter, b is the length of the stenosis, $n (\geq 2)$ is a parameter which determines the shape of the stenosis (the symmetric stenosis occurs for $n = 2$), a indicates the starting point of the stenosis and L is the length of the arterial segment under consideration. The parameter η is defined by

$$\eta = \frac{\delta n^{\frac{n}{n-1}}}{R_0 b^n (n - 1)}, \tag{2}$$

in which δ denotes the maximum height of the stenosis situated at

$$z = a + \frac{b}{n^{\frac{1}{n-1}}}. \tag{3}$$

Here φ is the tapering angle given by $\xi = \tan \varphi$. For converging tapering $\varphi < 0$, $\varphi = 0$ for non-tapered artery and for diverging tapering $\varphi > 0$.

2.1. Governing equations

The equations governing the steady, laminar, incompressible flow of blood are given by

$$\frac{\partial u}{\partial r} + \frac{u}{r} + \frac{\partial w}{\partial z} = 0, \quad (4)$$

$$\rho \left(u \frac{\partial}{\partial r} + w \frac{\partial}{\partial z} \right) u = -\frac{\partial p}{\partial r} + \frac{1}{r} \frac{\partial}{\partial r} (r\tau_{rr}) + \frac{\partial}{\partial z} (\tau_{rz}) - \frac{\tau_{\theta\theta}}{r}, \quad (5)$$

$$\rho \left(u \frac{\partial}{\partial r} + w \frac{\partial}{\partial z} \right) w = -\frac{\partial p}{\partial z} + \frac{1}{r} \frac{\partial}{\partial r} (r\tau_{rz}) + \frac{\partial}{\partial z} (\tau_{zz}), \quad (6)$$

where u and w are the velocity of the flowing blood in the radial and axial directions respectively, p is the pressure, ρ is the density of blood, and τ 's are the components of the stress tensor.

When the radius of the lumen is small, the radial velocity is negligibly small and can be neglected for a low Reynolds number flow [22]. In that case equations (2), (3) and (4) reduce to

$$\frac{\partial w}{\partial z} = 0, \quad (7)$$

$$\frac{\partial p}{\partial r} = 0, \quad (8)$$

$$-\frac{\partial p}{\partial z} + \frac{1}{r} \frac{\partial}{\partial r} (r\tau_{rz}) = 0. \quad (9)$$

2.2. Constitutive equations

Here, the streaming blood has been regarded as a non-Newtonian fluid obeying Bingham plastic fluid model. The constitutive equation for such model is given by

$$-\frac{dw}{dr} = \begin{cases} \frac{\tau - \tau_0}{\mu}, & \tau \geq \tau_0. \\ 0, & \tau < \tau_0, \end{cases} \quad (10)$$

where $\tau = |\tau_{rz}| = -\tau_{rz}$, τ_0 is the yield stress and μ is the viscosity of the flowing blood assumed to be constant.

3. Boundary conditions

The no-slip boundary condition on the arterial wall is imposed as

$$w = 0 \text{ at } r = R(z), \quad 0 \leq z \leq L, \quad (11)$$

If R_p is the plug flow radius, then

$$\frac{\partial w}{\partial r} = 0 \text{ at } 0 \leq r \leq R_p. \tag{12}$$

4. Method of solution

From (7) and (8), it is easily obtained that w is a function of r only, i.e., $w = w(r)$ and p is a function of z only, i.e., $p = p(z)$. Since at $r = 0$ τ_{rz} is finite and $\tau = |\tau_{rz}| = -\tau_{rz}$, from (9), we get

$$\tau = -\frac{r}{2} \frac{dp}{dz}. \tag{13}$$

From (10), we can write

$$\tau_0 - \mu \frac{dw}{dr} = -\frac{r}{2} \frac{dp}{dz}. \tag{14}$$

Using the boundary condition (12), the plug-flow radius is obtained as

$$R_p = -\frac{2\tau_0}{\frac{dp}{dz}}. \tag{15}$$

Now the volume rate of flow across any cross section is given by

$$Q = \int_0^{R_p} 2\pi r w_p dr + \int_{R_p}^R 2\pi r w dr$$

where w_p is the plug flow velocity.

Using the boundary condition (11), we have

$$Q = -\pi \int_{R_p}^R \frac{dw}{dr} r^2 dr. \tag{16}$$

Let τ_w be the wall shear stress. Then from (13) we get

$$\tau_w = -\frac{R}{2} \frac{dp}{dz}. \tag{17}$$

From (13) and (17) we have

$$r = \frac{\tau R}{\tau_w}. \tag{18}$$

Using (10) and (18) in (16) we have

$$Q = \pi \int_{\tau_0}^{\tau_w} \frac{\tau - \tau_0}{\mu} \frac{\tau^2 R^2}{\tau_w^2} \frac{R}{\tau_w} d\tau = \frac{\pi R^3}{\mu \tau_w^3} \left(\frac{\tau_w^4}{4} - \tau_0 \frac{\tau_w^3}{3} + \frac{\tau_0^4}{12} \right) \cong$$

$$\cong \frac{\pi R^3}{\mu} \left(\frac{\tau_w}{4} - \frac{\tau_0}{3} \right) \quad (19)$$

This gives the expression for wall shear stress as

$$\tau_w = 4 \left[\frac{\mu Q}{\pi R^3} + \frac{\tau_0}{3} \right]. \quad (20)$$

Putting this result into (17), we get the expression for the pressure gradient as

$$\frac{dp}{dz} = -\frac{8}{R} \left[\frac{\mu Q}{\pi R^3} + \frac{\tau_0}{3} \right]. \quad (21)$$

Now integrating (14) and using the boundary condition (11) we get the expression for the axial velocity as

$$w = -\frac{1}{\mu} \left[\frac{1}{4} (R^2 - r^2) \frac{dp}{dz} + \tau_0 (R - r) \right], \quad R_p \leq r \leq R \quad (22)$$

and the plug flow velocity is obtained as

$$w_p = -\frac{1}{\mu} \left[\frac{1}{4} (R^2 - R_p^2) \frac{dp}{dz} + \tau_0 (R - R_p) \right], \quad 0 \leq r \leq R_p. \quad (23)$$

The average velocity of flow can be calculated as

$$\begin{aligned} \bar{w} &= \frac{2\pi \int_0^R wr \, dr}{\pi R^2} = \frac{2}{R^2} \left[\int_0^{R_p} wr \, dr + \int_{R_p}^R wr \, dr \right] = \\ &= -\frac{2}{R^2} \left[\frac{1}{16\mu} (R^4 - R_p^4) \frac{dp}{dz} + \frac{\tau_0}{6\mu} (R^3 - R_p^3) \right]. \end{aligned} \quad (24)$$

Let $p = p_0$ at $z = 0$ and $p = p_1$ at $z = L$. Then integrating (21), we get the pressure drop as

$$p_0 - p_1 = 8 \left[\frac{\mu Q}{\pi} \int_0^L R^{-4} \, dz + \frac{\tau_0}{3} \int_0^L R^{-1} \, dz \right].$$

Thus the flow resistance is obtained as

$$\lambda = \frac{p_0 - p_1}{Q} = 8 \left[\frac{\mu}{\pi} \int_0^L R^{-4} \, dz + \frac{\tau_0}{3Q} \int_0^L R^{-1} \, dz \right], \quad (25)$$

which can be evaluated numerically.

Putting $\tau_0 = 0$ in (20), (21), (22) and (24), the corresponding expressions for a

Newtonian fluid [23] can be obtained as

$$\tau_w = \frac{4\mu Q}{\pi R^3}, \tag{26}$$

$$\frac{dp}{dz} = -\frac{8\mu Q}{\pi R^4}, \tag{27}$$

$$w = -\frac{1}{4\mu} (R^2 - r^2) \frac{dp}{dz}, \quad 0 \leq r \leq R, \tag{28}$$

$$\bar{w} = -\frac{R^2}{8\mu} \frac{dp}{dz}. \tag{29}$$

5. Results and discussion

For the purpose of numerical computations of the quantities of major physiological significance, the values of the following parameter have been taken: $R_0 = 0.2$ cm, $L = 4$ cm, $a = 1$ cm, $b = 1$ cm, $\mu = 0.04$ dyne-s/cm², $Q = 2.4$ cm³/s, $\tau_0 = 0.04$ dyne/cm². To observe the quantitative effects of n , δ and φ , the results of numerical computations are presented in Figs. 2–9.

The pressure gradient in the artery is presented in Figs. 2 and 3.

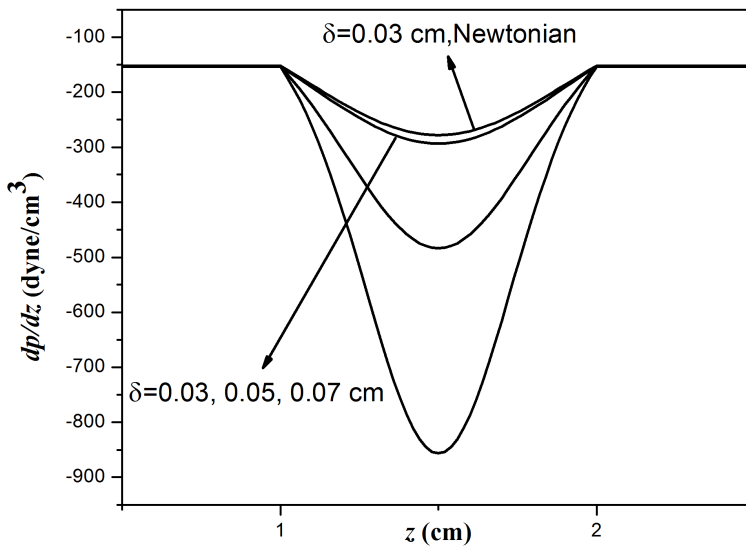


Fig. 2. Pressure gradient along the stenosed ($n = 2$) artery for $\varphi = 0^\circ$

A rapid fall in pressure gradient (noted as the constriction) is approached. Pressure gradient recovers its value after the constriction. From the figures it can be seen that the pressure gradient (in magnitude) is stronger at the stenosis zone and

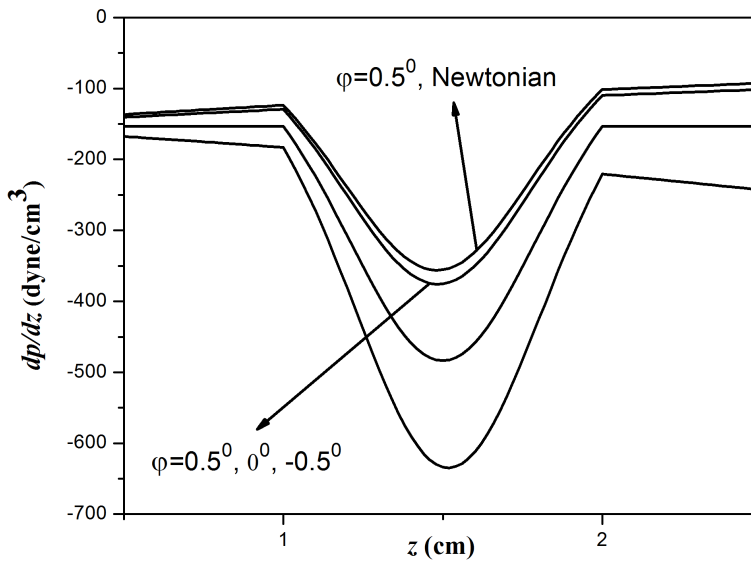


Fig. 3. Pressure gradient along the stenosed ($n = 2$) artery for $\delta = 0.05$ cm

particularly at the throat of the stenosis. Moreover, pressure gradient is found to decrease with the increasing height of the stenosis or with the decrease of the tapering angle. The low pressure region gives rise to a health complication as the vessel wall may collapse due to low pressure. Also, it is noted that the pressure gradient (in magnitude) is stronger in case of Bingham plastic fluid compared to Newtonian fluid. Due to the presence of yield stress in Bingham plastic fluid, more pressure gradient is required to maintain the same flow rate.

Figures 4 and 5 present the velocity field at the throat of the stenosis. It is found that the velocity is symmetrically distributed over the stenosis region about a fixed point where the height of the stenosis is maximum. So, flow rate along the artery increases or decreases as the cross section of the artery decreases or increases. With the increasing height of the stenosis or decreasing values of the tapering angle, the lumen area gets contracted. As a result, to maintain a constant flow rate, the velocity of the fluid increases. The position of maximum velocity corresponds to the lowest pressure. Also, it is found that due to the absence of yield stress in Newtonian fluid, the velocity in case of Newtonian fluid is larger than that of Bingham plastic fluid. This can be stated as the velocity decreases with the increase of yield stress. This is complete agreement with the results available in open literature.

Wall shear stress plays an important role in the initiation of the disease. High wall shear stress is believed to damage the vessel wall and is the cause of initial thickening. On the other hand, it is known that plaque is formed in the region of low shear stress. So wall shear stress deserves a special attention. Variations of wall shear stress are exhibited in Figs. 6 and 7. It is observed that with the increasing height of the stenosis or decreasing values of the tapering angle, the wall shear stress increases.

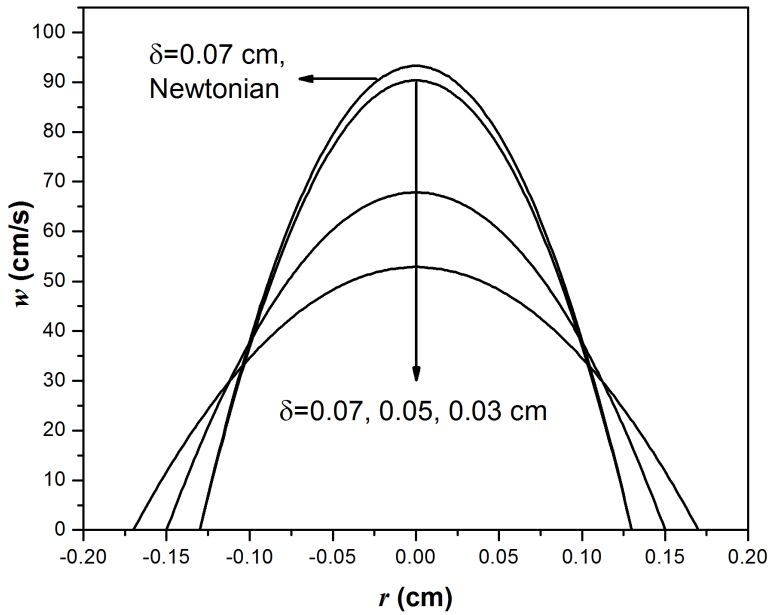


Fig. 4. Axial velocity profile at $z = 1.5$ cm for $(n = 2)$ and $\varphi = 0^\circ$

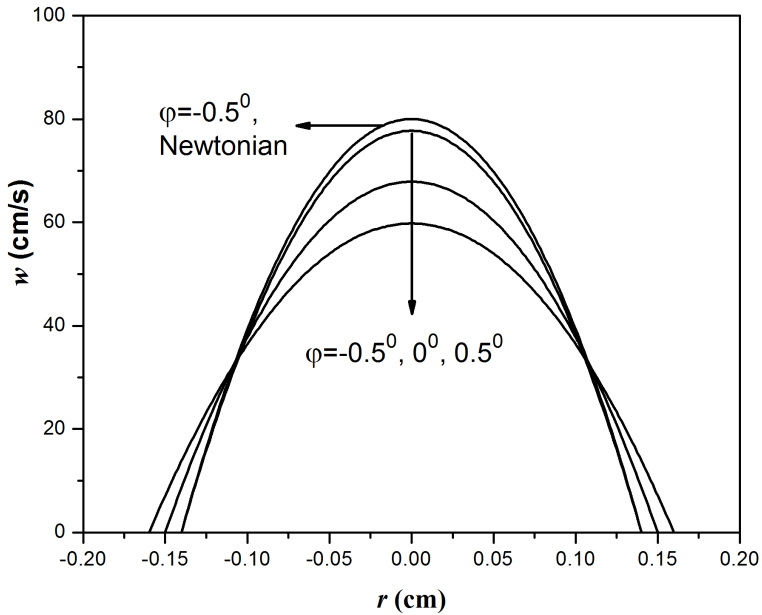


Fig. 5. Axial velocity profile at $z = 1.5$ cm for $n = 2$ and $\delta = 0.05$ cm

The figures also reveal that the wall shear stress is significantly higher at the stenosis zone and highest wall shear stress (peak value) is found at the throat of

the stenosis. This agrees qualitatively well with the results of Srivastava [24] who considered the Couple stress fluid representing blood.

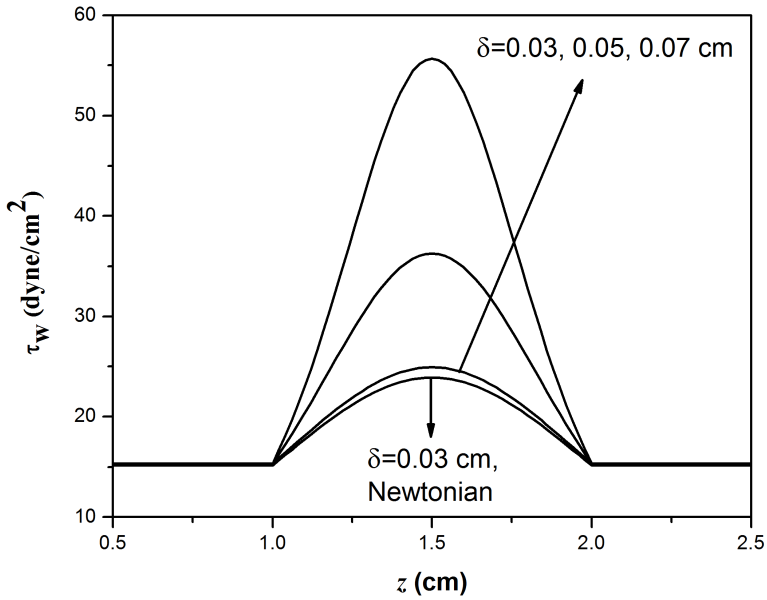


Fig. 6. Variation of wall shear stress for $(n = 2)$ and $\varphi = 0^\circ$

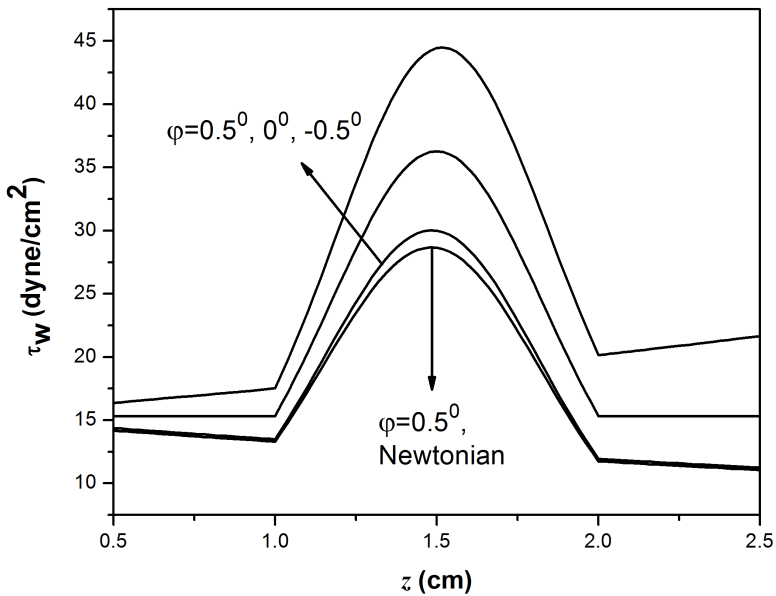


Fig. 7. Variation of wall shear stress for $n = 2$ and $\delta = 0.05$ cm

Peaks of wall shear stress are clinically relevant as it causes to damage the endothelial cells and aggregation of platelets. It is noted that the rate of increase of the wall shear stress with respect to the height of the stenosis increases, i.e., wall shear stress increases with the severity of the stenosis which appears to be reasonable from the medical point of view. Due to the absence of yield stress in Newtonian fluid, the wall shear stress in case of Newtonian fluid is weaker than that of Bingham plastic fluid. Wall shear stress developed in the constricted portion of the artery gets the shape of a symmetric curve only for $n = 2$ and $\varphi = 0$. This agrees well with the results of Chakravarty and Datta [17]. Such symmetry disappears as the tapering angle φ changes or the shape parameter n changes.

Figures 8 and 9 reveal the effects of various parameters on the flow resistance. It can be seen that the flow resistance increases with the height of the stenosis and rate of increase of the flow resistance with respect to the height of the stenosis increases, i.e., flow resistance increases with the severity of the stenosis which seems to be reasonable from the clinical point of view. The flow resistance increases from diverging to converging tapering. Flow resistance is maximum for a symmetric stenosis. This agrees well with the results of Chakravarty and Datta [17]. Due to the absence of yield stress in Newtonian fluid, the flow resistance in case of Newtonian fluid is less than that of Bingham plastic fluid. It is interesting to note that the flow resistance is maximum in case of symmetric stenosis.

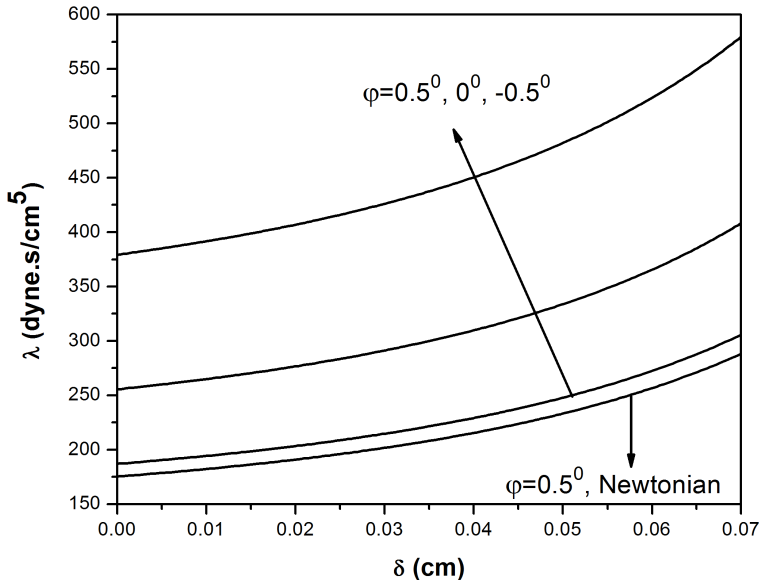


Fig. 8. Variation of flow resistance with stenosis height for $n = 2$

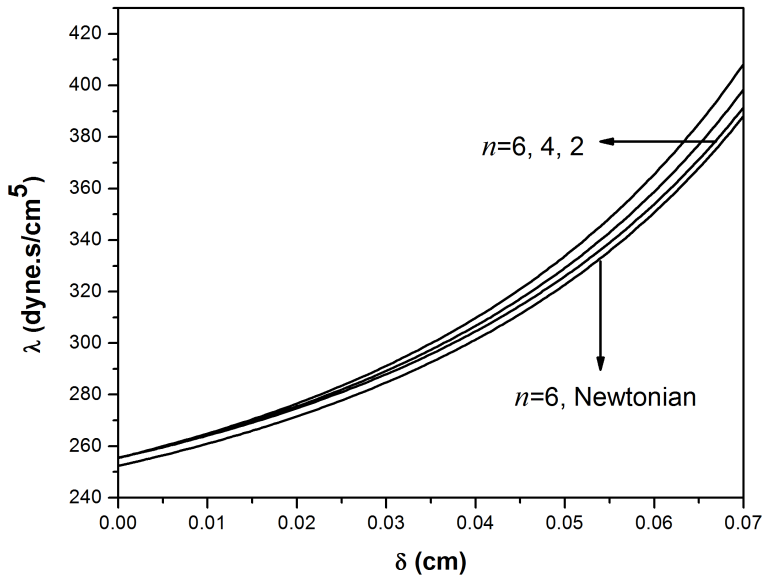


Fig. 9. Variation of flow resistance with stenosis height for $\varphi = 0^\circ$

6. Conclusion

Blood flow is analyzed in a narrow tapered stenosed artery using the Bingham plastic fluid model. The main findings are listed as follows:

1. It is observed that for a constant flow rate, the velocity field increases with the decrease of tapering angle or with the increase in height of the stenosis. Hence due to narrowing of the arterial lumen the velocity field increases.
2. It is found that for a constant flow rate, the wall shear stress increases if the tapering angle decreases or the height of the stenosis increases. Thus due to narrowing of the blood vessel the wall shear stress increases.
3. For any shape of stenosis, the wall shear stress is maximum at the throat of the stenosis. Maximum wall shear stress is observed for converging tapered artery.
4. For a constant flow rate, the flow resistance increases if the tapering angle decreases or the height of the stenosis increases. Hence due to reduction in area of the arterial lumen the resistance to flow increases.
5. The flow resistance becomes maximum for a symmetric stenosis.

References

- [1] M. J. DAVIES, A. THOMAS: *Plaque fissuring - the cause of acute myocardial infarction, sudden ischaemic death, and crescendo angina*. British Heart Journal 53 (1985), No. 4, 363-373.
- [2] S. GLAGOV, E. WEISENBERG, C. K. ZARINS, R. STANKUNAVICIUS, G. J. KOLETTIS:

- Compensatory enlargement of human atherosclerotic coronary arteries.* New England Journal of Medicine 316 (1987), No. 22, 1371–1375.
- [3] O. SMEDBY: *Do plaques grow upstream or downstream?: An angiographic study in the femoral artery.* Arteriosclerosis, Thrombosis, and Vascular Biology - AHA Journals 17 (1997), No. 5, 912–918.
 - [4] D. LIEPSCH: *An introduction to biofluid mechanics—basic models and applications.* Journal of Biomechanics 35 (2002), No. 4, 415–435.
 - [5] A. VALENCIA, M. VILLANUEVA: *Unsteady flow and mass transfer in models of stenotic arteries considering fluid-structure interaction.* International Communications in Heat and Mass Transfer 33 (2006), No. 8, 966–975.
 - [6] C. TU, M. DEVILLE: *Pulsatile flow of non-Newtonian fluids through arterial stenoses.* Journal of Biomechanics 29 (1996), No. 7, 899–908.
 - [7] S. CHIEN: *Hemorheology in clinical medicine.* Clinical Hemorheology and Microcirculation 2 (1982), Nos. 1–2, 137–142.
 - [8] P. CHATURANI, R. P. SAMY: *A study of non-Newtonian aspects of blood flow through stenosed arteries and its applications in arterial diseases.* Biorheology 22 (1985), No. 6, 521–531.
 - [9] C. E. HUCKABA, A. W. HAHN: *A generalized approach to the modeling of arterial blood flow.* Bulletin of Mathematical Biophysics 30 (1968), No. 4, 645–662.
 - [10] J. B. SHUKLA, R. S. PARIHAR, B. R. P. RAO: *Effects of stenosis on non-newtonian flow of the blood in an artery.* Bulletin of Mathematical Biology 42 (1980), No. 3, 283–294.
 - [11] S. CHAKRAVARTY: *Effects of stenosis on the flow-behaviour of blood in an artery.* International Journal of Engineering Science 25 (1987), No. 8, 1003–1016.
 - [12] J. C. MISRA, M. K. PATRA, S. C. MISRA: *A non-Newtonian fluid model for blood flow through arteries under stenotic conditions.* Journal of Biomechanics 26 (1993), No. 9, 1129–1141.
 - [13] SARIFUDDIN, S. CHAKRAVARTY, P. K. MANDAL: *Numerical simulation of Casson fluid flow through differently shaped arterial stenoses.* Zeitschrift für angewandte Mathematik und Physik 65 (2014), No. 4, 767–782.
 - [14] G. THEODOROU, D. BELLET: *Laminar flows of a non-newtonian fluid in mild stenosis.* Computer Methods in Applied Mechanics and Engineering 54 (1986), No. 1, 111–123.
 - [15] P. K. MANDAL: *An unsteady analysis of non-Newtonian blood flow through tapered arteries with a stenosis.* International Journal of Non-Linear Mechanics 40 (2005), No. 1, 151–164.
 - [16] S. CHAKRAVARTY, P. K. MANDAL: *Two-dimensional blood flow through tapered arteries under stenotic conditions.* International Journal of Non-Linear Mechanics 35 (2000), No. 5, 779–793.
 - [17] S. CHAKRAVARTY, A. DATTA: *Dynamic response of arterial blood flow in the presence of multi-stenoses.* Mathematical and Computer Modelling 13 (1990), No. 11, 37–55.
 - [18] R. L. WHITEMORE: *Rheology of circulation.* Publisher: Pergamon Press, Oxford (1968).
 - [19] G. BUGLIARELL, J. SEVILLA: *Velocity distribution and other characteristics of steady and pulsatile blood flow in fine glass tubes.* Biorheology 7 (1970), No. 2, 85–107.
 - [20] J. MALEK, J. NECAS, M. ROKYTA, M. RUZICKA: *Weak and measure-valued solutions to evolutionary PDEs.* CRC Press, Chapman & Hall, New York (1996).
 - [21] J. MALEK, K. R. RAJAGOPAL, M. RUZICKA: *Existence and regularity of solutions and the stability of the rest state for fluids with shear dependent viscosity.* Mathematical Models and Methods in Applied Sciences 5 (1995), No. 6, 789–812.
 - [22] D. S. SANKAR, A. I. MD. ISMAIL: *Two-fluid mathematical models for blood flow in stenosed arteries: A comparative study.* Boundary Value Problems, Springer Nature (2009), p. 568657.
 - [23] J. L. BANSAL: *Viscous fluid dynamics.* Publisher: Oxford & IBH Publishing Company (1992), 74–76.

- [24] L. M. SRIVASTAVA: *Flow of couple stress fluid through stenotic blood vessels*. Journal of Biomechanics 18 (1985), No. 7, 479–485.

Received September 13, 2018

Analysis of time-varying harmonic distortion related to induction motor operation

MARINA RASHEVSKAYA¹, SERGEY YANCHENKO¹

Abstract. Existing standards covering the issues of electromagnetic compatibility related to induction motors' operation are miscellaneous and may be confusing. Penetration of variable frequency drives and soft starters requires the development of standards and techniques assessing non-stationary harmonic performance of induction motors. This paper studies the standards defining harmonic emission limits within adjustable speed drive systems. Exemplarily, for the soft-starter of induction motor the estimation of non-stationary harmonic levels is produced by some popular techniques and their performance is analyzed.

Key words. Harmonics, induction motors, non-stationary distortion levels, soft-starter.

1. Introduction

Electromagnetic compatibility (EMC) is the ability of an equipment or system to function satisfactorily in its electromagnetic environment without introducing intolerable electromagnetic disturbances to anything in that environment [1].

The assessment of EMC featured by certain electrical device often presents a challenging task, implying the study of numerous standards and manuals. Current paper, exemplarily, studies the EMC standards covering the operation of induction motors (IM) [2–4] and, eventually, demonstrates a need for restructuring the present various standards related to IMs. Furthermore, a unified document covering all aspects of providing EMC of IMs should be developed. This particularly applies to the operation of variable-frequency drives (VFD) and soft starters that are well known for high levels of harmonic distortion of the voltage supplied to regulated IM. Moreover, proliferation of this equipment in industrial power grids results in additional harmonic problems in the supply network.

¹Power Engineering Institute, Department of Electric Power Supply and Electric Technology, Krasnokazarmennaya street 17, 111250, Moscow, Russia

2. Harmonic and interharmonic emission related to induction motors

According to the IEC 61000-2-12 [5] interharmonics are the spectral components of the waveform that are not multiples of the grid fundamental frequency. These can reveal themselves as separate or grouped spectral components. The voltage (current) waveform containing these components is called interharmonic.

Induction motors can give rise to interharmonic emission, so called slot harmonics, originating from the slots in the stator or rotor iron cores under conditions of saturation [6, 7]. In the steady-state constant speed operating mode interharmonics usually belong to the low frequency range of 500–2000 Hz that can be expanded under starting or accelerating conditions. Interharmonics can also originate from the natural asymmetry inherent to motor design (e.g., deviations from designed dimensions, air gap eccentricity, etc.).

Effects of current and voltage distortion associated with IMs, are aggravated in case of VFDs and soft starters [8]. The increase of current RMS values induced by additional harmonic currents combined with the growth of frequency-dependent resistive impedance may lead to conductor overheating, reduction of the power factor and equipment's efficiency, malfunction of circuit breakers and oversizing of power generators. Negative effects for transformers include additional losses related to hysteresis, eddy currents in the core and windings; and, consequently, reduction of isolation life span. Similarly, average cable durability reduces as a result of increased leakage currents [9].

2.1. Harmonic distortion of adjustable speed drives

Harmonic issues related to speed regulating equipment (including VFDs and soft-starters) can be assessed for the input and output terminals of equipment. Harmonic levels injected at the input terminals in supplying grid should comply with emission limits provided in IEC 61000-3-2 [2] and IEC 61000-3-4 [3]. Herewith, steady-state distortion of speed regulating equipment (see Fig. 1) is usually limited.

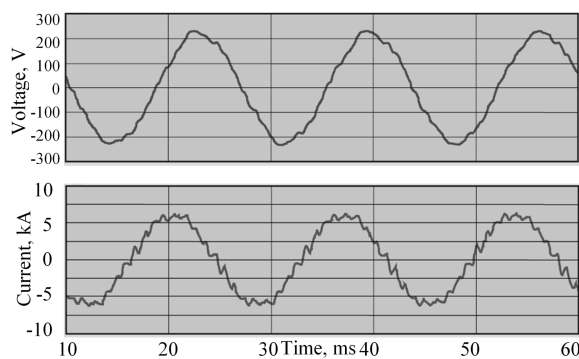


Fig. 1. Steady-state voltage (top) and current (bottom) waveforms measured at the input terminals of PWM-inverter

At the same time harmonics at the output of PWM-inverters affect the IM's durability by overheating the windings and deteriorating the isolation. The general idea behind the VFD operation implies using the pulse-width modulated (PWM) voltage waveform fed to IM. This waveform presents a sequence of multiple pulses with high rise rate du/dt and, consequently, is not sinusoidal (see Fig. 2). Together with high frequency (HF) switching this benefits the overall inverter efficiency. Nevertheless, high rise rate du/dt can lead to the following parasitic phenomena in feeders and IMs affecting durability and reliability of VFD [10]:

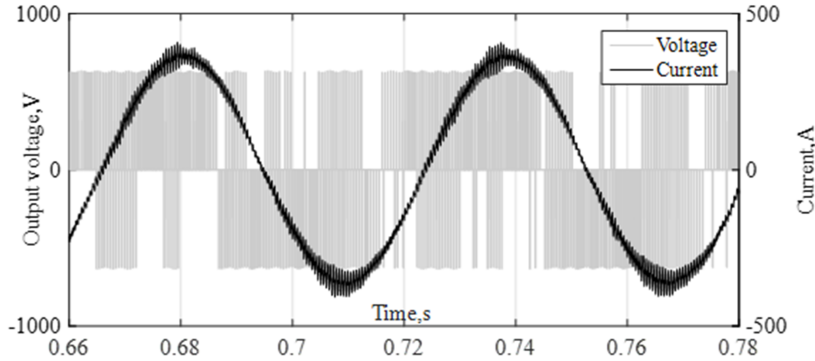


Fig. 2. Output voltage (grey line) and current (dark line) waveforms of PWM-inverter feeding induction motor

2.2. Harmonic assessment techniques

General approach for harmonic estimation at particular frequency implies grouping the intermediate spectral components (see Fig. 3) in accordance with the following equation [11]

$$Y_{g,h}^2 = \frac{1}{2}Y_{C,(Nh)-\frac{N}{2}}^2 + \sum_{k=(-\frac{N}{2})+1}^{\frac{N}{2}-1} Y_{C,(Nh)+k}^2 + \frac{1}{2}Y_{C,(Nh)+\frac{N}{2}}^2, \quad (1)$$

where $Y_{g,h}$ is the resulting RMS value of harmonic group and $Y_{C,(Nh)+\frac{N}{2}}$ (or $Y_{C,(Nh)-\frac{N}{2}}$) represents the RMS value of a spectral component, corresponding to a certain position of Discrete Fourier Transform (DFT).

The outcome of (1) presents the values for harmonic groups $Y_{g,h}$ of order h that correspond to the central components of the frequency ranges highlighted with black color in Fig. 3.

Currently only steady-state harmonic emission levels are limited by corresponding standards [2–4], while time-varying harmonics and interharmonics are left out of the scope of regulatory documents. The Fourier transform requires the repeatability of the measured signal inherent for the steady-state operation and thus can produce incorrect measurement results during transients. This impedes the utilization of standard Fast Fourier transform (FFT) in various cases of energizing equipment or

varying operation modes featuring high harmonic levels.

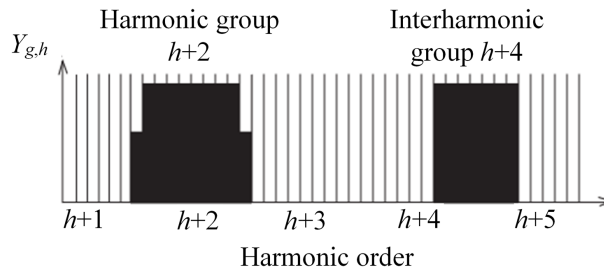


Fig. 3. Derivation of harmonic and interharmonic groups

Figure 4 exemplarily presents the distorted voltage and current waveforms of a soft-starter feeding IM at the starting period. Significant amounts of non-stationary harmonic and interharmonic distortion can be observed for both voltage and current waveforms. In this case, alternative methods of harmonic estimation should be adopted like short-time Fourier transform (STFT) or wavelet packet transform (WPT).

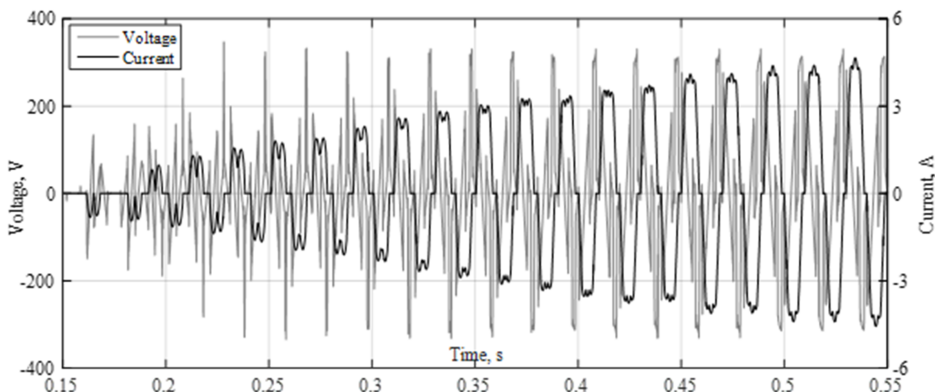


Fig. 4. Voltage (grey line) and current (dark line) waveforms at the output terminals of a soft starter supplying induction motor at the starting period

3. Assessment of non-stationary harmonic distortion

The original limitation of standard DFT is its validity for periodic steady-state infinite signals. Meanwhile, the majority of waveforms measured in real grid conditions feature non-periodic time-varying nature. If decomposed with DFT these waveforms produce spectra with multiple components adjacent to the main harmonics that can be referred as “spectral leakage” effects. In order to improve the accuracy of harmonic decomposition of dynamic signals various filtering techniques operating simultaneously in time and frequency domains can be adopted.

3.1. Short-time Fourier transform

Discrete Short-time Fourier transform (STFT) for a given signal $x(n)$ (produces a complex-valued component in a frequency band k at time instant n [12]

$$X_n(e^{j\omega_k}) = \sum_m x(m)w(n-m)e^{-j\omega_k m}, \quad k = 0, 1, \dots, N-1, \quad m = 1, 2, \dots, L, \quad (2)$$

where $\omega_k = 2\pi k/N$ is the frequency in radians, N is the number of the frequency bands, $w(m)$ is the selected symmetric window of size L , utilized to produce symmetry of the signal at the borders of considered interval. The sampling frequency f_S of the signal and the size of the window L define the center frequency f_k and the size of the bandwidth B , e.g., for Hamming window

$$f_k = f_S/N, \quad 2B = 4f_S/L. \quad (3)$$

Thus, the time-dependent frequency components of the studied signal are obtained by sliding the data window across the signal length, convolving it with original waveform and eventually decomposing the results with the DFT. The non-zero length of the data window limits the applicability of STFT method for tracing non-periodic short-time phenomena like high frequency harmonic bursts or voltage surges [12]. Nevertheless, in case of continuously varying harmonic levels STFT provides accurate and effective frequency decomposition.

3.2. Wavelet packet transform

Wavelet Packet Transform (WPT) defines the frequency components $C_{j,m}^k$ as an inner product of a given signal $x(t)$ and a scaled shifted wavelet packet function $W_m(t)$ [13]

$$C_{j,m}^k(x) = \left\langle x(t), 2^{-j/2}W_m(2^{-j}t - k) \right\rangle,$$

$$m = 0, 1 \cdot 2^j - 1, \quad k = 0, 1 \cdot 2M, \quad j = Z, \quad t = 0, 1 \cdot 2^N, \quad (4)$$

where j is the decomposition level, k denotes the shift of a wavelet function, m stands for the frequency band, and t represents the time step. The wavelet packets used to derive approximation and detail coefficients of the signal are as follows:

$$W_{2m}(t) = \sqrt{2} \sum_{k=0}^{2N-1} h(k)W_m(2t - k), \quad W_{2m+1}(t) = \sqrt{2} \sum_{k=0}^{2N-1} g(k)W_m(2t - k), \quad (5)$$

where $h(k)$ and $g(k)$ stand for the low- and high-pass filters. As a result, a uniform frequency decomposition of a given signal is built consisting of its band-pass filtered copies each corresponding to particular frequency bands. Featuring the properties of a filter bank WPT may suffer from frequency aliasing effects between adjacent frequency bands originating from non-ideal filter frequency response [13]. At the same time the capability to account for both short-term spikes and prolonged dis-

turbances, makes WPT a suitable tool for multiresolution analysis.

3.3. Kalman filtering technique

Kalman filter (KF) based procedure for harmonic spectra assessment implies iterative estimation of expected signal parameters $x(t)$ based on available measurements of $z(t)$ and initial guesses [12]. The following set of equations is built:

$$\begin{aligned}\hat{x}(t|t) &= \hat{x}(t|t-1) + G(t) [z(t) - h(\hat{x}(t|t-1))], \\ \hat{x}(t+1|t) &= F\hat{x}(t|t), \\ G(t) &= P(t)H^T \cdot (H(t)P(t)H^T(t) + R)^{-1}, \\ P(t+1) &= F [P(t) - G(t)H(t)P(t)] F^T + Q,\end{aligned}\tag{6}$$

where $\hat{x}(t|t)$, $\hat{x}(t|t-1)$ and $\hat{x}(t+1|t)$ represent the estimation of the state-space vector $x(t)$ at the time instants t , $t-1$ and $t+1$, respectively, F is the state-transition matrix, $z(t)$ and $h(t)$ stand for the vectors of measured and expected parameters, respectively, G represents the Kalman gain matrix, P is the error covariance matrix, Q and R denote the measurement and process covariance matrices, respectively, and H stands for the Jacobian of $h(t)$ derived as

$$H(t) = \frac{\partial h(\hat{x}(t|t-1))}{\partial \hat{x}(t|t-1)}.\tag{7}$$

The expected state-space vector corresponding to converged process contains estimated parameters of harmonics of the given signal. The inability to capture signals with varying or undefined frequencies hinders the use of KF method for analysis of interharmonics or PQ events in non-stiff grids. Furthermore, as the process approaches steady-state KF loses its ability to track abrupt signal variations [12]. Nevertheless, KF may be quite effective for analysis of noisy measurements.

3.4. Harmonic assessment of soft-starter output voltage supplied to induction motor

Aforementioned methods of harmonic estimation were applied to non-stationary supply voltage waveform of induction motor soft-starter (Fig. 5, top part). The transient voltage features varying harmonic content with high distortion at the early stage and pure sinusoidal waveform after the start-up is over and soft starter is bypassed. In this case harmonic decomposition was produced by means of STFT, WPT and KF for the low-order harmonics (1st, 5th, 7th and 9th) resulting in time plots of harmonic magnitudes (Fig. 5, middle part) and phase angles (Fig. 5, bottom part). Variations of harmonic magnitudes are equally well captured by three considered methods. At the same time for harmonic phase angle plots there is a certain deviation of results acquired by WPT compared with those delivered from

STFT and KF. This probably results from the filter delay introduced by wavelet functions [13].

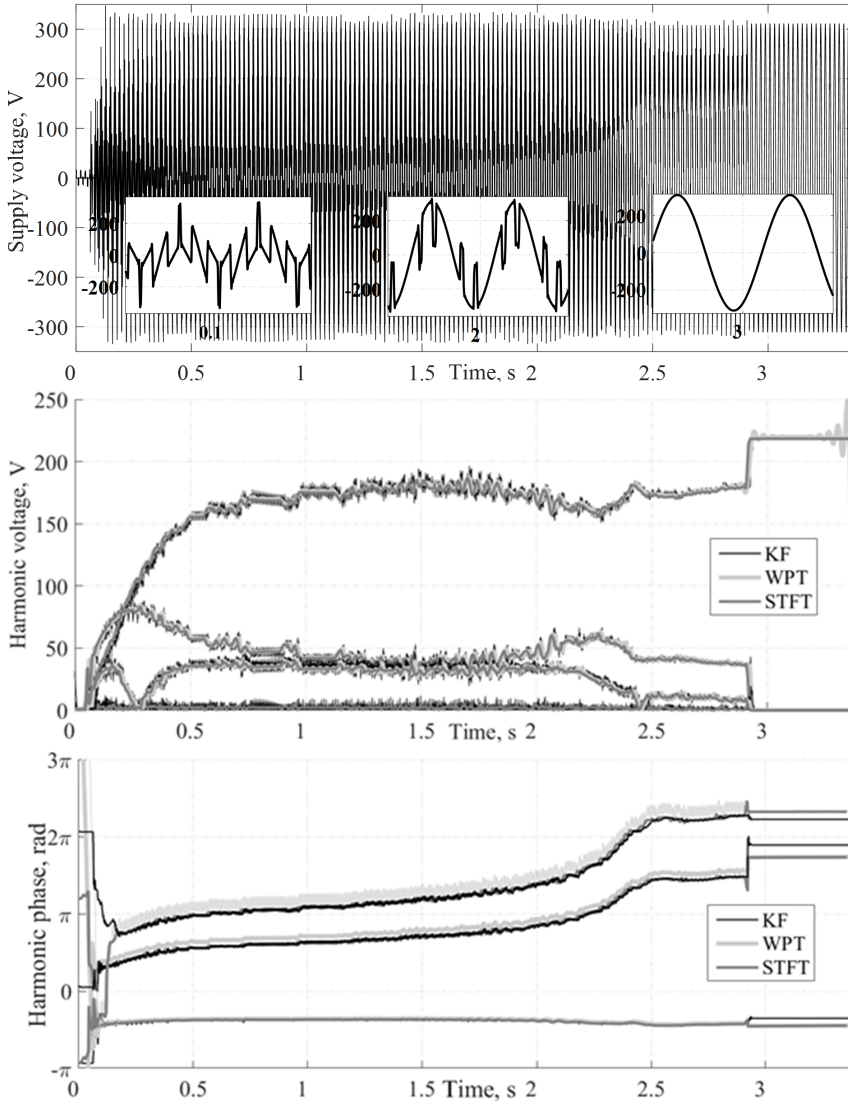


Fig. 5. Transient output voltage waveform of induction motor soft-starter (top part) and corresponding time plots of harmonic magnitudes (middle part) and phase angles (bottom part)

4. Conclusion

Vast penetration of variable frequency drives and soft-starters for induction motors brings about new challenges in harmonic control and limitation. In order to suppress high levels of non-stationary harmonic distortion inherent for this equipment new measuring and regulating approaches need to be introduced.

Conducted study of various standards prescribing the measuring, processing and limiting harmonic data acquired from induction motors operation has revealed some underdevelopment issues. These include e.g. methods for standardizing or acquiring the levels of inter- and supraharmonics. Consequently, time-varying harmonic distortion of induction motor soft-starter was exemplarily assessed by most common signal processing techniques like Short-time Fourier Transform, Wavelet Packet Transform and Kalman Filtering. Eventually, applicability limits of each method for estimating harmonic performance of variable frequency drives were outlined.

References

- [1] IEC TR 61000-2-1: *Electromagnetic compatibility (EMC) - Part 2: Environment - Section 1: Description of the environment - Electromagnetic environment for low-frequency conducted disturbances and signalling in public power supply systems* (1990).
- [2] CISPR 14-2: *Electromagnetic compatibility - Requirements for household appliances, electric tools and similar apparatus - Part 2: Immunity - Product family standard* (2015).
- [3] IEC 61000-3-2: *Electromagnetic compatibility (EMC) - Part 3-2: Limits - Limits for harmonic current emissions (equipment input current ≤ 16 A per phase)* (2013).
- [4] IEC TS 61000-3-4: *Electromagnetic compatibility (EMC) - Part 3-4: Limits - Limitation of emission of harmonic currents in low-voltage power supply systems for equipment with rated current greater than 16 A* (1998).
- [5] IEC 61000-2-12: *Electromagnetic compatibility (EMC) - Part 2-12: Environment - Compatibility levels for low-frequency conducted disturbances and signalling in public medium-voltage power supply systems* (2003).
- [6] J. LLAQUET, D. GONZALEZ, E. ALDABAS, L. ROMERAL: *Improvements in high frequency modelling of induction motors for diagnostics and EMI prediction*. IEEE Annual Conference of the Industrial Electronics Society (IECON 02), 5–8 November 2002, Sevilla, Spain, Publisher: IEEE 1 (2002), 68–71.
- [7] M. NAIM, B. SINGH, S. P. SINGH, J. SINGH: *Improvement of power factor and reduction of harmonics in three-phase induction motor by PWM techniques: A literature survey*. International Conference on Sustainable Energy and Intelligent Systems (SEISCON 2011), 20–22 July 2011, Chennai, India, Publisher: IET (2011), 529–538.
- [8] S. A. TSYRUK, E. A. KIREYEVA: *Modernization of management by pump units with use of the frequency converter and soft actuators*. Industrial Power Engineering 1 (2008), No. 1, 6–10.
- [9] O. IONTSEVA, T. ANCHAROVA: *Expediency of disaggregation of workshop transformer substations*. International Conference on Industrial Engineering, Applications and Manufacturing (ICIEAM 2016), 19–20 May 2016, Chelyabinsk, Russia, Publisher: IEEE (2016), 1–5.
- [10] E. F. FUCHS, MOHAMMAD A. S. MASOUM: *Power quality in power systems and electrical machines*. Academic Press, New-York, USA (2008).
- [11] IEC 61000-4-7:2002+AMD1:2008: *Electromagnetic compatibility (EMC) - Part 4-7: Testing and measurement techniques - General guide on harmonics and interhar-*

monics measurements and instrumentation, for power supply systems and equipment connected thereto (2009).

- [12] M. BOLLEN, I. GU: *Signal processing of power quality disturbances*. Publisher: Wiley-IEEE Press Series on Power Engineering, New-York, USA (2006).
- [13] J. BARROS, R. I. DIEGO: *Application of the wavelet-packet transform to the estimation of harmonic groups in current and voltage waveforms*. IEEE Transactions on Power Delivery *21* (2006), No. 1, 533–535.

Received October 12, 2017

Development of photometric system transformation

OLGA E. ZHELEZNIKOVA¹, SERGEY V. PRYTKOV¹,
SVETLANA A. MIKAEVA²

Abstract. The article is devoted to the determination of transition method between the photometric systems $A\alpha$, $B\beta$, $C\gamma$, based on their combination by the means of rotations in the rectangular coordinate system and the subsequent interpolation of luminous intensity values in the given units. This allows us to determine all values of meridional angles in the entire range of values correctly: $[-\pi, \pi]$ for A, B, and $[0, 2\pi]$ for C. It is shown that in order to solve the problem of a regular angle grid obtaining, one can use the interpolation of scattered data on the basis of the Delaunay triangulation.

Key words. Lighting device, photometry systems, light intensity curve, goniophotometry, photometric body, triangulation grid, the interpolation of scattered data..

1. Introduction

The spatial-angular distribution of the light intensity is determined during goniophotometric measurements and can be specified in one of the three photometric systems $A\alpha$, $B\beta$, $C\gamma$ (type A, type B, type C) [1–4]. The choice of a particular system for a particular type of light source (LS) or illuminating devices (ID) is not regulated strictly by standards, although there are some recommendations. For example, spotlights are more suitable for photo-metering in the $B\beta$ system [1–3], car headlights - in $A\alpha$ system [3], and office and street lamps - in $C\gamma$ system. If the kinematic scheme of a goniophotometer involves the rotation of a LS, and a discharge lamp is measured, then the system must be chosen in which its operation position does not change. Often, the choice can be dictated just by the convenience of measuring. There can be situations in lighting engineering practice, when photo metering is carried out in one system, and the results must be presented in another

¹Federal State Budgetary Educational Institution of Higher Education "National Research Moravia State University named after N. P. Ogarev"

²Federal State Budgetary Educational Institution of Higher Education "Moscow Technological University

system. For example, it is necessary to compare the results of two goniophotometers measurements whose kinematic schemes implement different systems of photometry. References [1, 3] contain the formulas for the transition between photometry systems. However, as will be shown below, this issue has not been studied fully.

2. Method

Photometric systems are spherical coordinate systems that are oriented in a certain way relative to photometric, longitudinal and transverse axes of a LD [1]. The combination of photo-metering systems can be carried out either by the use of the basic concepts and rules of spherical geometry [5], or via matrix transformations in the Cartesian coordinate system. Both methods lead to the same results, but in this paper we prefer the latter one because of its more economical, easy-to-remember form of record. As is well known, the transition from spherical coordinates to rectangular ones is carried out according to the following formulas:

$$\begin{aligned}x &= r \sin \theta \cos \varphi, \\x &= r \sin \theta \sin \varphi, \\z &= r \cos \theta.\end{aligned}\tag{1}$$

Now, let us explain the way of transition to rectangular coordinates associated with the photometric systems $C\gamma$, $B\beta$, $A\alpha$. The coordinate axes in all three systems are the transverse, longitudinal and photometric axes of an LD. The positive directions of the coordinate axes in the systems $C\gamma$, $B\beta$, $A\alpha$ determine the triples of the unit vectors $(\mathbf{i}_C, \mathbf{j}_C, \mathbf{k}_C)$, $(\mathbf{i}_B, \mathbf{j}_B, \mathbf{k}_B)$ and $(\mathbf{i}_A, \mathbf{j}_A, \mathbf{k}_A)$, respectively (see Figs. 1 and 2).

Figures 1 and 2 show that the polar θ and azimuth φ angles are related to the meridian and equatorial angles of the systems $C\gamma$, $B\beta$, $A\alpha$ as follows: $\theta_C = 180^\circ - \gamma$, $\varphi_C = C$, $\theta_B = 90^\circ - \beta$, $\varphi_B = B$, $\theta_A = 90^\circ + \alpha$, $\varphi_A = A$. Substituting these expressions in (1), we obtain the following formulas for the transformation of the system $C\gamma$, $B\beta$, $A\alpha$ coordinates in the rectangular coordinates

$$\begin{aligned}x_C &= \sin \gamma \cos C, \quad x_B = \cos \beta \cos B, \quad x_A = \cos \alpha \cos A, \\y_C &= \sin \gamma \sin C, \quad y_B = \cos \beta \sin B, \quad y_A = \cos \alpha \sin A, \\z_C &= -\cos \gamma, \quad z_B = \sin \beta, \quad z_A = -\sin \alpha.\end{aligned}\tag{2}$$

Now it is necessary to rotate the coordinate axes or the base of the systems. Turning again to Figs. 2–4 we see that during the transition $C\gamma \rightarrow B\beta$, the rotation is 270° counterclockwise relative to the \mathbf{j}_C axis, and 270° counterclockwise for $B\beta$

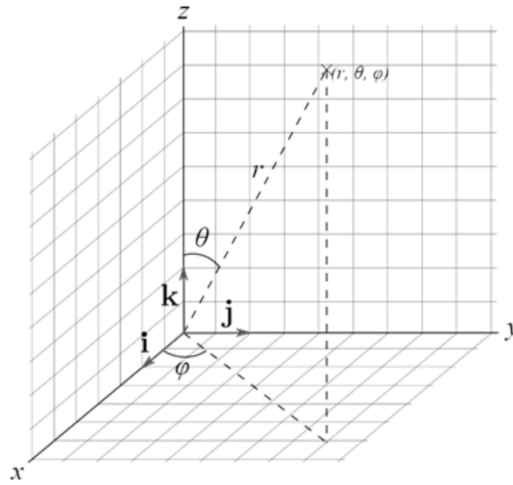


Fig. 1. Spherical coordinate system

→ $A\alpha$ -relative to the i_B axis. The matrices of the transformation data are given as

$$R_{cb} = \begin{pmatrix} \cos 270^\circ & 0 & \sin 270^\circ \\ 0 & 1 & 0 \\ -\sin 270^\circ & 0 & \cos 270^\circ \end{pmatrix} = \begin{pmatrix} 0 & 0 & -1 \\ 0 & 1 & 0 \\ 1 & 0 & 0 \end{pmatrix}, \quad (3)$$

$$R_{ba} = \begin{pmatrix} 1 & 0 & 0 \\ 0 & \cos 270^\circ & -\sin 270^\circ \\ 0 & \sin 270^\circ & \cos 270^\circ \end{pmatrix} = \begin{pmatrix} 1 & 0 & 0 \\ 0 & 0 & 1 \\ 0 & -1 & 0 \end{pmatrix}. \quad (4)$$

As will be shown later, these two matrices are sufficient to describe fully the relationship of photometry systems. Now, let us give the mathematical notation for the transformations (4)

$$c = \begin{pmatrix} x_C \\ y_C \\ z_C \end{pmatrix}, \quad b = \begin{pmatrix} x_B \\ y_B \\ z_B \end{pmatrix}, \quad a = \begin{pmatrix} x_A \\ y_A \\ z_A \end{pmatrix}.$$

The expressions (5)–(10) determine the relationship between the photo-metering systems uniquely. Solving them in an explicit form, we find the following relations:

$$C\gamma \rightarrow B\beta : B = \arctan(\sin C \tan \gamma), \quad \beta = \arcsin(\cos C \sin \gamma), \quad (5)$$

$$B\beta \rightarrow A\alpha : A = \arctan(\tan \beta / \cos \beta), \quad \alpha = \arcsin(\sin B \cos \beta), \quad (6)$$

$$C\gamma \rightarrow A\alpha : A = \arctan(\cos C \tan \gamma), \quad \alpha = \arcsin(\sin C \sin \gamma), \quad (7)$$

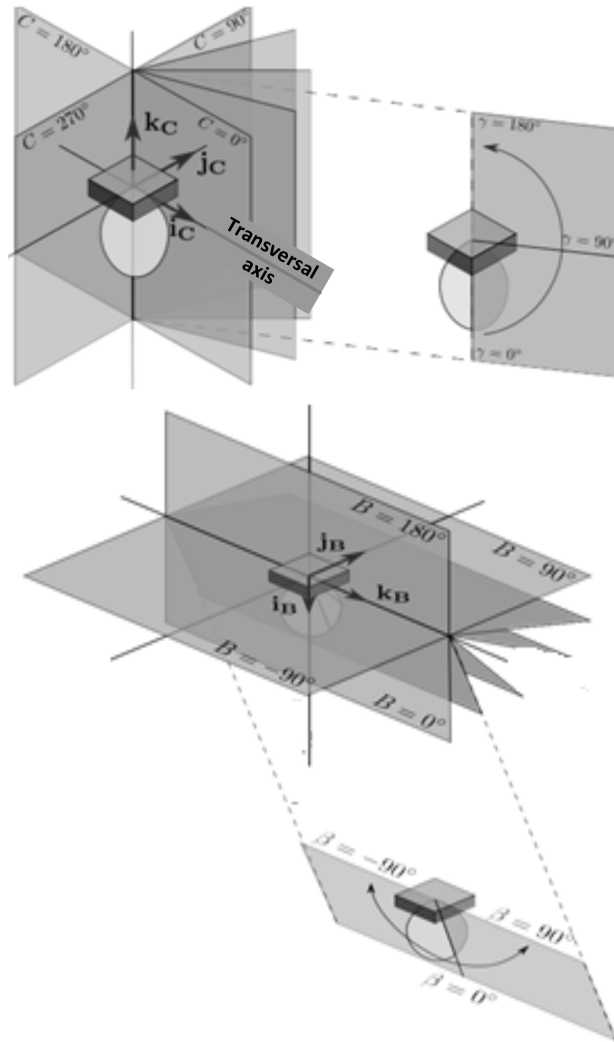


Fig. 2. Photometric system

$$B\beta \rightarrow C\gamma : C = \arctan(\sin \beta / \tan \beta), \quad \gamma = \arccos(\cos B \cos \beta), \quad (8)$$

$$A\alpha \rightarrow B\beta : B = \arctan(\tan \alpha / \cos A), \quad \beta = \arcsin(\sin A \cos \alpha), \quad (9)$$

$$A\alpha \rightarrow C\gamma : C = \arctan(\tan \alpha / \sin A), \quad \gamma = \arccos(\cos A \cos \alpha). \quad (10)$$

The same relations are given in [1]. Analyzing them and considering Figs. 1 and 2, we conclude that in order to find the equatorial angles A , B , and C , the use of only

the main branch of the arc tangent is not enough, since $-\pi \leq A \leq \pi$, $-\pi \leq B \leq \pi$, and $0 \leq C \leq 2\pi$, and at the same time $-\pi/2 < \arctan x < \pi/2$. This leads to the fact that after the conversion, half the information is lost. For a correct determination of all values of the meridional angle, it should be looked for an argument of a complex number. Taking this into account, let us rewrite the expressions (5)–(10) in the following form:

$$C\gamma \rightarrow B\beta : B = \varphi(\sin C, \cot \gamma), \quad \beta = \arcsin(\cos C \sin \gamma), \quad (11)$$

$$B\beta \rightarrow A\alpha : A = \varphi(\tan \beta, \cos \beta), \quad \alpha = \arcsin(\sin B \cos \beta), \quad (12)$$

$$C\gamma \rightarrow A\alpha : A = \varphi(\cos C, \cot \gamma), \quad \alpha = \arcsin(\sin C \sin \gamma), \quad (13)$$

$$B\beta \rightarrow C\gamma : C = \varphi * (\sin B, \tan \beta), \quad \gamma = \arccos(\cos B \cos \beta), \quad (14)$$

$$A\alpha \rightarrow B\beta : B = \varphi(\tan \alpha, / \cos A), \quad \beta = \arcsin(\sin A \cos \alpha), \quad (15)$$

$$A\alpha \rightarrow C\gamma : C = \varphi * (\tan \alpha / \sin A), \quad \gamma = \arccos(\cos A \cos \alpha). \quad (16)$$

The result of the transformation by these formulas is shown in Fig. 3.

In general, the light intensity I is the function of two variables, the values of which are known only at the points (C_i, γ_j) , but it is required to find out its value at the points from the other set (C^*_k, γ^*_l) . To do this, we must perform the Delaunay triangulation of the domain $[0, 180^\circ] \times [0, 360^\circ]$. After this, the values of $I(C^*_k, \gamma^*_l)$ can be obtained by the interpolation of $I(C_i, \gamma_j)$ values, at the vertices of the triangles. The problem is that the triangulation grid constructed from the available (C_i, γ_j) covers the domain of the function I definition not completely: the edges of the domain do not fall into any triangle (Fig. 6). This leads to the impossibility of interpolation at some points of the set (C^*_k, γ^*_l) ; the photometric body itself will have a "cutout". This difficulty can be overcome by using the parity and the periodicity of LDC, which follow from the definition of the spherical coordinate:

$$I(-C, \gamma) = I(C, \gamma), \quad I(360^\circ - C, \gamma) = I(C, \gamma),$$

$$I(-C, \gamma - 360^\circ) = I(C, \gamma), \quad I(C, \gamma + 360^\circ) = I(C, \gamma),$$

These relations make it possible to determine (C, γ) at the points lying beyond the lower, the upper, the left and the right boundaries of its definition domain, respectively. Expanding these boundaries, it is possible to ensure that the original rectangle $[0^\circ, 180^\circ] \times [0^\circ, 360^\circ]$, together with all the points (C^*_k, γ^*_l) , will be covered by Delaunay triangulation grid completely, built for a new expanded domain of definition.

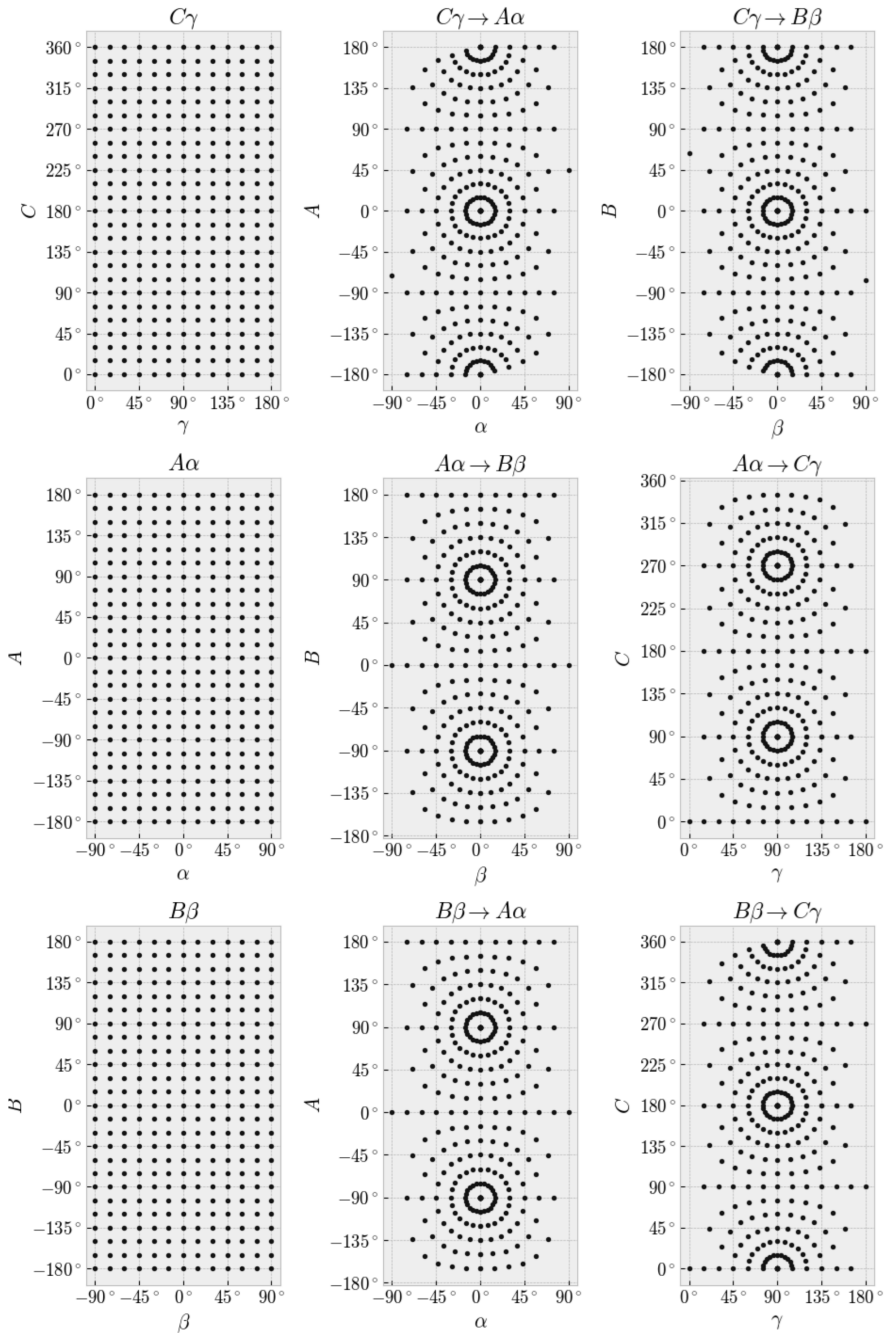


Fig. 3. Photometric system nodes before and after conversion by formulas 11–16

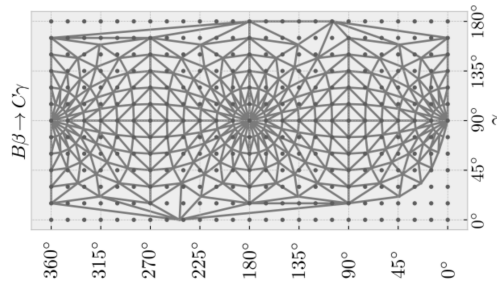


Fig. 4. Interpolation by scattered data

3. Conclusion

The paper showed that after the transformations (11–16), the grid of angles becomes irregular, which in its turn leads to the inability to generate photometric data files in widely distributed formats ldt and ies. It is shown that in order to solve the problem of a regular grid of angles, one can use the interpolation of scattered data on the basis of Delaunay triangulation. The solution for photometric system conversion proposed by the authors is more universal. Secondly, [1, 3] do not indicate that after the transformation $B\beta \rightarrow C\gamma$ the grid of angles becomes irregular one, with all the ensuing consequences. And, thirdly, in order to transform $A\alpha \rightarrow C\gamma$ the formulas are proposed in [3] that do not agree with either [1] or with the solution proposed in this paper.

References

- [1] IESNA LM-75-01: *Goniophotometer types and photometric coordinates (Reaffirmed 2012)*. New York: Illuminating Engineering Society of North America (2012), p. 12.
- [2] J. P. WEISSHAAR: *Next generation goniophotometry*. *Light and Engineering* 23 (2015), No. 4, 75–80.
- [3] D. V. ALEKSEEVSKY, E. B. VINBERG, A. S. SOLODOVNIKOV: *The geometry of constant curvature spaces*. Results of science and technology. Modern problems of mathematics (fundamental trends), VINITI, Moscow 29 (1988), 1–146.
- [4] A. W. STOCKMAR: *EULUMDAT/2 - Extended version of a well established luminaire data format*. CIBSE National Lighting Conference, 5–8 April 1998, Lancaster University, UK, Proceedings 353–362.
- [5] A. V. SKVORTSOV: *Delaunay triangulation and its application*. Tomsk: Publishing house of Tomsk University (2002), p. 128.
- [6] IESNA LM-63-1995: *IESNA LM-63-1995*. New York: Illuminating Engineering Society of North America (1995).
- [7] EN 13032-2:2004: *Light and Lighting. Measurement and Presentation of Photometric Data of Lamp and Luminaries (2004)*.

Received October 12, 2017

